N°d'ordre NNT : 2018LYSEI060

THESE de DOCTORAT DE L'UNIVERSITE DE LYON
opérée au sein de
INSA de LYON

Ecole Doctorale N° 162
**Ecole doctorale des Sciences pour l'Ingénieur de Lyon :
Mécanique, Energétique, Génie Civil, Acoustique (MEGA)**

Spécialité/ discipline de doctorat :
Génie Mécanique

Soutenue publiquement le 11/07/2018, par :
Stéphane Tromp

Lubrication with a refrigerant: an industrial challenge investigated through multiscale modeling based on fluid/surface chemistry

Devant le jury composé de :

Cobian, Manuel	Maître de Conférences / Ecole Centrale Lyon	Examinateur
Dini, Daniele	Professeur / Imperial College London	Rapporteur
Fillot, Nicolas	Maître de Conférences - HDR / INSA-Lyon	Directeur
Joly, Laurent	Professeur / Université Claude Bernard Lyon 1	Co-directeur
Leonard, Céline	Professeur / Université Paris-Est Marne-La-Vallée	Examinatrice
Moseler, Michael	Professeur / University of Freiburg	Rapporteur

Département FEDORA – INSA Lyon - Ecoles Doctorales – Quinquennal 2016-2020

SIGLE	ECOLE DOCTORALE	NOM ET COORDONNEES DU RESPONSABLE
CHIMIE	**CHIMIE DE LYON** http://www.edchimie-lyon.fr Sec. : Renée EL MELHEM Bât. Blaise PASCAL, 3e étage secretariat@edchimie-lyon.fr INSA : R. GOURDON	M. Stéphane DANIELE Institut de recherches sur la catalyse et l'environnement de Lyon IRCELYON-UMR 5256 Équipe CDFA 2 Avenue Albert EINSTEIN 69 626 Villeurbanne CEDEX directeur@edchimie-lyon.fr
E.E.A.	**ÉLECTRONIQUE, ÉLECTROTECHNIQUE, AUTOMATIQUE** http://edeea.ec-lyon.fr Sec. : M.C. HAVGOUDOUKIAN ecole-doctorale.eea@ec-lyon.fr	M. Gérard SCORLETTI École Centrale de Lyon 36 Avenue Guy DE COLLONGUE 69 134 Écully Tél : 04.72.18.60.97 Fax 04.78.43.37.17 gerard.scorletti@ec-lyon.fr
E2M2	**ÉVOLUTION, ÉCOSYSTÈME, MICROBIOLOGIE, MODÉLISATION** http://e2m2.universite-lyon.fr Sec. : Sylvie ROBERJOT Bât. Atrium, UCB Lyon 1 Tél : 04.72.44.83.62 INSA : H. CHARLES secretariat.e2m2@univ-lyon1.fr	M. Philippe NORMAND UMR 5557 Lab. d'Ecologie Microbienne Université Claude Bernard Lyon 1 Bâtiment Mendel 43, boulevard du 11 Novembre 1918 69 622 Villeurbanne CEDEX philippe.normand@univ-lyon1.fr
EDISS	**INTERDISCIPLINAIRE SCIENCES-SANTÉ** http://www.ediss-lyon.fr Sec. : Sylvie ROBERJOT Bât. Atrium, UCB Lyon 1 Tél : 04.72.44.83.62 INSA : M. LAGARDE secretariat.ediss@univ-lyon1.fr	Mme Emmanuelle CANET-SOULAS INSERM U1060, CarMeN lab, Univ. Lyon 1 Bâtiment IMBL 11 Avenue Jean CAPELLE INSA de Lyon 69 621 Villeurbanne Tél : 04.72.68.49.09 Fax : 04.72.68.49.16 emmanuelle.canet@univ-lyon1.fr
INFOMATHS	**INFORMATIQUE ET MATHÉMATIQUES** http://edinfomaths.universite-lyon.fr Sec. : Renée EL MELHEM Bât. Blaise PASCAL, 3e étage Tél : 04.72.43.80.46 Fax : 04.72.43.16.87 infomaths@univ-lyon1.fr	M. Luca ZAMBONI Bât. Braconnier 43 Boulevard du 11 novembre 1918 69 622 Villeurbanne CEDEX Tél : 04.26.23.45.52 zamboni@maths.univ-lyon1.fr
Matériaux	**MATÉRIAUX DE LYON** http://ed34.universite-lyon.fr Sec. : Marion COMBE Tél : 04.72.43.71.70 Fax : 04.72.43.87.12 Bât. Direction ed.materiaux@insa-lyon.fr	M. Jean-Yves BUFFIÈRE INSA de Lyon MATEIS - Bât. Saint-Exupéry 7 Avenue Jean CAPELLE 69 621 Villeurbanne CEDEX Tél : 04.72.43.71.70 Fax : 04.72.43.85.28 jean-yves.buffiere@insa-lyon.fr
MEGA	**MÉCANIQUE, ÉNERGÉTIQUE, GÉNIE CIVIL, ACOUSTIQUE** http://edmega.universite-lyon.fr Sec. : Marion COMBE Tél : 04.72.43.71.70 Fax : 04.72.43.87.12 Bât. Direction mega@insa-lyon.fr	M. Jocelyn BONJOUR INSA de Lyon Laboratoire CETHIL Bâtiment Sadi-Carnot 9, rue de la Physique 69 621 Villeurbanne CEDEX jocelyn.bonjour@insa-lyon.fr
ScSo	**ScSo*** http://ed483.univ-lyon2.fr Sec. : Viviane POLSINELLI Brigitte DUBOIS INSA : J.Y. TOUSSAINT Tél : 04.78.69.72.76 viviane.polsinelli@univ-lyon2.fr	M. Christian MONTES Université Lyon 2 86 Rue Pasteur 69 365 Lyon CEDEX 07 christian.montes@univ-lyon2.fr

*ScSo : Histoire, Géographie, Aménagement, Urbanisme, Archéologie, Science politique, Sociologie, Anthropologie

Remerciements

Je tiens à remercier mes directeurs de thèse, Nicolas Fillot et Laurent Joly qui m'ont offert l'opportunité de réaliser cette thèse au LaMCoS et à l'ILM. Merci pour votre disponibilité, vos conseils, et votre gentillesse. De plus je tiens à remercier chaleureusement Manuel Cobian qui s'est greffé au projet dès le début et qui a été d'une très grande aide dans ce projet, en particulier pour toute la partie ab-initio.

Mes remerciements vont ensuite à mes deux rapporteurs de thèse, Daniele Dini et Michael Moseler pour avoir pris le temps de relire et juger ce travail et à Céline Leonard pour l'avoir examiné.

Merci à Nathalie Bouscharain et Guillermo Morales-Espejel qui m'ont apporté respectivement leurs connaissances sur la chimie des réfrigérants et sur les applications industrielles.

Cette thèse ayant été réalisée grâce au financement du labex iMUST, je tiens à remercier Amandine Ducreux pour sa grande réactivité lors de mes différents congrès et missions.

Un merci particulier à Vincent Strubel sans qui cette thèse n'aurait tout simplement pas eu lieu, puisque c'est lui qui m'a présenté à Nicolas Fillot en 2014. Bien sûr grâce à toi, beaucoup d'autres choses très positives se sont produites durant ces années. Merci également à Nicolas Voeltzel qui a passé beaucoup de temps à me transmettre ce qu'il savait sur la dynamique moléculaire et à Alejandro Porras Vázquez et Rafael Pereira De Matos pour nos nombreuses discussions sur cette méthode. Merci également à Sayed Albahrani pour nos discussions très variées sur la physique et la tribologie.

Je n'oublie pas de remercier chaleureusement les autres membres de l'équipe TMI et plus généralement du LaMCoS avec qui j'ai pu interagir durant ces années. Grâce à vous, j'ai pu m'épanouir professionnellement et personnellement. Merci également à tous les membres de l'équipe du badminton de ces trois années.

Lors des nombreux congrès auxquels j'ai participé durant ma thèse, j'ai pu discuter avec des scientifiques de différents horizons et pays. Cela m'a beaucoup apporté et je veux pour cela remercier mes directeurs de thèse qui m'ont fait confiance en me laissant présenter ces travaux. J'ai également eu la chance de pouvoir enseigner en TD de

mathématiques pour des étudiants ingénieurs en 3e année. Ce fut une expérience particulièrement enrichissante. Pour cela je remercie Etienne Parizet. De plus je remercie ici aussi Nicolas Fillot qui m'a permis de co-encadrer deux étudiants de Master lors de leur stage de fin d'études. Pour leur aide logistique, je tiens à remercier Emmanuel Montero et Sophie De Oliveira.

Je ne vais pas faire une liste de tous les doctorants, postdoc, et stagiaires, avec qui j'ai passé de super moments au labo et également beaucoup en dehors, ils se reconnaîtront. Merci pour toutes ces marches, bars, sorties ski,... !

Je conclus ces remerciements en les adressant à toute ma famille qui m'a soutenu durant ma scolarité et enfin merci à Laurence de m'avoir supporté, particulièrement durant ces derniers mois.

Abstract

In large refrigeration systems, using the refrigerant as lubricant instead of oil can help to simplify the design, lighten the systems, and reduce their environmental impact. However, the very low viscosity of refrigerants leads to ultra-thin films separating the surfaces, with a thickness comparable to surface roughness. Nevertheless, experiments with the R1233zd refrigerant suggests that lubrication is still possible in that situation thanks to an adsorbed layer formed on iron oxide surfaces. Experimental in situ analysis area is very difficult because of high confinement and high pressure. That is why a multiscale numerical approach is developed here, to explore the impact of chemical reactions and physical processes at the refrigerant-surface interface on large-scale lubrication properties. Density functional theory is used to quantify the adsorption of a refrigerant molecule on an iron oxide surface at the quantum level. Binding energies ranging from -0.92 eV to -0.22 eV are measured and related to different adsorption cases. These results are then used to parametrize an interfacial force field, whose predictions of interfacial molecular structure differs from those obtained using potentials based on standard mixing rules. Large-scale molecular dynamics simulations involving this parametrized force field confirm the existence of a strongly adsorbed layer of R1233zd molecules on Fe_2O_3 surface. With atomically smooth surfaces, and a refrigerant film thickness as small as 2 nm, the adsorbed refrigerant layers resists pressures as high as 4 GPa and sliding velocities as high as 100 m/s. A minimum value of 5 refrigerant molecules per nm^2 is necessary to the formation of two adsorbed layers at 0.5 GPa. Moreover, sliding simulations with a rough surface reveal total film breakdown for around 13 GPa.

Keywords: Lubrication, Refrigerants, Fluid/Surface Physical Chemistry, Molecular Dynamics, Density Functional Theory.

Résumé

Dans les grands systèmes de réfrigération, l'utilisation de réfrigérants comme lubrifiants, à la place des huiles, simplifie la conception du système, l'allège et réduit son impact environnemental. La très faible viscosité du réfrigérant conduit à une épaisseur de film séparant les deux surfaces comparable à leur rugosité. Néanmoins, des travaux expérimentaux avec le réfrigérant R1233zd suggèrent que la lubrification est possible dans ces conditions grâce à la formation d'une couche adsorbée sur la surface d'oxyde de fer. Les analyses expérimentales in situ dans le contact sont très difficiles à cause des conditions de fort confinement et haute pression. C'est pourquoi une approche numérique multi-échelles est développée, afin d'étudier l'impact des réactions physico-chimiques à l'interface réfrigérant-surface sur les propriétés de lubrification. La théorie de la fonctionnelle de la densité est utilisée pour quantifier au niveau quantique, l'adsorption d'une molécule de réfrigérant sur une surface d'oxyde de fer. Des énergies de liaison allant de -0,92 eV à -0,22 eV sont observées et reliées à différents cas d'adsorption. Ces résultats sont exploités pour paramétrer un champ de forces interfacial, qui prédit des structures moléculaires à l'interface, différentes de celles obtenues avec des potentiels basés sur les règles de mélange classiques. Des simulations de dynamique moléculaire utilisant ce champ de forces paramétré confirment l'existence d'une couche fortement adsorbée de R1233zd sur une surface de Fe_2O_3. Avec des surfaces atomiques lisses et seulement 2 nm d'épaisseur de film de réfrigérant, les couches adsorbées résistent à des pressions allant jusqu'à 4 GPa et des vitesses de cisaillement atteignant 100 m/s. Une valeur minimale de 5 molécules de réfrigérant par nm^2 est nécessaire à la formation de deux couches adsorbées à 0,5 GPa. De plus, des simulations en cisaillement avec une surface rugueuse prédisent une rupture totale du film à environ 13 GPa.

Mots-clés: Lubrification, Réfrigérants, Physico-Chimie Fluide/Surface, Dynamique Moléculaire, Théorie de la Fonctionnelle de Densité.

Résumé étendu

0.1 Introduction générale et contexte

La lubrification consiste à introduire un lubrifiant entre deux surfaces en mouvement l'une par rapport à l'autre afin de réduire le frottement et l'usure. En réduisant la contrainte entre les éléments mobiles, elle améliore la durée de vie des composants mécaniques. Néanmoins, la lubrification nécessite souvent une conception lourde, avec par exemple l'ajout de pompes à lubrifiant, alors que la tendance actuelle est à l'allégement des systèmes mécaniques.

Dans les grands systèmes de réfrigération, la conception peut être simplifier en utilisant le fluide dit actif, ici le réfrigérant, pour lubrifier les roulements. Cependant, les réfrigérants possèdent de faibles viscosités, contraignant le film de réfrigérant séparant les deux surfaces à atteindre localement une épaisseur de quelques nanomètres, donc du même ordre de grandeur que les rugosités des surfaces. C'est pour cette raison qu'une quantité minimum de réfrigérant doit être entraînée entre les aspérités pour éviter que les surfaces ne rentrent en contact.

Avec ce régime de lubrification à très faible épaisseur, seules quelques molécules séparent localement les surfaces. Dans ce contexte, la physicochimie à l'interface entre le réfrigérant et les surfaces joue un rôle prédominant. La littérature révèle qu'une couche adsorbée de molécules de réfrigérant a été observée sur les surfaces d'acier du roulement, lors d'un test de lubrification avec réfrigérant pur.

Néanmoins, les conditions sévères de grand confinement et haute pression rendent difficiles les analyses expérimentales in situ. C'est pour cette raison qu'une approche de modélisation multi-échelles est considérée dans cette thèse pour étudier les performances tribologiques d'un système lubrifié avec un réfrigérant pur tel que le R1233zd, confiné entre deux surfaces de fer.

Tout d'abord, des simulations quantiques basées sur la théorie de la fonctionnelle de la densité (DFT, pour *density functional theory*) permettent d'analyser la physicochimie à l'interface entre le réfrigérant et la surface. Puis, des simulations de dynamique

moléculaire (DM) à plus large échelle, paramétrées à l'aide des résultats ab-initio, sont utilisées pour étudier la structure et le comportement dynamique du réfrigérant confiné sous conditions tribologiques extrêmes.

La réfrigération est le processus durant lequel la température d'un espace clos est réduite par déplacement de la chaleur vers un autre endroit. Les réfrigérants sont des fluides utilisés dans plusieurs types de systèmes tels que les chauffages, climatisations ou équipements de refroidissement.

Les réfrigérants sont classés en plusieurs familles selon les différents types d'atomes et structures moléculaires du réfrigérant. Des contraintes environnementales et de sécurité ont conduit à l'apparition d'une toute nouvelle génération de réfrigérant composée d'hydrofluoroléfines (HFO). Le HCFO-1233zd(E), plus communément nommé R1233zd, fait partie de cette nouvelle génération et est particulier car sa molécule possède un atome de chlore, faisant de lui une molécule hydrochlorofluoroléfine (HCFO).

Le R1233zd : un réfrigérant de nouvelle génération

En raison de son point d'ébullition relativement élevé (environ 19°C à pression atmosphérique), le R1233zd est considéré comme un réfrigérant alternatif pour plusieurs types de systèmes tels que les pompes à chaleur à haute température, ou les systèmes de réfrigération à basse pression. Ce projet se concentre sur l'étude de systèmes de réfrigération utilisés pour refroidir de grands bâtiments ou procédés industriels. Durant un cycle classique de réfrigération, le réfrigérant est compressé à l'aide d'un compresseur composé entres autres par des roulements. Ces roulements sont classiquement lubrifiés avec un mélange huile-réfrigérant. Cependant, le but de cette étude et d'étudier la faisabilité de lubrifier les roulements à l'aide d'un réfrigérant R1233zd pur. Ce type de système s'appelle PRL (pour "pure refrigerant lubrication").

Lubrification dans les systèmes de réfrigération

Les roulements dans les technologies PRL sont hybrides. En effet, les billes sont faites de nitrure de silicium Si_3N_4 (céramique), tandis que les bagues intérieures et extérieures sont en acier inoxydable [1, 2, 3].

De plus, ces roulements sont lubrifiés dans un régime de lubrification de film très mince où l'épaisseur de film minimale peut être de quelques nanomètres. Des essais expérimentaux portant sur le R1233zd comme lubrifiant, dans des conditions de fonctionnement variables (pression de contact hertzienne d'environ 1.2 GPa en moyenne) ont été réalisés par la société SKF [4, 5]. Ils ont observé que cette lubrification extrême n'avait pas causé de dégât aux surfaces du roulement et qu'un dépôt solide s'était crée sur les surface en acier. L'analyse XPS de ces dernières a révélé que:

- la surface était principalement constituée d'oxydes de fer(II) FeO et d'oxyde de

fer(III) Fe_2O_3,

- les éléments constituant les molécules de R1233zd comme le chlore et fluor sont détectés sur la couche adsorbée,

- l'épaisseur de cette couche peut atteindre jusqu'à 25 nm pour des tests longs.

Malheureusement, ces résultats ne donnent pas d'indication sur la structure ou l'écoulement du réfrigérant confiné.

0.2 Objectifs de la thèse

Ce projet vise à comprendre le comportement physico-chimique entre la surface et le R1233zd et ses effets sur les performances tribologiques. Les roulements hybrides combinés avec des bagues en acier inoxydable donnent les meilleures performances tribologiques des systèmes PRL. Pour cette raison, une surface d'oxyde de fer représentée par une surface d'hématite ($\alpha - Fe_2O_3$) est considérée dans toute l'étude et le R1233zd nanoconfiné entre deux surfaces d'hématite est étudié. Les expériences citées ci-dessus suggèrent que la lubrification est possible dans cette situation grâce à une couche adsorbée qui se forme sur des surfaces d'oxyde de fer. Tandis que l'analyse in-situ expérimentale à l'intérieur de la zone de contact est encore très difficile, nous utilisons des simulations numériques pour observer les réactions chimiques et les processus physiques à l'interface entre le réfrigérant et la surface.

Dans ce contexte, nous avons développé une approche numérique multi-échelles où les calculs DFT, décrivant la matière au niveau de sa structure électronique, sont associés à des simulations de DM à grande échelle, utilisant des champs de forces empiriques paramétrés en utilisant les résultats de la DFT. Tout d'abord, les résultats obtenus avec la DFT sont détaillés dans la prochaine section et les interactions entre le réfrigérant et l'hématite sont étudiées à l'échelle quantique. Les calculs DFT sont utilisés pour obtenir des énergies de liaison précises sous différentes conformations. Dans la section suivante, le modèle de dynamique moléculaire est développé. La méthodologie utilisée pour paramétrer un champ de force à l'interface surface/réfrigérant sur la base de ces résultats DFT ne sera pas détaillée dans ce résumé. Cependant, des simulations de DM à grande échelle impliquant ce champ de force paramétré confirment l'existence d'une couche fortement adsorbée de molécules de R1233zd sur la surface Fe_2O_3. La résistance de cette couche adsorbée est explorée dans des conditions extrêmes de pression et de vitesse de cisaillement en présence de surfaces lisses et rugueuses. De plus, la structure, l'écoulement et le comportement en frottement sont étudiés avant la rupture locale du film de réfrigérant. Le rôle des orientations des molécules aux interfaces est également

discuté.

0.3 Physicochimie à l'interface réfrigérant-surface dans un système lubrifié : une étude ab-initio

Les résultats de cette section ont été en partie publiés dans "Journal of Physical Chemistry C" [6].

Durant les dernières décennies, l'intérêt pour les calculs quantiques permettant de prédire la structure électronique de la matière, a augmenté. Du point de vue de la physico-chimie et même de l'intérêt industriel, les propriétés électroniques sont primordiales. Les méthodes ab-initio visent à résoudre des équations de mécanique quantique, qui sont généralement des formes simplifiées de l'équation de Schrödinger. En effet, cette dernière est très difficile à résoudre dès lors que le plusieurs électrons sont présents dans le système. L'une des méthodes les plus populaires est la théorie de la fonctionnelle de la densité (DFT), qui utilise la densité électronique pour résoudre un problème à plusieurs corps. Les calculs DFT ont été testés pour décrire divers phénomènes dans différents domaines de la science. Par exemple, elle permet de décrire des processus chimiques comme la synthèse d'ammoniac ou l'hydrogénation [7], ainsi que le comportement mécanique dû à la fragilisation des métaux, ou même d'étudier les propriétés des matériaux au cours de la formation des planètes [8]. En particulier, la DFT offre la possibilité d'étudier les phénomènes de lubrification. En effet, cette méthode a été testée pour étudier le frottement au travers des réactions chimiques à l'interface solide-liquide [9]. La DFT a également été utilisée pour paramétrer des champs de forces entre le lubrifiant et les surfaces dans les contacts lubrifiés [10, 11].

Dans cette section, le modèle utilisé dans cette étude ab-initio est détaillé. L'adsorption de la molécule R1233zd sur une surface d'oxyde de fer (hématite) est étudiée, et en particulier les énergies de liaisons sont calculées. De plus, la distribution des charges durant le procédé d'adsorption est examinée.

0.3.1 Modèle : système R1233zd-hématite et énergies de liaison

Dans cette section, nous étudions l'adsorption des molécules de réfrigérant au niveau quantique en considérant un ensemble de positions et d'orientations d'une molécule proche de la surface. Ceci vise à imiter des situations probables dans un contact lubrifié réel. Afin de représenter une surface en acier située dans un roulement, un oxyde de fer est considéré. Comme représenté sur la Figure 1, la surface d'oxyde de fer est décrite avec

l'hématite $\alpha - Fe_2O_3$, qui est la forme thermodynamiquement la plus stable des oxydes de fer sous environnement ambiant et ainsi, la plus présente sur terre. Le choix a été fait de considérer l'orientation $(01\overline{1}2)$ en raison de la présence d'atomes de fer et d'oxygène sur la couche supérieure. Par conséquent, un ensemble représentatif d'interactions entre les atomes du réfrigérant et la surface sera considéré. La molécule R1233zd est structurée autour d'une liaison double carbone-carbone. Le premier carbone sp^2 de cette double liaison est lié à un atome d'hydrogène H1 et un atome de Cl, tandis que le second carbone sp^2 est lié à un hydrogène nommé H2 et à un groupe CF$_3$. Les dimensions (x,y,z) de l'hématite relaxée sont approximativement de 10 Å x 10 Å x 10 Å.
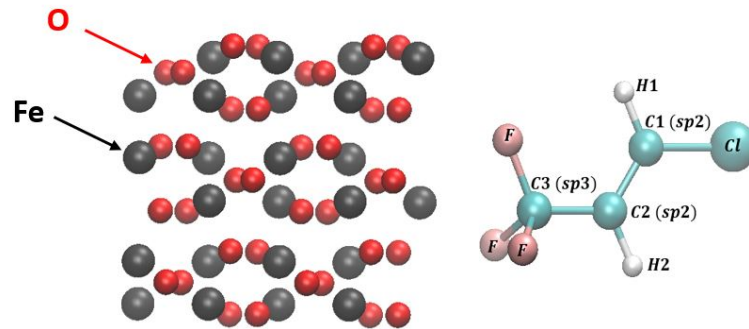
Figure 1: Surface d'hématite $\alpha - Fe_2O_3(01\overline{1}2)$ relaxée (gauche) et molécule de R1233zd (droite).

Afin d'étudier l'adsorption de molécules R1233zd sur des surfaces d'hématite ($\alpha - Fe_2O_3$), le code CP2K/QUICKSTEP [12] (version 3.0) est utilisé pour effectuer les calculs DFT. Comme les forces de van der Waals sont primordiales pour décrire les liquides et le comportement interfacial, le terme d'échange et corrélation est calculé dans l'approximation des gradients généralisée GGA avec la fonctionnelle de la densité, non locale, optB88-vdW [13]. Dabaghmanesh et al. [14] a montré que cette fonctionnelle permet de décrire précisément l'adsorption du méthane et du benzène sur la surface d'hématite. Le but est de trouver l'énergie la plus basse de tout le système composé d'une molécule de R1233zd et d'une surface Fe$_2$O$_3$ formée de 120 atomes. Comme la surface est déjà relaxée, les atomes de fer et d'oxygène restent fixes pendant l'optimisation de la géométrie et seule la molécule de réfrigérant peut se déplacer dans une boîte de 10,24 Å x 10,93 Å x 25 Å. Cette dernière dimension laisse un vide d'environ 1 nm entre le sommet de la molécule et le bas de l'image périodique de la surface solide. Avec la méthode DFT + U, où U = 5 eV, les électrons fortement corrélés 3d du fer sont correctement décrits [15, 16, 17, 18].

Énergie de liaison :

Le capacité d'adsorption du R1233zd sur le $(01\overline{1}2)$ $\alpha - Fe_2O_3$ a été étudiée et les valeurs d'énergie de liaison Eb (pour "binding energies") ont été calculées avec la formule
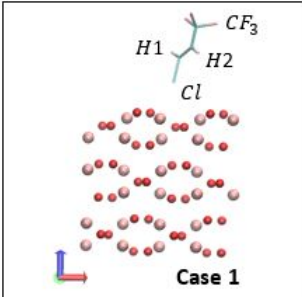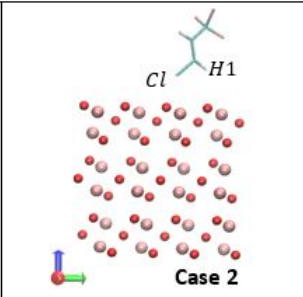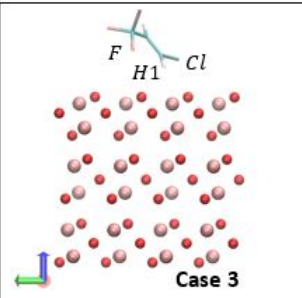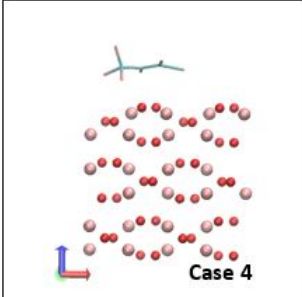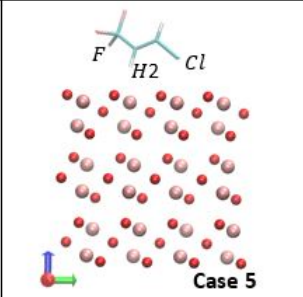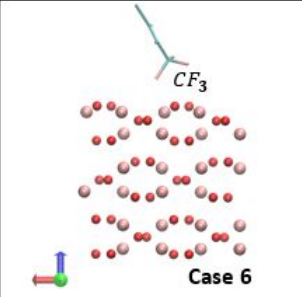
suivante:

$$Eb = E_{\{surface+1mol_{R1233zd}\}} - E_{\text{surface}} - E_{1mol_{R1233zd}} \tag{1}$$

où $E_{surface+1mol_{R1233zd}}$ est l'énergie totale du système adsorbat-substrat relaxé, E_{surface} est l'énergie de la surface isolée et $E_{1mol_{R1233zd}}$ est l'énergie de la molécule R1233zd isolée. Les deux derniers termes sont calculés en utilisant la même géométrie que celle optimisée pour le système {surface + 1mol$_{R1233zd}$}. Une valeur négative de l'énergie de liaison signifie que la géométrie obtenue est plus stable que l'état non lié.

0.3.2 Adsorption du R1233zd sur des surfaces d'oxydes de fer

Seize configurations initiales différentes ont été obtenues par translations et rotations aléatoires de la molécule de réfrigérant par rapport aux trois directions de l'espace. Comme indiqué dans le Tableau 1 ci-dessous, l'adsorption peut se produire suivant six cas différents (correspondant chacun à des positions et orientations similaires), associés à six gammes d'énergie de liaison. Tous les résultats d'adsorption sont visualisés avec le logiciel "visual molecular dynamics" (VMD) [19].

Table 1: Six cas d'adsorption différents associés à leurs valeurs d'énergie de liaison et leur numéro d'optimisation de géométrie.

Le premier résultat important est que les atomes de chlore interagissent fortement avec

les atomes de fer, comme le montre le cas 1 du Tableau 1. Lors de l'optimisation de la géométrie, il est également possible que la molécule de réfrigérant s'incline et que l'hydrogène H1 situé près du chlore stabilise la molécule adsorbée, comme indiqué dans le cas 2. Le cas 3 montre que le fluor peut également participer à l'adsorption, avec une liaison plus forte que dans le cas 2, et qui atteint ici une valeur de -0,65 eV. L'hypothèse d'une interaction possible entre les atomes de fer et de fluor a déjà été soulevée dans la littérature [20], mais pour un autre réfrigérant. Le cas 4 représente l'adsorption la plus forte. En effet, les énergies de liaison avec la molécule de réfrigérant parallèle à la surface d'hématite ont une amplitude plus grande que celles avec les orientations verticales de la molécule. Par conséquent, cela signifie que les positions horizontales des molécules de réfrigérant sont plus stables que celles verticales. En effet, la surface intéragit d'un côté avec le chlore, mais également avec les fluors. De plus, la liaison π entre les carbones sp^2 pourrait jouer un rôle. Pour le cas 5, la molécule a subi une rotation le long de l'axe de la double liaison carbone-carbone ; le chlore, le fluor et l'hydrogène H2 lié au carbone situé au milieu de la molécule, interagissent avec la surface. Dans le cas 6, seuls les atomes de fluor interagissent avec la surface. Cette dernière orientation de la molécule s'est trouvée en pratique être la plus difficile à obtenir car le processus d'optimisation de la géométrie ne convergeait pas facilement. Il est également intéressant d'observer qu'il est possible d'obtenir la même valeur d'énergie de liaison avec une molécule adsorbée soit grâce aux trois atomes de fluor, soit seulement avec l'atome de chlore. Cette dernière observation appuie certaines supposition trouvées dans la littérature avec un autre réfrigérant, le R12, à propos d'une formation de revêtement chlore-fer [21]. En effet, les atomes de chlore et de fer interagissent fortement et la molécule R1233zd peut être adsorbée avec une contribution majeure des interactions de van der Waals entre ces deux atomes et bien sûr à cause de toutes les interactions coulombiennes. De plus, Akram et al. ont rapporté la formation d'un film enrichi en fluor FeF_3 pour le HFO-1234yf [22]. Il est donc possible de lier cette observation à la géométrie optimisée du cas 6.

Après voir introduit notre modèle DFT, les résultats concernant l'adsorption de molécules de R1233zd sur la surface de l'oxyde de fer ont été présentés. Cette section représente un complément idéal pour répondre à certaines lacunes expérimentales présentes dans la littérature. Le point délicat était d'utiliser la méthode DFT + U avec une fonctionnelle vdW combinée à un système polarisé en spin. Les principaux résultats, incluant une étude supplémentaire sur la distribution des charges, non détaillée dans ce résumé, peuvent être rapportées comme suit:

- on observe une plage de valeurs d'énergie de liaison de la molécule de réfrigérant sur la surface d'oxyde de fer allant de -0,92 eV à -0,22 eV,

- les atomes de fer jouent un rôle majeur dans le processus d'adsorption,

- l'hydrogène H1 situé à proximité du chlore joue un rôle non négligeable de stabil-

isation,

- les positions horizontales des molécules de réfrigérant sont les plus stables avec une valeur d'énergie de liaison d'environ -0,92 eV,

- aucun phénomène de dissociation du réfrigérant sur l'hématite n'a été observé,

- entre la molécule R1233zd et la surface, seuls de petits échanges de charge sont obtenus avec une valeur maximale de 0,1e. Les molécules de R1233zd sont physisorbées sur les surfaces d'hématite $\alpha - Fe_2O_3(01\bar{1}2)$ et aucune chimisorption n'est observée. De plus, aucune rupture de la double liaison carbone-carbone n'est constatée.

Dans cette étude ab-initio, nous avons montré que la molécule R1233zd pouvait être fortement adsorbée sur une surface d'oxyde de fer. Cette adsorption a été caractérisée en considérant un ensemble de positions et d'orientations de la molécule au-dessus de la surface, recouvrant ce qui pourrait être trouvé dans un contact lubrifié. Ces informations sur la réactivité de la surface avec le réfrigérant, obtenues à partir des calculs DFT sont ensuite conservées dans un champ de force afin d'étudier des systèmes beaucoup plus grands avec des simulations de dynamique moléculaire, comme détaillé dans la prochaine section.

0.4 Dynamique Moléculaire : performance tribologique du R1233zd en extrême confinement

La dynamique moléculaire (DM) est une méthode numérique basée sur la résolution dans le temps de l'équation du mouvement de Newton sur tous les atomes interagissant dans un système moléculaire [23]. En DM, contrairement à la DFT, les interactions entre atomes sont décrites par des champs de force (FF, pour "force field") [23]. Puisque les simulations de DM sont dépendantes du temps, des phénomènes hors équilibre peuvent être explorés et un grand nombre de caractéristiques concernant le cisaillement de films minces (frottement, conductivité thermique, profil de vitesse, etc.) peuvent être obtenus [24, 25, 26, 11, 27, 28, 29]. C'est pour ces raisons que des simulations de DM sont réalisées dans ce projet pour caractériser des systèmes confinés sous cisaillement.

Comme indiqué dans le chapitre précédent, les coûts de calcul élevés nécessaires à la DFT empêchent son utilisation pour étudier de plus gros systèmes. C'est pourquoi, dans cette section, des simulations DM sont utilisées pour les systèmes à plus grande échelle afin d'étudier les comportements tribologiques dans différentes conditions extrêmes. En particulier, les effets des fortes interactions réfrigérant/hématite observées en ab-initio, sur la résistance du film dans le contact lubrifié, sont étudiés.

0.4.1 Modèle et méthodes

Tous les calculs de DM dans cette section sont effectués en utilisant le logiciel LAMMPS (version: 14 mai 2016) [30]. Des surfaces d'hématite d'orientation ($01\bar{1}2$) et avec des dimensions *(x × y × z)* d'environ 30 Å × 33 Å × 10 Å sont utilisées dans tous les calculs. Au lieu d'utiliser un champ de force de la littérature qui, dans le meilleur des cas, reproduirait approximativement les paramètres de mailles, chaque atome de la surface est relié avec un ressort à un atome virtuel situé à sa position d'équilibre. À 0 K, la surface virtuelle se superpose donc à la surface réelle. Aucune interaction n'est définie à l'intérieur de la surface virtuelle, entre les deux surfaces virtuelles, ou entre les surfaces virtuelles et le réfrigérant. Les seuls interactions avec les surfaces virtuelles sont les ressorts qui les relient aux surface réelles. La surface supérieure est obtenue par rotation de 180 degrés de la surface inférieure. Chaque surface est composée de 1080 atomes (sans compter les atomes virtuels).
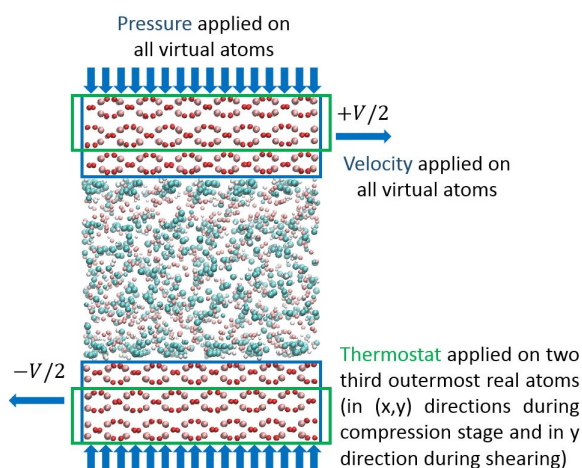
Figure 2: Représentation d'un système de R1233zd confiné entre deux surfaces d'hématite.

Le réfrigérant liquide est composé de 192 molécules, soit 1728 atomes. Le champ de force de Raabe est utilisé pour décrire les interactions du R1233zd [31, 32]. Dans la section précédente, la capacité d'adsorption du R1233zd sur la surface de l'hématite a été étudiée. Un champ de force a été adapté de ces résultats pour l'interface entre le réfrigérant et la surface. Le choix a été fait de transcrire les interactions entre le réfrigérant et la surface en utilisant deux potentiels, un potentiel de Coulomb et un potentiel de Lennard-Jones (LJ) 12-6 entre chaque paire d'atomes. L'algorithme d'intégration de Verlet est utilisé avec un pas de temps de 1 fs.

Toutes les configurations initiales sont obtenues avec le logiciel Moltemplate [33]. Un espace vide d'environ 30 Å dans la direction z entre les molécules de réfrigérant et la surface est établi initialement, afin de ne pas perturber la minimisation de l'énergie avant d'appliquer la charge normale. Comme ilustré sur la Figure 2, la pression $P_z = 500\,\text{MPa}$ est contrôlée en appliquant une force externe supplémentaire à la surface virtuelle de telle

sorte que chaque atome virtuel subisse la même force, et ainsi que la surface virtuelle se déplace de manière rigide. Après l'étape de compression, une vitesse $v_x = \pm \frac{v_s}{2}$ est imposée dans la direction x pour tous les atomes de la surface virtuelle avec une valeur $v_s = 20\,\text{m/s}$, tandis que la charge normale reste fixe. Un thermostat de Langevin avec un temps de relaxation de 0,1 ps est appliqué aux deux tiers des couches d'atomes les plus à l'extérieur des surfaces d'hématite, afin de les maintenir à une température de 283 K pendant tous les calculs de DM. Durant l'étape de cisaillement, le thermostat de Langevin est appliqué sur les deux surfaces d'hématite, mais uniquement perpendiculairement aux directions de cisaillement et de compression, donc seulement dans la direction y [34]. En effet, il a été montré que thermostater directement le fluide confiné peut conduire à des propriétés irréalistes [35]. La Figure 2 est une représentation d'un fluide R1233zd confiné entre deux surfaces d'hématite où les conditions mécaniques, ainsi que les thermostats, sont illustrés. Des premières simulations DM non détaillées ici nous permettent de conclure qu'une couche de molécules de R1233zd adsorbée apparaît aux parois, quelles que soient la vitesse de cisaillement (jusqu'à 100 m/s) et la pression (jusqu'à 4 GPa). Ce résultat peut être rapproché de l'observation expérimentale d'une tribocouche avec ce réfrigérant. De plus, cela montre la capacité de cette couche adsorbée à résister à des conditions de fonctionnement tribologiques extrêmes en pression, et en vitesse de cisaillement.

En régime de film complet, aucun contact entre les surfaces n'apparaît. Cependant, comme indiqué précédemment, les roulements utilisés pour la technologie PRL sont lubrifiés dans un régime de lubrification où l'épaisseur minimale du film atteint quelques nanomètres. Dans ce cas, la séparation des surfaces n'est pas garantie dans toute la zone de contact et des contacts entre aspérités peuvent se produire localement. Par conséquent, la prochaine section s'attèle à décrire le cas où les surfaces d'oxyde de fer sont très proches et seulement séparées par quelques couches de molécules de réfrigérant.

0.4.2 Vers la rupture du film de R1233zd entre surfaces lisses

La dégradation du film local peut être analysée en réduisant l'épaisseur du film jusqu'à un contact sec. La transition entre une bicouche et une monocouche incomplète est étudiée ici. Les propriétés structurales et tribologiques sont analysées au fur et à mesure que le nombre de molécules est réduit, molécule par molécule. L'orientation des molécules est considérée pour examiner la structure du film pendant les changements de nombre de couches. Enfin, les effets de la réduction de l'épaisseur sur le frottement sont discutés.

Pour décrire le processus conduisant à la formation de mono- et bicouche, l'orientation des molécules est analysée. Pour un ensemble donné de pression P, de vitesse de cisaille-

ment v_s et de nombre de molécules de réfrigérant dans le contact N_{zd}, 60 configurations de toutes les positions atomiques sont déterminées tout au long de l'étape de cisaillement de 3 ns, pour calculer les orientations moléculaires. Pour chaque configuration et molécule, l'angle $\alpha_{z\text{-}ClH2}$ entre les directions Cl-H2 et l'axe z est calculé. Les molécules sont ensuite classées selon la valeur de cet angle puis, les résultats sont moyennés sur tous les configurations. Le choix de cet angle est justifié en raison de sa capacité à représenter les molécules perpendiculaires où les atomes de chlore sont situés proches de la surface et les groupes CF_3 éloignés de l'interface. Une petite valeur de $\alpha_{z\text{-}ClH2}$ correspond donc à une molécule perpendiculaire à la surface inférieure. Une molécule est considérée comme perpendiculaire lorsque $\mid \alpha_{z\text{-}ClH2} \mid$ est inférieur à 30° ou compris entre 150° et 180°. La Figure 3 superpose la densité du film (en orange) et le pourcentage de molécules perpendiculaires (en bleu) entre les deux surfaces. Ces caractéristiques sont dessinées en fonction de N_{zd} à P = 0,5 GPa et pour une vitesse de cisaillement $v_s = 20\,\text{m/s}$
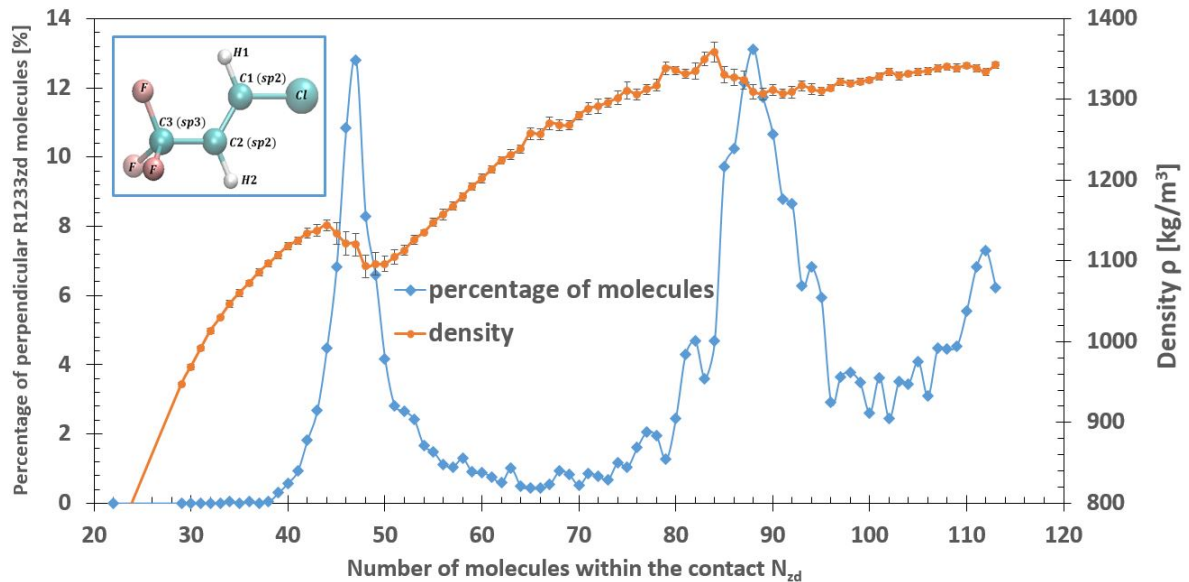
Figure 3: Pourcentage de molécules perpendiculaires (en bleu) en fonction du nombre total de molécules de réfrigérant dans le contact, en comparaison avec la densité (en orange), à P = 0,5 GPa et pour une vitesse de cisaillement $v_s = 20\,\text{m/s}$.

Ces courbes donnent des informations sur le processus de transition des dernières couches. En effet, lorsque la quantité de réfrigérant est progressivement réduite, la densité du film augmente brusquement juste avant d'atteindre une bicouche complète à 84 molécules ou avant une monocouche à 44 molécules. La signification physique de ces augmentations est que le volume diminue rapidement en réduisant le nombre de molécules. Ce processus peut être lié à l'orientation des molécules dans cette zone. En effet, le nombre de molécules perpendiculaires aux surfaces croît fortement au cours de ces deux augmentations de densité lorsque la quantité de réfrigérant est réduite. Ce pourcentage de molécules perpendiculaires s'élève au maximum à environ 13% du nombre total

de molécules. Il correspond à la tendance des molécules à relier les couches (par des ponts) jusqu'à la fusion des couches en une seule. Ensuite, ce pourcentage diminue fortement et seulement 4% du nombre total des molécules sont orientées perpendiculairement lorsqu'une mono- ou bicouche complète est atteinte. En réduisant encore la quantité de réfrigérant après avoir atteint la monocouche, le pourcentage de molécules perpendiculaires atteint zéro en raison d'une orientation plate des molécules restantes.

À l'échelle nanométrique, la structure du film est très différente de celle d'un fluide en volume et la densité, ainsi que les profils de vitesse, peuvent fournir des informations supplémentaires à la compréhension des phénomènes. La molécule R1233zd est composée de plusieurs types d'atomes avec différentes masses molaires. Ainsi, afin de mieux représenter la distribution des atomes à travers l'épaisseur du film, la densité définie comme le nombre de particules par unité de volume, est calculée à la place de la densité massique. La Figure 4 représente quatre cas caractéristiques de structuration et de dynamique particulière à travers l'épaisseur du film, à une pression appliquée de 0,5 GPa. En réduisant la quantité de réfrigérant, le cas a) décrit une bicouche complète (8,4 molécules par nm^2) ; le cas b) (5,0 molécules par nm^2) représente le N_{zd} le plus élevé pour lequel un glissement aux parois apparaît ; le cas c) est représentatif d'une monocouche complète (4,4 molécules par nm^2); enfin, le cas d) représente une monocouche à moitié remplie, soit 2,2 molécules par nm^2.

Pour une bicouche complète (cas a), les molécules de réfrigérant se situent dans une épaisseur de film d'environ 10 Å. Dans ce cas, les deux couches sont accrochées chacune sur la surface la plus proche, en raison des interactions interfaciales élevées. Par conséquent, le profil de vitesse montre que le cisaillement se produit entre les deux couches (localisation centrale). Il est particulièrement intéressant de souligner que les deux couches de R1233zd sont toujours adsorbées sur les surfaces, même à un taux de cisaillement extrêmement élevé (supérieur à $10^{10}\,\mathrm{s}^{-1}$). Cette remarque contribue à expliquer pourquoi une couche protectrice est attendue même dans des conditions sévères de fonctionnement, comme observé expérimentalement [4, 5]. Cela permet également de caractériser la limite de lubrification avec un tel réfrigérant. Le cas b représente la première situation où un glissement se produit à la paroi réfrigérant/surface. En effet, on observe une chute de la vitesse entre la surface et le réfrigérant au niveau de la paroi. Plus spécifiquement, à l'interface fluide/surface inférieure (à z = 10 Å), le point bleu situé directement après l'interface a une vitesse différente de celle de la surface. Cependant, cette chute de vitesse est moins distincte à l'interface avec la surface supérieure (à z = 17,4 Å), où une faible adsorption semble persister. Au milieu du profil de densité, le nombre d'atomes est plus grand que dans le cas a (bicouche complète), ce qui signifie que des ponts apparaissent entre les deux couches. En conséquence, l'épaisseur de chacune des deux couches est réduite ; cela est représenté par une largeur des pics de densité qui diminue. Le cas c décrit une monocouche complète où un large glissement
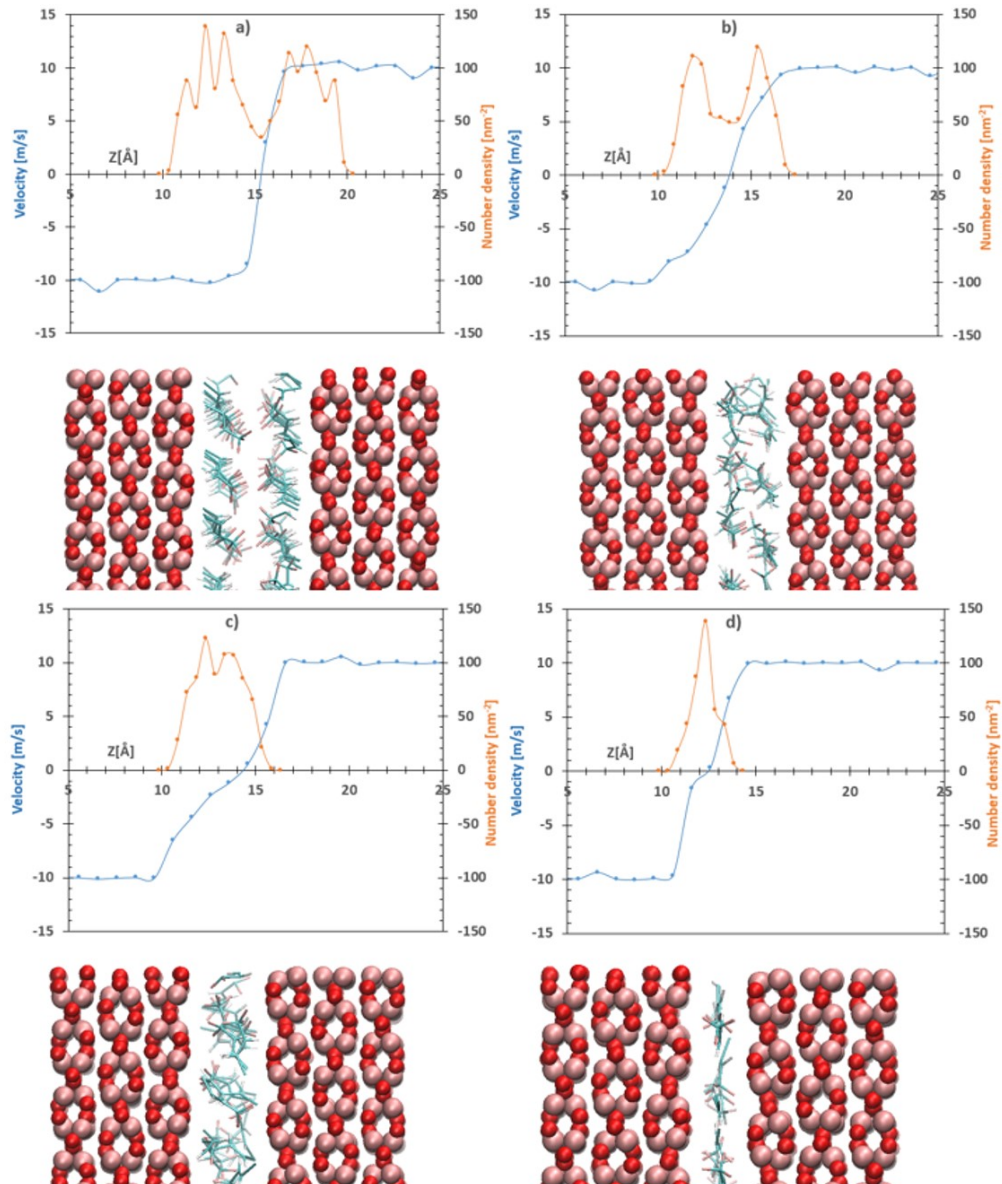
Figure 4: Profils de densité et de vitesse dans l'épaisseur du film pour quatre N_{zd} différents – a)$N_{zd} = 84$, b)$N_{zd} = 50$, c)$N_{zd} = 44$, d)$N_{zd} = 22$ – à 0,5 GPa, avec une vitesse de cisaillement de 20 m/s and une température de la surface fixée à 283 K.

aux parois est observé. Une partie de la différence de vitesse entre les surfaces et le réfrigérant est absorbée par le cisaillement de la monocouche elle-même, les molécules se déplaçant indépendamment les unes des autres. Dans le cas d, le pic de densité est plus mince car les molécules sont orientées de façon plane, comme détaillé précédemment, et le glissement à la paroi est prédominant.

La Figure IV.8 représente la variation de la contrainte de cisaillement τ et de la densité en fonction de N_{zd}, à P = 0,5 GPa.
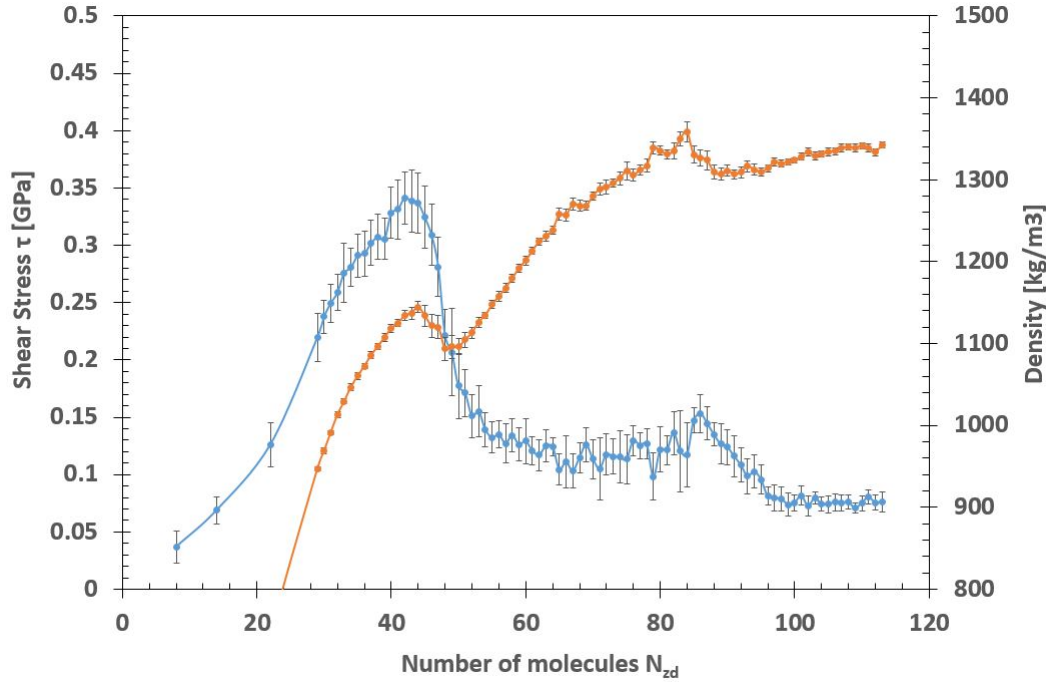
Figure 5: Densité du film (orange) et contrainte de cisaillement τ (bleu) en fonction du nombre de molécules de réfrigérant N_{zd} à l'intérieur du contact, pour P = 0,5 GPa

En partant du point le plus à droite de la figure, correspondant au maximum du nombre de molécules, lorsque la quantité de réfrigérant est réduite, la contrainte de cisaillement τ augmente, correspondant à une augmentation du nombre de molécules perpendiculaires aux surfaces reliant les couches (voir Figure 3), avant d'atteindre une bicouche complète. En continuant à réduire le nombre de molécules de réfrigérant, la contrainte de cisaillement diminue légèrement en raison de la diminution du nombre de molécules qui s'opposent au mouvement des surfaces. Avec deux couches distinctes dans le film, un minimum local de contrainte de cisaillement est observé. Ensuite, τ augmente fortement jusqu'à l'obtention d'une monocouche. Lors de cette augmentation, les deux couches se confondent progressivement en une monocouche unique et donc le pourcentage de molécules perpendiculaires qui relient les deux couches augmente (voir Figure IV.6). Dès que les deux couches fusionnent en une couche à 5,0 molécules par nm^2, le film de réfrigérant est cisaillé et glisse sur les deux parois.

Une valeur maximale de τ est obtenue pour une monocouche séparant les surfaces. À

ce stade, le glissement aux parois est inévitable. En effet, les deux surfaces se déplacent dans des directions opposées et le cisaillement ne se produit qu'à l'intérieur d'une couche de réfrigérant. Par conséquent, seules les interactions interfaciales réfrigérant/surface déterminent le comportement en frottement. En conséquence de la paramétrisation du champ de force à l'interface, le terme ε du potentiel de Lennard-Jones est élevé pour représenter la capacité d'adsorption de la molécule de R1233zd sur les surfaces d'hématite. Ces fortes interactions conduisent à une contrainte de cisaillement très élevée $\tau = 0{,}34\,\mathrm{GPa}$ à P = 0,5 GPa. De plus, l'épaisseur du film étant très faible avec seulement une monocouche séparant les deux surfaces, l'adhérence entre les deux surfaces, dues aux forces de Van der Waals et aux interactions électrostatiques, peut augmenter le frottement [36].

Ensuite, la contrainte de cisaillement τ diminue lorsque le nombre de molécules de réfrigérant est réduit davantage. Moins de molécules de R1233zd doivent être cisaillées, impliquant une plus faible résistance au mouvement des surfaces et donc une force tangentielle inférieure. Par conséquent, un τ inférieur est trouvé en comparaison avec une monocouche complète.

La prochaine section a pour but de considérer un contact entre une aspérité et une surface lisse afin d'étudier la résistance de la couche adsorbée dans des cas extrêmes plus réalistes. En effet, la rugosité peut avoir un impact sévère sur la structure et l'écoulement du fluide nanoconfiné [37].

0.4.3 Structure et rupture du film avec surfaces rugueuses

La conception de la rugosité et son implication sur le système sont tout d'abord expliquées. Ensuite, la structure et la résistance de la couche adsorbée située dans la zone de contact avec la rugosité seront étudiées à différentes pressions et vitesses de cisaillement. Pour analyser les effets de rugosité, des systèmes plus grands que ceux considérés précédemment doivent être utilisés. Dans les systèmes réels, la rugosité quadratique moyenne (RMS) peut atteindre plusieurs nanomètres [3] mais pour limiter les coûts de calculs, nous considérerons ici un système plus petit et représentatif du sommet d'une aspérité. Une surface $(01\bar{1}2)$ d'hématite, avec des dimensions $(x \times y \times z)$ environ égales à 205 Å $\times$ 33 Å $\times$ 10 Å, est utilisée dans cette section pour la surface supérieure. De plus, la surface inférieure est construite en déformant sa forme avec une fonction gaussienne d'amplitude A = 15 Å, comme suit.

$$Z_{\mathrm{rugosité}} : x \longmapsto Z_{\mathrm{init}} + A e^{-\frac{(x - \frac{L_x}{2})^2}{2\sigma^2}} \tag{2}$$

Où σ est choisi pour avoir une largeur à mi-hauteur $H = 2\sqrt{2ln(2)}\sigma = \frac{L_x}{4}$ avec L_x la

longueur totale de la surface de 205 Å, Z_{init} la coordonnée initiale suivant la direction z de chaque atome et $Z_{\text{rugosité}}$ les nouvelles coordonnées suivant la direction z. Cette fonction est également appliquée aux atomes de la surface virtuelle. La longueur de la surface est choisie assez grande pour augmenter le rayon de courbure au sommet, donné par $\frac{\sigma^2}{A} = 31$ Å.

Différentes quantités de molécules de réfrigérant ont été testées pour assurer une couche adsorbée répartie sur toute la surface mais également pour permettre qu'une bulle reste piégée entre les parties planes des surfaces après compression et pour chaque pression. Le but de cette procédure est de s'assurer que nous testons bien la résistance de la couche adsorbée, et non la compressibilité du fluide. 600 molécules de R1233zd sont mises en place dans le système et chaque surface est composée de 7200 atomes (sans compter les atomes virtuels). Les deux étapes de compression et de cisaillement durent 5 ns chacune. Contrairement aux précédentes études de DM, seule la surface supérieure se déplace. Des pressions de 50 MPa à 3 GPa sont appliquées à la surface supérieure virtuelle. La vitesse est appliquée suivant la direction x pour tous les atomes virtuels de la surface supérieure avec une valeur de la vitesse de cisaillement v_s variant de 2 m/s à 50 m/s.

Les effets de la vitesse de cisaillement sur la résistance et la structure de la couche adsorbée sont analysés. Quatre vitesses de cisaillement différentes (2, 5, 10, 50) m/s sont considérées avec les pressions suivantes: 0,05, 0,1, 0,3, 0,5, 1, 1,5, 2, 3 GPa. Comme la force entre les deux surfaces est transmise à travers une très petite zone de contact, la pression locale dans cette zone est beaucoup plus grande que la pression moyenne imposée dans les simulations. Pour estimer la pression locale dans la zone de contact, la méthodologie suivante est utilisée pour mesurer la longueur de contact, comme indiqué sur la Figure 6.

Comme la surface inférieure ne bouge pas, le pic de rugosité reste localisé à la position x_0, qui correspond au milieu de la longueur totale $L_x = 205$ Å de la boîte de simulation. Considérant la sortie du divergent de la région de contact avec l'aspérité, une zone de vide peut être identifiée à partir de la position x_c (voir Figure 6). Une estimation grossière de la longueur réelle du contact L_c est proposée comme $L_c = 2(x_c - x_0)$. À partir de la pression P appliquée uniformément sur les atomes de la surface supérieure virtuelle, on peut déduire la pression de contact effective P_c comme:

$$P_c = P\frac{L_x}{L_c}, \tag{3}$$

où la limite de contact x_c varie autour de 118 Å, correspondant à un rapport $\frac{L_x}{L_c}$ constant pour tous les cas: $\frac{L_x}{L_c} = 6{,}6$. P_c représente une estimation approximative de la pression réelle subie par les couches de réfrigérant, à des fins de comparaison.
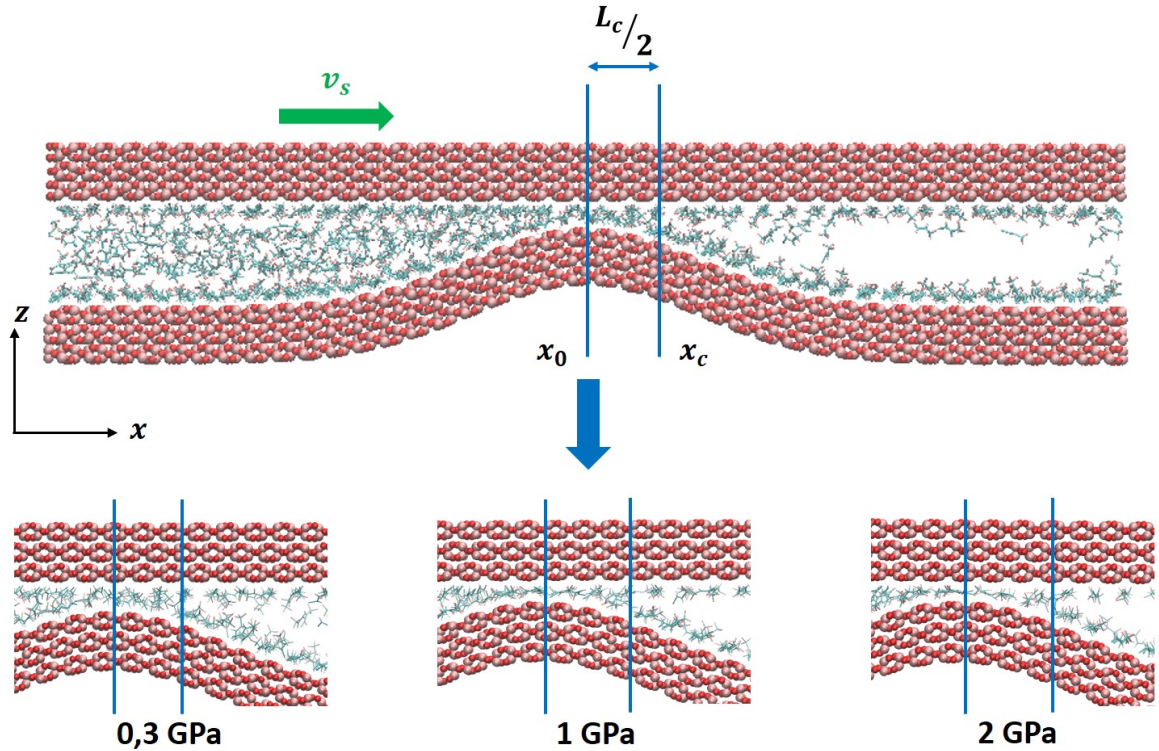
Figure 6: Estimation visuelle de la zone de contact utilisée pour estimer la pression de contact par rapport à la pression appliquée globalement.

Le Tableau 2 rassemble les informations sur la résistance et la structure des couches de réfrigérant sous compression et cisaillement. De plus, les pressions estimées P_c dans la zone de contact sont fournies.

À P = 0,05 GPa ($P_c \approx 0,3\,\text{GPa}$), la bicouche résiste. Pour le cas intermédiaire avec P = 0,1 GPa ($P_c \approx 0,7\,\text{GPa}$), une vitesse de cisaillement v_s élevée, qui est ici égale à la vitesse d'entraînement du fluide dans le contact, est bénéfique pour conserver la formation d'une bicouche ($v_s = 10\,\text{m/s}$ et $50\,\text{m/s}$). Au contraire, pour des petites vitesses, le mouvement de cisaillement tend à déstabiliser la structure en bicouche qui perdurait en régime stationnaire sans cisaillement, et donc à favoriser une monocouche. A plus hautes pressions, aucune bicouche n'est observée.

Pressure [GPa]		Sliding velocity Vs [m/s]			
Applied	Estimated in the contact area	2	5	10	50
0.05	0.3	Bilayer	Bilayer	Bilayer	Bilayer
0.1	0.7	Monolayer	Monolayer	Bi-Monolayer transition	Bilayer
0.3	2.0	Discontinuous	Monolayer	Monolayer	Monolayer
0.5	3.3	Discontinuous	Discontinuous	Monolayer	Monolayer
1	6.6	Discontinuous	Discontinuous	Discontinuous	Monolayer
1.5	9.9	Discontinuous	Discontinuous	Discontinuous	Discontinuous
2	13.2	Breakdown	Discontinuous	Discontinuous	Discontinuous
3	19.8	Breakdown	Breakdown	Breakdown	Breakdown

Table 2: Résistance et structure des couches adsorbées compressées et cisaillées à l'intérieur d'un contact lisse/rugueux, à 0,05, 0,1, 0,3, 0,5, 1, 1,5, 2, 3 GPa et à des vitesses de cisaillement de 2, 5, 10, 50 m/s.

La Figure 7 représente une vue du dessus de la zone de contact où les deux surfaces sont cachées, dans différentes configurations typiques. En particulier, à P = 0,3 GPa ($P_c \approx 2\,\text{GPa}$) pour la plus petite vitesse de cisaillement ($v_s = 2\,\text{m/s}$), et à P = 0,5 GPa ($P_c \approx 3,3\,\text{GPa}$) et $v_s = 2\,\text{m/s}$ ou $v_s = 5\,\text{m/s}$, le film réfrigérant est légèrement discontinu. Plus spécifiquement, des trous de dimensions égale à celles d'une molécule seule, peuvent apparaître dans la zone de contact. De P = 1 GPa ($P_c \approx 6,6\,\text{GPa}$) à P = 2 GPa ($P_c \approx 13,2\,\text{GPa}$), le film de réfrigérant est principalement discontinu. Comme illustré sur la Figure 7 (b), les molécules parviennent à entrer dans la zone de contact une par une, mais des espaces importants apparaissent entre elles. Le phénomène d'entraînement hydrodynamique est aussi observé à P = 1 GPa ($P_c \approx 6,6\,\text{GPa}$) et $v_s = 50\,\text{m/s}$ où une monocouche est formée alors qu'un film discontinu apparaît à une vitesse inférieure, et à P = 2 GPa ($P_c \approx 13,2\,\text{GPa}$), où $v_s = 2\,\text{m/s}$ n'est pas suffisant pour entraîner des molécules à l'intérieur de la zone de contact, alors que c'est le cas pour des vitesses plus élevées.

Enfin, la rupture complète du film se produit pour toutes les vitesses à P = 3 GPa ($P_c \approx 19,8\,\text{GPa}$). Les simulations sont arrêtées lorsqu'il y a une rupture totale du film de réfrigérant, et donc un contact direct entre les surfaces. La Figure 7 (c) montre la vue de dessus du contact juste avant l'arrêt de la simulation, donc juste avant le contact des surfaces. Bien que les pressions locales estimées dans la région de contact semblent très élevées, la situation est similaire dans les systèmes réels, où la pression locale du contact entre les aspérités peut largement dépasser la pression globale appliquée.
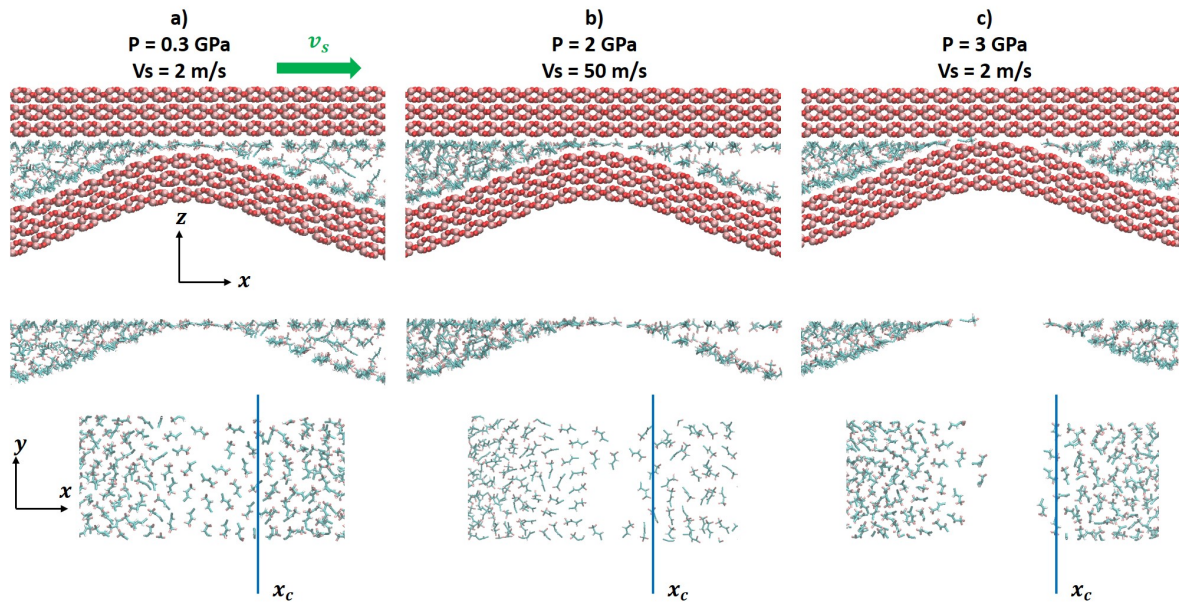
Figure 7: Vue du dessus de la zone de contact au niveau du sommet de la rugosité (les deux surfaces sont cachées). Discontinuité légère (a) à P = 0,1 GPa ($P_c \approx 0,7\,\text{GPa}$) et $v_s = 2\,\text{m/s}$. Discontinuité forte dans le film (b) à P = 2 GPa ($P_c \approx 13,2\,\text{GPa}$) et $v_s = 50\,\text{m/s}$. Figure représentant l'étape de simulation précédant la rupture totale du film (c) à 3 GPa ($P_c \approx 19,8\,\text{GPa}$) et $v_s = 2\,\text{m/s}$.

0.5 Conclusion générale

En utilisant une approche de modélisation multi-échelles, cette thèse a exploré l'influence de la physicochimie à l'interface entre un réfrigérant et une surface d'oxyde de fer sur la performance tribologique dans un contact lubrifié, sous des conditions de lubrification avec réfrigérant pur (PRL).

Tout d'abord, des calculs quantiques basés sur la théorie de la fonctionnelle de la densité (DFT) ont été réalisés afin d'étudier l'adsorption du réfrigérant R1233zd sur la surface d'oxyde de fer. Les molécules de R1233zd sont physisorbées sur des surfaces d'hématite $\alpha - Fe_2O_3(01\bar{1}2)$ et aucune chimisorption et aucune rupture de double liaisons carbone-carbone ne sont observés. De plus, la dissociation du réfrigérant à l'approche de la surface n'est pas constatée. Seuls de faibles échanges de charge sont trouvés entre la molécule R1233zd et la surface, avec une valeur maximale de 0,1e. Une gamme de valeurs d'énergies de liaison allant de -0,92 eV à -0,22 eV est observée avec seize orientations et positions différentes de la molécule R1233zd sur le dessus de la surface. Les positions horizontales des molécules de réfrigérant sont les plus stables avec une valeur d'énergie de liaison d'environ -0,92 eV. Les atomes de fer jouent un rôle majeur dans le processus d'adsorption et l'hydrogène H1 situé à proximité du chlore joue un rôle non négligeable de stabilisation.

Ces résultats ab-initio sont ensuite utilisés pour paramétrer un champ de forces à l'interface réfrigérant-surface qui est utilisé dans des simulations à plus grande échelle à l'aide de la dynamique moléculaire (DM). Avec ces simulations, une couche adsorbée de R1233zd sur les surfaces d'oxydes de fer est observée, corroborant les résultats expérimentaux. La résistance de cette couche adsorbée et sa capacité à protéger la surface contre l'usure sont testées. Les simulations de DM ont permis d'étudier des cas tribologiques différents, des conditions les moins extrêmes à celles les plus sévères. La première étude de cas a considéré une épaisseur de film de 2,1-2,5 nm, confinée entre deux surfaces atomiquement lisses sous une pression normale allant jusqu'à 4 GPa et avec une vitesse de cisaillement allant jusqu'à 100 m/s. La principale découverte est qu'une couche de R1233zd reste adsorbée sur les deux surfaces d'oxyde de fer, quelles que soient les conditions opératoires testées. Ceci est cohérent avec l'analyse XPS réalisée sur des surfaces de roulements réels dans diverses conditions.

La deuxième étude de cas considère une épaisseur de film ultra-mince de 1,5 nm à 0,5 nm, avec des surfaces lisses, une pression P = 0,5 GPa et une vitesse de cisaillement $v_s = 20\,\mathrm{m/s}$. Dans ces conditions, le film de réfrigérant développe des couches parallèles aux surfaces. Avec 8,4 molécules de R1233zd par nm², deux couches saturées sont formées, chacune adhérant à la surface la plus proche. Dans ce cas, le cisaillement se localise dans la partie centrale du film et est représenté par un plan de glissement

entre les deux couches. Avec deux couches distinctes dans le film, un minimum local de contrainte de cisaillement est observé. Cependant, lorsque le nombre de molécules diminue, des molécules perpendiculaires aux surfaces sont observées, et les deux couches se confondent progressivement en une seule monocouche. La contrainte de cisaillement augmente fortement pendant cette transition, et le maximum est atteint lorsque la monocouche est saturée, avec 4,4 molécules par nm^2 à P = 0,5 GPa, et 4,7 molécules par nm^2 à P = 1,5 GPa. Dès que les deux couches fusionnent en une monocouche, le film de réfrigérant est cisaillé, accompagné de glissement aux parois.

Enfin, la troisième étude de cas visait à représenter un contact plus réaliste. Une aspérité longitudinale rigide de forme gaussienne est créée sur une surface fixe, tandis que l'autre surface est lisse. Au repos, donc sans cisaillement, sous une pression maximale de P = 3 GPa (c'est-à-dire une pression de contact moyenne $P_c \approx 19{,}8\,\text{GPa}$) le film de réfrigérant supporte la charge normale. Une transition apparaît à P = 0,3 GPa ($P_c \approx 2\,\text{GPa}$) où la structure du film passe d'une bicouche à une monocouche. Lorsqu'une vitesse de cisaillement est appliquée, la résistance du film de réfrigérant décroît. Pour la vitesse de cisaillement la plus faible, la transition de la bicouche à la monocouche apparaît à P = 0,05 - 0,1 GPa ($P_c \approx 0{,}3-0{,}7\,\text{GPa}$), et la monocouche se divise en molécules individuelles entrant une à une dans le contact à partir de P = 1 GPa ($P_c \approx 6{,}6\,\text{GPa}$). Ici, la vitesse de cisaillement imposée représente également la vitesse d'entraînement hydrodynamique des molécules de R1233zd dans la zone de contact, ce qui explique pourquoi le film de réfrigérant, à une valeur de P = 1 GPa ($P_c \approx 6{,}6\,\text{GPa}$), résiste mieux à des vitesses plus élevées. A P = 3 GPa ($P_c \approx 19{,}8\,\text{GPa}$), la rupture totale du film apparaît à n'importe quelle vitesse de cisaillement testée, et les surfaces solides se touchent.

Contents

Contents

3

List of Figures

List of Tables

9

Main abbreviations

DFT   Density Functional Theory

EHL   Elasto-Hydrodynamic Lubrication

FF   Force Field

GWP   Global Warming Potential

HCFO   HydroChloroFluoroOlefin

HFO   HydroFluoroOlefin

MD   Molecular Dynamics

ODP   Ozone Depletion Potential

PRL   Pure Refrigerant Lubrication

VTF   Very Thin Film

Introduction

Lubrication consists in introducing a lubricant between two surfaces in contact moving one with respect to the other in order to reduce friction and wear. By reducing the stress between moving elements, this process improves the life of mechanical components. Nonetheless, lubrication often requires a heavy design – with for example addition of lubricant pumps, while the actual trend is to decrease the weight of mechanical systems. In large refrigeration systems, using the working fluid – here the refrigerant – as lubricant instead of oils simplifies the design. However, refrigerants are low-viscosity fluids. As a consequence, the lubricant film thickness separating the surfaces can reach the nanometric scale locally, and thus be on the same order of magnitude as surface roughness.

In this very thin film regime of lubrication, few refrigerant molecules separate the asperities. In this context, fluid/surface physical chemistry is of primary importance for the control and optimization of the tribological performance of the system. Among many existing refrigerants, R1233zd has been developed to replace environmentally harmful ones. The literature reports that an adsorbed layer of R1233zd refrigerant molecules was observed on steel bearing surfaces under pure refrigerant lubrication conditions, suggesting good tribological performances.

Nonetheless, the severe operating conditions of lubricated contacts such as confinement and high pressure make experimental in situ analysis very difficult. Therefore, this work presents a multiscale modeling approach to explore the tribological performance of a pure refrigerant (R1233zd) lubricated contact confined between steel surfaces.

First, density functional theory (DFT) calculations will analyze the refrigerant/surface chemical physics. Second, large-scale molecular dynamics (MD) simulations, parametrized with the help of the DFT results, will study the structure and dynamics of the confined refrigerant under severe tribological conditions.

This manuscript contains four chapters.

Chapter 1 provides an overview of the scientific and industrial contexts of this thesis. The refrigeration systems are introduced and a historical overview of the development of refrigerants is presented. Then, the lubrication in refrigeration compressors is discussed,

involving either an oil-refrigerant mixture or pure refrigerant. Under these conditions, molecular lubrication regime prevails. Moreover, the ability of some refrigerants to adsorb on surfaces is reviewed. To conclude this Chapter, the objectives of this PhD are exposed.

Chapter 2 is dedicated to quantum calculations with the DFT. First, the principles of DFT are explained. Then, our model is detailed. The choice to consider hematite ($\alpha - Fe_2O_3$) representative of bearing steel surfaces is presented. Finally, R1233zd molecule adsorption on hematite surfaces is discussed. Binding energies are derived from these calculations under different conformations. Moreover, the type of the observed sorption is determined from a charge analysis.

Chapter 3 develops the principles of MD simulations used for larger scale systems. In MD, interatomic interactions are described by empirical potentials, often referred to as force fields (FF). Classical FF for the refrigerant and the surface are described. Afterwards, the methodology used to parametrize a FF dedicated to the refrigerant-surface interface based on the previous DFT results is presented. This approach is then implemented in large-scale MD simulations of R1233zd molecules confined between two hematite ($\alpha - Fe_2O_3$) surfaces. The existence of an adsorbed layer is then studied numerically. Moreover, orientations of the molecules at the refrigerant/surface interface are discussed.

Chapter 4 exploits the parametrized FF to study the tribological behavior of R1233zd confined between smooth surfaces under extreme conditions. The strength of the adsorbed layer is tested and friction is evaluated on a range of pressures and sliding velocities. Reducing the amount of confined refrigerant, one molecule at a time, structure, flow, and friction are investigated, until the film breaks down locally. Afterwards, contact between a rough surface and a smooth surface is studied, where the local pressure supported by the refrigerant film is far bigger.

This manuscript ends with a general conclusion, where the main results of this thesis throughout the different chapters are gathered and perspectives arise.

Chapter I

Context and State of the art

Contents

This chapter provides a thread guiding the reader to the objectives of this PhD thesis. First, refrigeration systems are introduced. Second, a historical overview of the development of refrigerants is presented to explain the choice made in this project to study the HCFO-1233zd(E) refrigerant. Then, lubrication in refrigeration compressors, from classical lubrication with oil-refrigerant mixtures to the new pure refrigerant lubrication (PRL) technology, is detailed. Moreover, the lubrication regimes reached in refrigeration systems are exposed. The fourth section is dedicated to molecular lubrication. A literature review concerning the ability of some refrigerants to be adsorbed on the surface is performed. To conclude, the objectives of this PhD are presented.

I.1 Refrigeration systems

Refrigeration is the process in which the temperature of an enclosed space is reduced by heat removal. Refrigerants are fluids used in several different kinds of systems, such as heating, ventilation, air conditioning and refrigeration equipments. While in 1955, air conditioning systems were only equipping 2% of American residences, the amount increased continuously and reached 87% in 2015[38, 39]. The same rate of air conditioning increase can be found for urban chinese households[40, 41].

Vapor-compression refrigeration systems are the most widely used for air-conditioning of large buildings. In these systems, the refrigerant is the working fluid, which takes heat from an enclosed space and rejects it elsewhere. As represented in Figure I.1, these systems are composed of four main components: a compressor, a condenser, an expansion valve and an evaporator.
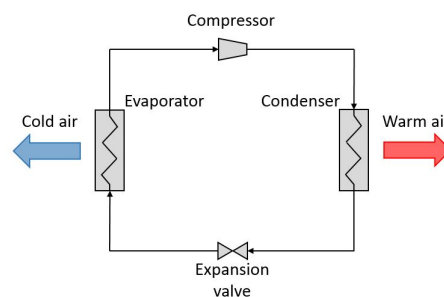
Figure I.1: Vapor-compression refrigeration system.

In this cycle, the flowing refrigerant enters the compressor as a saturated vapor, and is compressed to a higher pressure, resulting in a higher temperature as well. This compressed and hot vapor (superheated vapor) is then condensed thanks to cooling air or water flowing across tubes in the condenser. Hence, this component of the global system enables to reject heat into the cooling air/water. Afterwards the condensed liquid refrigerant (saturated liquid) is going through the expansion valve. This component

is a flow-restricting device in which the working fluid undergoes a pressure reduction resulting in an adiabatic flash evaporation of a fraction of the liquid refrigerant, associated with a temperature decrease. Finally, in the evaporator, a fan circulates the warm air from the enclosed space across coils or tubes carrying the cold refrigerant mixture. That warm air evaporates the liquid part of the mixture, so that the refrigerant exit the evaporator as a saturated vapor. The evaporator is where the circulating refrigerant absorbs heat from the enclosed space. The refrigeration cycle is then completed. In this project, we only investigate the compressors.
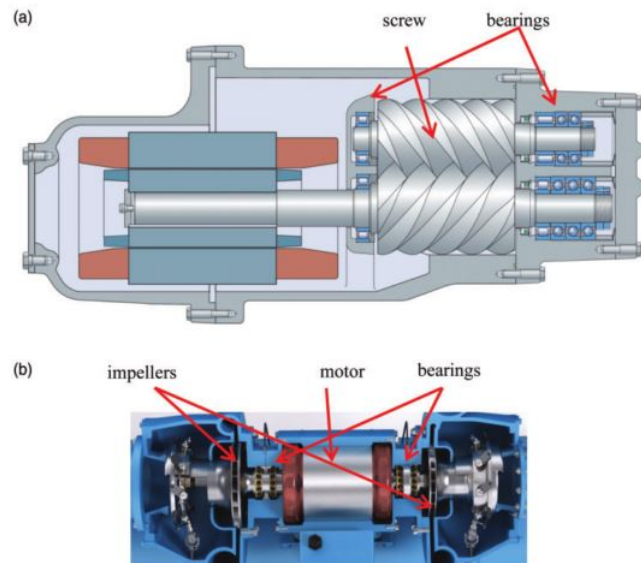
Figure I.2: Two kinds of refrigerant compressor: a) screw compressor and b) centrifugal compressor [2].

The compressor is a system compressing gas, thus rising the pressure. Two main techniques can be distinguished, as shown in Figure I.2[2]:

- the positive displacement compressors: the volume available for the gas is reduced in order to increase the pressure. It is for example the case with the screw compressor, as shown in Figure I.2[2]. The gas is mechanically displaced through screws, named rotors, and compressed. The compressed gas is then ejected of the compressor at the end of the screws. The radial and axial position of the rotors is maintained by bearings, which are also supporting rotors load.

- the dynamic turbo-machinery: the gas is accelerated to high velocity in a continuous flow and kinetic energy is converted to an increased pressure. The two main sort of dynamic turbomachines are the axial and centrifugal compressors. The last one is sometimes also called radial compressor. The difference between these two turbomachines is the direction of the flow through the system. The centrifugal compressor is shown in Figure I.2[2]. It is one of the most widely used in refrigeration industry. In centrifugal compressors, the gas is accelerated through rotating

18

impellers and the pressure is increased by slowing the flow through a diffuser. The compressed gas is then ejected through a nozzle.

Compressors used to cool down huge buildings can be either screw or centrifugal compressors. Both are using rolling element bearings, and both are relying on refrigerants as a working fluid.

I.2 The refrigerants

In order to understand the origin of this project, a historical overview of refrigerants market trends is required. Indeed, international regulations have affected from time to time the development of refrigerants. Hence, industrial manufacturers proposed alternatives refrigerants to the environmentally harmful old ones. In this section, the different families of refrigerants are presented.

I.2.1 The refrigerants and their strong environmental impact

The refrigerants are classified into several families according to the different kinds of atoms and molecular structures of the refrigerant. They will be introduced in this section by tracking their temporal appearance. Figure I.3[42] illustrates the different stages of refrigerants use from the beginning until now with the fourth generation. In order to explain Figure I.3, the different generations of refrigerants are detailed below.
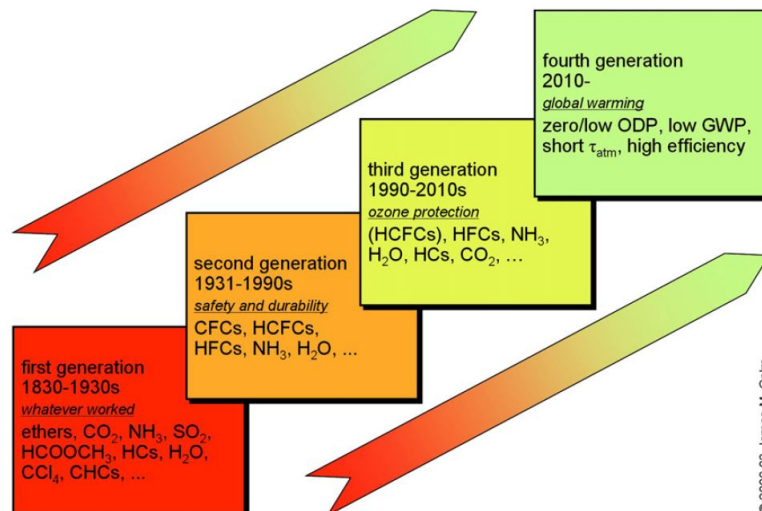
Figure I.3: Refrigerants evolution [42].

First generation: whatever worked

For about a century (1830-1930), the first generation of refrigerants, named "whatever worked" in Figure I.3, was used for refrigeration and air conditioning systems. These refrigerants are composed of molecules such as carbon dioxide CO_2, ammonia NH_3 (widely used in industrial refrigeration), sulfure dioxide SO_2 (used in home refrigerators), hydrocarbons (HCs). However, the flammable and toxic behavior of some molecules led to accidents [42, 43].

Second generation: safety and durability

The growth of refrigeration market forced industry to propose safer synthetic alternatives composed of chlorofluorocarbons (CFCs) and hydrochlorofluorocarbons (HCFCs). This generation being safer than the first generation of refrigerant, the number of accidents decreased [2]. In refrigeration compressors, the low-pressure trichlorofluoromethane (CFC-11), the medium-pressure dichlorodifluoromethane (CFC-12) and the chlorodifluoromethane (HCFC-22) were mainly used[2]. The "low-pressure" aptitude, e.g. for CFC-11 refrigerant, arises from the high boiling point of the fluid, which thus can work at low pressure without evaporation. Hence, the CFC-12 and HCFC-22, having a lower boiling point, are named "medium-pressure" refrigerants, because they need a higher operating pressure than the CFC-11, meaning that the mechanical design is more complex.

Unfortunately, some of these refrigerants were harmful to the environment. Thanks to the publication of Molina and Rowland in 1974 [44], efforts were made concerning environmental impact recognition of chlorofluorocarbons (CFCs). In particular, it was shown that CFCs and HCFCs molecules deplete the ozone layer, which protects life on earth against harmful ultraviolet radiations. Indeed, due to stratospheric ultraviolet radiation, CFCs release chlorine atoms Cl [45], which catalyze the conversion of ozone into O_2 [44]. In order to quantify the ozone depleting behavior, the ozone depletion potential was introduced.

The *Ozone Depletion Potential* (ODP) describes the destruction effect of the ozone layer by ozone depleting substances (ODS). The tricholorofluoromethane CFC-11 is taken as the reference with an ODP value of 1, to calculate the ODP of other substances. As detailed below, this parameter was used to phase down some refrigerants classified as ODS. The substances with low ODP values are preferred. In the following section, the ODP is used in Table I.1 to differentiate the different generations of refrigerants. The ODP parameter was used to justify the phase-out of CFCs and some HCFCs during the Montreal Protocol in 1987 because they were depleting the ozone layer[46].

Third generation: ozone protection

Hydrofluorocarbons (HFC) with zero ODP and new HCFCs with low ODP were proposed as alternative refrigerants. The 1,1,1,2-tetrafluoroethane HFC-134a replaced the CFC-12 in automotive air-conditioning systems[47]. The 2,2-Dichloro-1,1,1-trifluoroethane HCFC-123, with its very low ODP, became a substitute for CFC-11 in building refrigeration systems [2, 48]. However they were characterized as greenhouse gases because of long atmospheric lifetime, due to their low chemical reactivity with atmosphere. In order to quantify this effect, the global warming potential is introduced.

The *Global Warming Potential* (GWP) is used to measure greenhouse effect of a gas relative to carbon dioxide CO_2, which has a GWP value of 1. This parameter is calculated over a given time period. For example GWP100yr is the GWP value over 100 years. The larger the GWP, the more a gas will participate to Earth warming in comparison with CO_2 [49]. Therefore, gases with lowest GWP values are preferred. For example, HFC-134a has a GWP of around 1360 [50]. In the following section, the GWP is used in Table I.1 to differentiate the different generations of refrigerants.

With the Kyoto Protocol signed in 1997, some countries agreed on the reduction of greenhouse gases. However major countries did not sign, and the protocol was never entirely implemented [2]. More recently on 15th October 2016, 197 countries adopted in Kigali an amendment of the Montreal Protocol to phase down HFCs[51]. New refrigerants are developed in order to replace them. This fourth generation of refrigerants is composed of Hydrofluoroolefins (HFOs) and Hydrochlorofluoroolefins (HCFOs).

I.2.2 The fourth generation of refrigerants: HFOs and HCFOs family

Hydrofluoroolefins (HFOs) are developed as alternative refrigerants in order to replace the progressively forbidden ones [52, 53]. They are synthetic fluids containing a double carbon bond. Figure I.4 [52] summarizes the most important HFOs and HCFOs molecules.
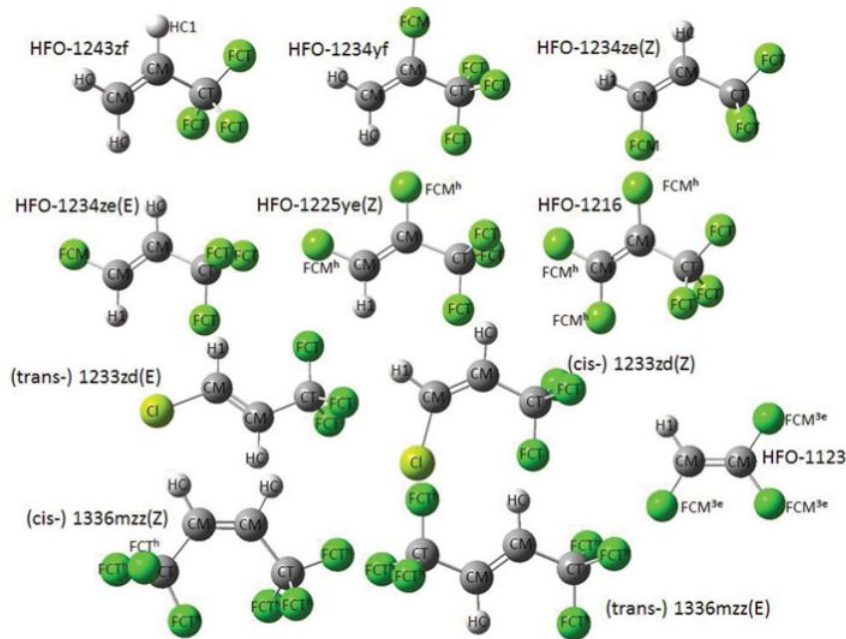
Figure I.4: HFOs and HCFOs family [52].

Their double carbons bond ensures a low atmospheric lifetime providing a low GWP. Besides, pure HFO molecules are not composed of chlorine atoms, and have thus a zero ODP. As shown in Table I.1, the HCFO molecule is the only one of this new generation composed of one chlorine atom and therefore has a finite, but very low ODP. They could therefore replace HFC and HCFC molecules in industrial systems [52]. This provides a new outlook to limit the environmental impact related to the worldwide increasing use of refrigerants.

	Chemical Name	Generation	Atmospheric lifetime	GWP100yr	ODP
CFC-11	trichlorofluoromethane	second	52 years	5160	1.00
HCFC-123	2,2-dichloro-1,1,1-trifluoroethane	third	1.3 years	79	0.02
HFC-134a	1,1,1,2-tetrafluoroethane	third	14 years	1360	0
HFO-1234yf	2,3,3,3-tetra-fluoro-1-propene	fourth	10.5 days	4	0
HCFO-1233zd(E)	trans-1-chloro-3,3,3-trifluoropropene	fourth	26 days	7	0.00034

Table I.1: Evolution of the atmospheric lifetime, GWP over 100 years and ODP over the different generations of refrigerants. Values found in [50, 54, 55, 56, 57, 58].

These new refrigerants have to replace the old ones in systems such as Mobile Air Conditioning (MAC) systems, Organic Rankine Cycle (ORC) and chillers.

The most widely used refrigerant for MAC systems of automobiles is the HFC-134a with a GWP of 1360 [50]. Leakage of HFC-134a from the air-conditioning system increases its presence in the atmosphere and the effect on the global warming becomes consequent due to its high GWP. Leakage can be reduced by improving components design. Alternatively, refrigerants with lower GWP can be used. For instance, the 2,3,3,3-tetrafluoropropene (HFO-1234yf) refrigerant is considered as replacement of HFC-134a in MAC systems, for having compatible thermo-physical properties and lower GWP [59, 60, 53]. Both HFO-1234yf and HFO-1234ze(E) show lower coefficient of performance (COP) and cooling capacity than HFC-134a [61, 62, 63, 64]. Nonetheless the modification of the system itself can improve the performance of systems based on HFO-1234yf [65]. For instance, Molés et al. [66] found that using an expander or an ejector as expansion device increases the COP in comparison to basic cycle working with HFC-134a.

The Organic Rankine Cycle (ORC) is a thermodynamic system (mostly composed of the same components that the vapor-compression refrigeration system (see Figure I.1), used to create electricity from low temperature heat sources. This heat can come from different processes, such as biomass combustion, industrial waste heat, geothermal or solar heat [67, 68]. This heat is used to evaporate the working fluid. HFC-245fa is commonly used for ORC at low temperature. However, with its 1030 GWP, some new working fluids have to be found as replacement. Cis-1,1,1,4,4,4-hexafluoro-2-butene, also named HCFO-1336mzz(Z) and trans-1-chloro-3,3,3-trifluoropropene, or HCFO-1233zd(E), are investigated as alternatives to HFC-245fa [69, 70] for ORC systems. Molés et al. [71] found that the use of HFO-1336mzz(Z) as the ORC working fluid gives a slightly higher system thermal efficiency. In supercritical ORC, HFO-1234ze(E) could also replace HFC-134a [72, 73]. Mota-Babiloni et al. [74] proposed system modifications to increase HFO-1234ze(E) cooling capacity and compared it with features obtaind with R134a.

Concerning the low pressure centrifugal chillers used to cool down huge buildings, HCFO-1233zd is envisaged to replace the HCFC-123 refrigerant [31, 75, 76].

The regulations have also reintroduced interests about "natural refrigerants" (for instance: NH_3, CO_2, H_2O, hydrocarbons, air) of the first generation[77, 78]. CO_2 is for example easily available and cheap but need a high operating pressure compared with other refrigerants. Therefore, the cost of refrigeration systems enabling high pressures is one of the main issues to address [43]. However, CO_2 refrigerant properties make it one of the promising HFC replacements in some systems [79]. Hydrocarbons (HCs) have also been proposed as alternatives for domestic refrigeration to replace R-134a [80, 81]. However, due to their flammability, restriction have been applied [82].

As mentioned above, refrigerants have various ranges of application pressure, depending on their boiling point. In order to replace an old refrigerant with a new, more envi-

ronmentally friendly one, the user has to verify the range of pressures that the new refrigerant can sustain.

Forced by scientific discovers about environmental aspects, this fourth generation of refrigerants opens a new hope in refrigeration industry. These zero ODP and very low GWP molecules could answer to regulatory requirements. However, Vollmer et al. [83] published first observations of the presence of medium pressure refrigerants HFO-1234yf and HFO-1234ze(E) and low pressure refrigerant HCFO-1233zd(E) in atmosphere, showing that even with their short atmospheric lifetime, the emission growth of the fourth generation of refrigerant remains detectable. These three new refrigerants are the most promising ones [2].

However, new HFOs such as HFO-1234yf and HFO-1234ze(E) are flammable and have lower volumetric refrigerant capacities than the old HFCs [52, 84]. This latter feature is defined as the cooling capacity per unit of vapor volume at the exit of the evaporator. In order to increase the cooling capacity and to suppress flammability, HFC refrigerants can be used in HFO/HFC compounds. In some cases, HFC added to HFO can even increase the COP in comparison with pure HFO [85, 73]. Nonetheless the high GWP values of HFC have to be considered to design the HFO/HFC blends due to the new regulations regarding to GWP levels. Moreover, CO_2 is non-flammable and has a GWP of 1. Therefore it is a good candidate for blending with HFO compounds [86].

These issues regarding flammable behavior of some HFOs are suppressed by considering HCFO-1233zd, making it especially interesting.

I.2.3   HCFO-1233zd(E)

The trans-1-chloro-3,3,3-trifluoropropene 1233zd(E), also called HCFO-1233zd(E) or R-1233zd or even R1233zd, belongs to the fourth generation of refrigerants. It is a hydrochlorofluoroolefin (HCFO) because the molecule contains a chlorine atom. Its applications are presented and then, a literature review on its physical and environmental properties is performed.

Note that for more clarity, the HCFO-1233zd(E) refrigerant will be named R1233zd in the following sections and chapters. More generally, every refrigerant molecules will be named that way. HFC-134a will be called R134a and HCFC-123 named R123.

Because of its relatively high boiling point, R1233zd is considered as an alternative refrigerant to replace e.g. R245fa for ORC and for high temperature heat pumps, or R123 for low pressure centrifugal chillers [31, 75, 76, 87]. In fact the U.S. Environmental Protection Agency approved the use of R1233zd for chiller applications. In 2014 the Trane

inc. manufacturer commercialized the first chiller in the world using this refrigerant [88]. R1233zd is also proposed as spray foam for building roof insulation [58].

Eyerer et al. [89] concluded that R1233zd can be used as a substitute for R245fa in existing ORC systems, leading to an increasing thermal efficiency. They found that R1233zd performs 6.92% better than R245fa for the highest achieved thermal efficiency. However, R245fa performed 12.17% better regarding the maximal gross power output. Molés et al. [69] found from the theory that the use of R1233zd as the ORC working fluid for low temperature heat recovery could increase by up to 10.6% the net cycle efficiency as compared to using R245fa. Nonetheless, in a following paper [90], they found from experiments a mass flow rate 20% lower for R1233zd than for R245fa, leading to a reduced thermal efficiency. For geothermal powerplants based on ORC, Welzl et al. [91] found that R245fa performs better than R1233zd. Lavernia et al. [92] found a theoretical thermal efficiency of 14.79% with ORC system using the R1233zd working fluid in residential applications. Guillaume et al. [93] considered small scale ORC systems used to convert the waste heat coming from the exhaust gases of a truck combustion engine. In this study, the bearings are lubricated with the refrigerant itself. They experimentally found that R1233zd represents a better choice than R245fa in this kind of application. Furthermore, Ju et al. [94] found different R1233zd/hydrocarbons blends to replace R22 or R134a in heat pump water heaters. Of course, these results have to be considered carefully because they depend on what system is considered and each ORC system manufacturer can have used different processes, materials or components design.

Whereas several studies are conducted to replace R245fa with R1233zd for ORC systems, only very few papers relate to the replacement of R123 by R1233zd for low pressure centrifugal chiller [3, 2]. In comparison with some others refrigerants, such as R1234yf, the literature is still poor regarding R1233zd.

We now turn to the environmental and physical properties of this new refrigerant. Because of the chlorine atom of the R1233zd molecule, it is classified as HCFO and not HFO. However, due to its short atmospheric lifetime of around 26 days [56, 58] caused by the double carbon bond, R1233zd still has a low ODP of 0.0005 [95, 96]. Patten el al. [57] also found a close ODP value of 0.00034. Note, however, that Orkins et al. [95] proposed a larger atmospheric lifetime value of 46 days and besides, they pointed out that the lifetime can be drastically increased with the latitude of the emission and the season. Sulbaek Andersen et al. [56, 97] studied the reactions in the atmosphere with R1233zd. They discovered that OH radicals react with the refrigerant through the two carbons of the double bond. Thanks to these results, they calculated the atmospheric lifetime of 26 days, depending on the OH concentration in atmosphere. In any case, this lifetime is much lower than the ones of R134a and R245fa, respectively of 51 and 7.4

years [98]. Moreover, R1233zd has a GWP upper limit of 14 for time horizons of 100 years [95]. The literature often makes reference to a GWP value of 7 for a 100-year time horizon, given by Sulbaek Andersen et al. [56]. Unlike some other HFO refrigerants and even with a small ratio of chlorine to hydrogen atoms amount, R1233zd remains non-flammable. Since it has a bowling point T_b of 291.2 K at ambient pressure [99], experiments are difficult with R1233zd, due to the evaporation.
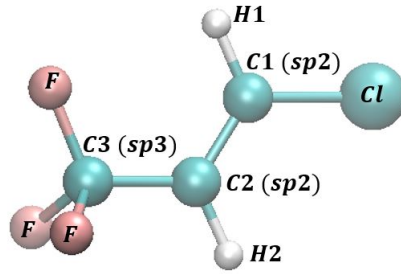
Figure I.5: Representation of the trans-1-chloro-3,3,3-trifluoropropene 1233zd(E) molecule. Caption obtained with the VMD software [19]

As represented in Figure I.5, the R1233zd molecule is composed of a CF_3 group next to a double-carbon bond. The sp^2 carbon in the middle is linked to a hydrogen named H2 and the second sp^2 carbon to one hydrogen H1 and one Cl atom.

A density value ρ of 1.276 g/cm^3 and a viscosity value η of 0.506 mPa.s at 19°C and 150 kPa are experimentaly found by Honeywell [100]. A small amount of experimental works have been performed by different research groups but most of them present thermophysical properties at low pressure only. Vapor pressure studies have been published [99, 101, 100], as well as speed of sound data [101] and surface tension [100, 102]. Moreover, liquid and vapor density data sets have also been published [103, 104, 100], but with low values of pressure. For instance, Fedele et al. [103] reached a saturation pressure of 35 MPa while Romeo et al. [104] stopped at 30 MPa. Therefore, these results cannot be directly used in studies of lubricated contacts. Furthermore, Perkins et al. [105] experimentally measured the thermal conductivity of R1233zd at pressures up to 67 MPa. Data sets of pressure-density-temperature (P,ρ,T) [101, 106] and pressure-specific_volume-temperature (P,v,T) [103] have been published as well.

One key issue in the literature on R1233zd is that no data is available for high pressure studies, except the one published by Morales-Espejel et al. [3] and a review of rolling bearing technology for refrigerant compressors [2].

In this project, only chiller systems composed of centrifugal compressors and employed to cool down large buildings or industrial process are considered. Indeed, it will be explained in the next section that systems used in mobile air conditioning systems for example cannot be treated with the same conditions (regarding local pressure, shearing velocity, refrigerant that can be used) in comparison with systems implemented in huge

buildings.

I.3 Lubrication in refrigeration systems

After introducing the main features of refrigerants in general refrigeration systems, this section aims to develop the lubrication principles in the contact area within the compressor systems.

I.3.1 Lubrication

The science of lubrication consists in introducing a lubricant between two surfaces moving one with respect to the other in order to reduce friction and wear. By reducing the tangential stress between moving elements, the life of mechanical components is improved. In centrifugal compressors, the rotation is ensured by rolling elements bearings.

Rolling element bearings are composed of two rings separated by rolling elements (balls, rollers, etc.), which are held within cages. In most applications, one of the rings is fixed to the housing and the other one to a shaft. The rolling bearings sustain loads and reduce friction in rotating mechanisms. Their lubrication ensures surface separation, load transmission, speed accommodation, cooling-down of the contacting solids and debris removal [107, 108]. The lubricant is usually oil or grease according to applications, environment and operating conditions. In some cases, it can be the working fluid (refrigerants in refrigeration systems, fuel in engines).

The surface separation is characterized with the thickness of the lubricant film, usually denoted h. This contact caracteristic has to be compared to the surfaces roughness in order to define the lubrication regime.

In the full film regime, the normal load is entirely supported by the hydrodynamic lift. The lubricant film is thick enough to ensure a full separation of the surfaces. The full film regime can be divided into two sub-regimes: hydrodynamic lubrication (HL) and the elasto-hydrodynamic lubrication (EHL) regimes.

Hydrodynamic lubrication often involves conforming surfaces, for example within journal bearings. Indeed, the lubrication and load occur in a large ($\sim$ cm^2-dm^2) contact area and thus, the lubricant pressure is in the range of 0.1-10 MPa [109]. These small pressure values yield to negligible elastic deformation of surfaces.

The second sub-regime is named Elasto-Hydrodynamic Lubrication (EHL) and concerns non-conforming geometries, like ball-on-plane contacts. The small contact area ($\sim$ mm^2) generates a high local pressure (0.5-5 GPa), leading to non negligible elastic deformation

of surfaces, hence the "elasto" term in EHL. The high pressure induces a change of lubricant properties through viscosity-pressure and viscosity-temperature dependence, and compressibility.

The mixed lubrication regime appears at smaller film thickness. In this regime, the surfaces are not fully separated by the lubricant and the asperities can come in contact, supporting a fraction of the load.

In the boundary lubrication regime, the load is fully carried out by direct contact between asperities. Additives can be used to protect the surface from direct asperities contact [110, 28, 27]. An adsorbed layer of lubricant additives can protect the surface from wear issues thanks to chemi- or physisorption phenomena.

Classical lubricants such as oils or greases in rolling element bearing complicate the design of refrigerant systems, since it involves an additional fluid to the working fluid (the refrigerant). Moreover, the refrigerant can mix with the lubricant fluid.

I.3.2 Refrigerants as lubricants

In this section, two possibilities of lubricating rolling bearing in refrigeration compressors are presented. The first one, which is currently the most available, is lubricating the bearing with an oil-refrigerant mixture. The origins of this mixture and the issues encountered with refrigerant in the lubricated contact will be detailed. Then, systems lubricated with pure refrigerants will be presented and the advantages of this solution will also be explained.

I.3.2.1 The unavoidable mixing of oil and refrigerant in lubricated systems

The conventional chiller design is represented in Figure I.6 [4].

The oil cycle and refrigerant cycle are theoretically separated with sealing. However, an impeccable sealing remains hard to design. The oil used to lubricate the compressor can be discharged into the refrigeration cycle and decreases heat transfer efficiency around the heat exchanger [111, 112, 3]. On the other side, rolling bearings in compressors are usually lubricated with an oil-refrigerant mixture. The dilution of refrigerant in oil reduces not only the viscosity but the viscosity-pressure dependence as well, and thus impacts the ability to build a separating film in the lubricated contact[113, 114, 60, 115, 116, 117, 118, 119, 120, 121, 122, 120].

Indeed, in lubricated contacts, the film thickness depends mainly on two lubricant properties: the viscosity and the viscosity-pressure coefficient. The viscosity η varies with
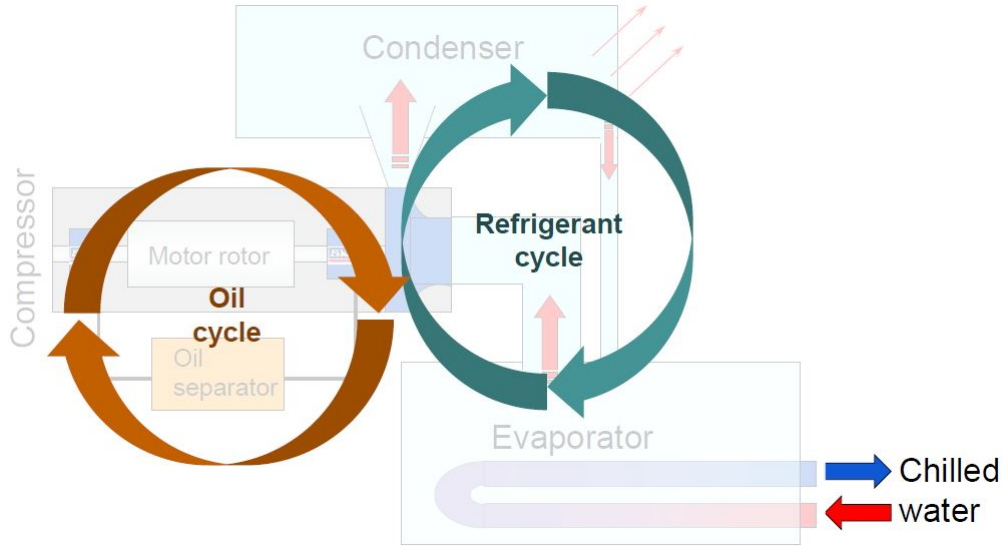
Figure I.6: Conventional chiller design [4].

pressure and temperature but depends also on the shear rate. At low shear rate, viscosity does not depend on the shear rate (Newtonian behavior), but at high shear rate the viscosity can decrease with increasing shear rate (shear-thinning) [24].

The viscosity-pressure coefficient α describes the influence of the pressure on viscosity. This variation can be determined with the Barus relation [123], as follows.

$$\eta(P,T) = \eta(0,T)e^{\alpha(P,T)P} \tag{I.1}$$

In this definition α varies with the pressure, limiting its applicability. Therefore Hamrock and Dowson [124] used the reciprocal asymptotic isoviscous pressure coefficient α^* [125] of Equation I.2 for film thickness prediction, where η_0 is the Newtonian viscosity and the pressure is expressed in MPa.

$$\frac{1}{\alpha^*} = \int_{0.1}^{\infty} \frac{\eta_0(0.1,T)}{\eta_0(P,T)} dP \tag{I.2}$$

The mixture of oil and refrigerant has been widely investigated regarding either lubricating properties, or thermophysical and rheological features. All the properties of the oil/refrigerant mixtures depend on the type of molecules considered. Indeed, Polyol Ester (POE), which is commonly used as refrigeration compressor oil [126], can react with R134a in a different manner than a mineral oil or a Polyalkylene Glycol (PAG). This is why main principles are developed in this section, but for clarity, the names of oils and refrigerants will not be provided.

To assess the lubrication ability of an oil/refrigerant mixture, the miscibility of the refrigerant in the oil lubricant is of primary importance [127, 128, 122, 20, 129, 21, 130,

121, 131]. The dissolution rate depends on the refrigerants and has to be determined to predict the film thickness [20, 129]. In particular, the difference in refrigerant molecular polarity can affect the dissolution in oil and thus the simple replacement of an old refrigerant with a new one is not automatically possible [2]. A more branched lubricant is more affected by dilution of refrigerant than a linear fluid [132, 133].

Adding only 9% by weight of refrigerant in an oil can decrease the film thickness to half its value, and the viscosity-pressure coefficient can be divided by two by adding 35% by weight of refrigerant [134]. The variation of the compressibility of the oil/refrigerant mixture with the quantity of refrigerant is still unclear. Some research groups found an increase of the compressibility with the amount of refrigerant [135] while other groups found the opposite [126].

Thanks to micro Fourier Transform Infrared (FT-IR) spectroscopy, it was found that the concentration distribution of the refrigerant in an EHD contact decreases in the inlet zone and in the Hertzian contact area. However, the refrigerant concentration increases in the side region of the contact [136]. Moreover, the concentration distribution of the refrigerant is affected by the sliding velocity and the temperature. Bair et al. [113] also found that increasing the inlet pressure reduces the film thickness due to an increasing solubility of the refrigerant in oil. However, they revealed an unusual behavior, when they pointed out that the inlet temperature can either reduce or increase the film thickness. On the one hand, by increasing the temperature the viscosity decreases and this tends to reduce the film thickness. But on the other hand, increasing the temperature reduces the concentration of refrigerant and thus leads to increase the mixture viscosity. There is a competition between these two effects. For low inlet pressure, the first effect is dominant while the second one appears more likely at high pressure.

Since oil/refrigerant mixtures have been widely studied in the literature, it is not the aim here to make a complete review but to show the research directions regarding these blends in lubricated contacts. One of the key results is that a dilution rate of refrigerant in oil limit of 20% to 30% has been found to lubricate a conventional all-steel bearings [2, 137].

Furthermore, the development of new viscometers operating at high pressure for oil/refrigerant mixtures opens the possibility to obtain accurately the viscosity, which is used in numerical models to predict the film thickness in EHL [138]. Recently, Bair [138] published results of the decrease in viscosity and viscosity-pressure coefficient for a POE/R134a mixture depending on the weight percentage of R134a in the blend. Some of these results are presented in Figure I.7, showing a considerable reduction of the viscosity and of the viscosity-pressure dependence with increasing weight percentage of R134a.

Besides, the high flow velocity might involve a non-equilibrium state of the solution. Depending on the surface temperature and on the oil-refrigerant mixture boiling point,
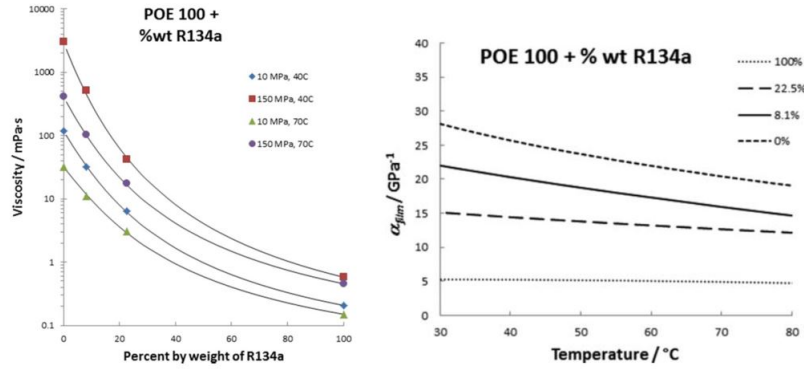
Figure I.7: Variation of the viscosity as a function of the weight percent of R134a in the mixture, at fixed temperatures and pressures (left). Viscosity-pressure dependence as a function of the temperature, at fixed weight percent of R134a in the mixture (right) [138].

the refrigerant can condense or boil off on the surface. This instability influences the ability to obtain a sufficient film thickness [139].

In addition to these problems of film build-up due to the oil-refrigerant mixture, two kinds of defects also appear on the surfaces because of the refrigerant in the lubricated contact. They are detailed in the following section.

I.3.2.2 Two issues encountered by lubricating with refrigerants: surface distress and corrosion

In refrigerant compressor bearings, due to pressures usually lower than 2 GPa, the main problems are rather related to the surface than to the subsurface. Indeed micropitting, also named surface distress, and wear can appear because of poor lubrication and contamination [2].

Surface distress comes from poor lubrication, related to low viscosity and viscosity-pressure dependence of the mixture, and high compressibility. Surface distress is a competition between mild-wear and surface fatigue [2]. An example of surface distress obtained in a raceway bearing surface in given in Figure I.8.

Corrosion fatigue is the second kind of defect observed for rolling bearing in refrigeration compressors. It comes from chemical reactivity of the refrigerants and can also be due to moisture. The corrosion effect can sometimes be increased with the latest generation of refrigerants. Indeed, as said before, the new HFOs and HCFOs have shorter lifetime than previous refrigerants, due to their larger chemical reactivity. The refrigerants can corrode steel surfaces, but also the cage and seals, and even ceramic materials [2]. Besides, the moisture inside the bearing can also be increased due to temperature changes of some components of compressor, raising corrosion effects. When the corrosion is significant, corrosion pitting can appear.
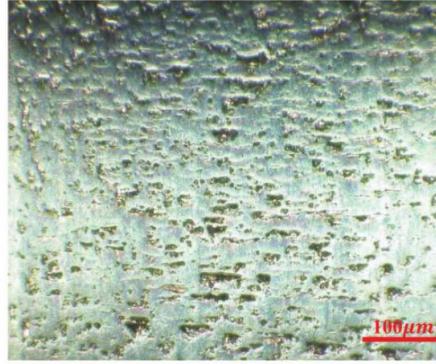
Figure I.8: Surface distress in a raceway bearing surface [2].

The efforts made in industry to enhance the bearings life are principally focused on protecting the surface from micropitting. The analytical model developed by Morales-Espejel et al. [140] can be used for micropitting in rolling bearings lubricated with oil-refrigerant mixtures [2].

To counter all the problems found in oil-refrigerant lubricated systems, the idea to lubricate the rolling bearings without any oil, thus only with the refrigerant, has attracted a growing interest. Besides, to reduce the corrosion and surface distress, special rolling bearings can be used, as detailed in the next section.

I.3.2.3 An alternative: pure refrigerant lubricated (PRL) systems with special hybrid rolling bearings

Traditionally, compressors are composed of hydrodynamic bearings, using a large amount of lubricating oil. With rolling bearings, less oil flow is required and a lower friction is observed, increasing the energy efficiency (around 2-4% [141]) in comparison with hydrodynamic bearings [1]. For centrifugal compressor, oil-free lubrication is possible by using either magnetic bearings or hybrid bearings (as detailed below) lubricated with pure refrigerant. The latter is named pure refrigerant lubrication (PRL), and this project focuses in this technology. Unlike screw compressors [2], centrifugal compressor used in large chiller can be designed with PRL, as shown in Figure I.9.

Oil-free systems improve heat transfer in the refrigation cycle, because no oil is discharged in the cycle anymore. The cost is reduced thanks to less maintenance and to cutting oil costs. Furthermore, the number of components are reduced, which also decreases the chiller cost [141].

Jacobson and Morales-Espejel [139] provided in 2006 analytical expressions of the compressibility as a function of the pressure for three refrigerants, R123, R134a and R245fa. Recently, Bair et Laesecke [142] measured the viscosity of pure refrigerants R32 and R410A at high pressure (350 MPa) in order to predict film thickness values. Moreover,
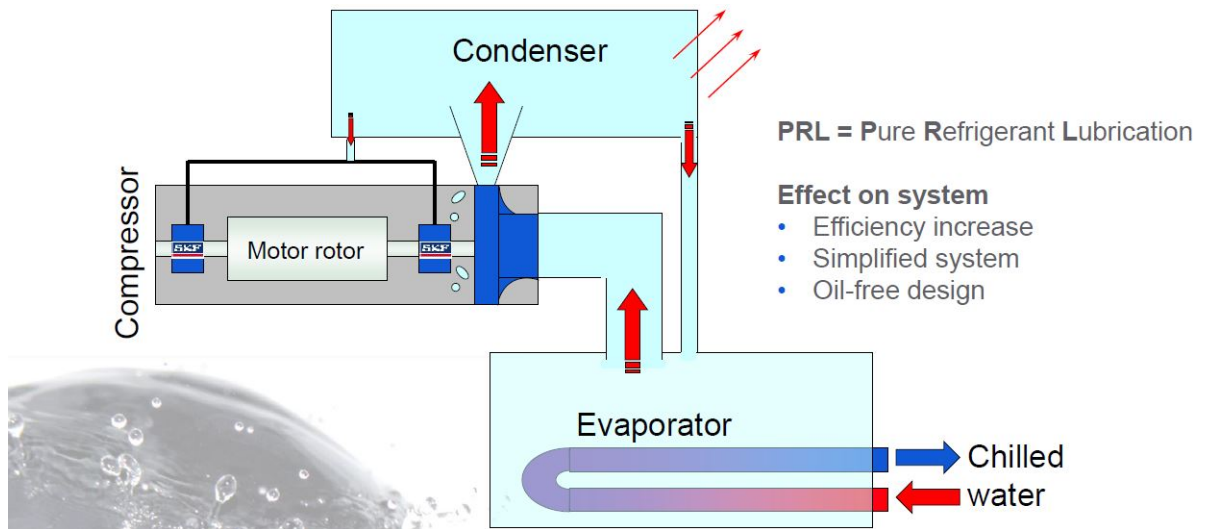
Figure I.9: Pure Refrigerant Lubricated chiller design [4].

it was found that it is possible to form a separating film because of an increase of viscosity with the very high pressure located in the contact between the rolling elements and the bearing raceways. This increase is not as large as with classic oils but sufficient to build a very thin lubricant film [1]. With conventional all-steel bearings, it would be inadequate for lubrication but the SKF compagny developed special hybrid bearings (as detailed below) enabling a PRL technology [1].

PRL rolling bearings require special materials. Special hybrid rolling bearing in PRL technology are composed of silicone nitride Si_3N_4 rolling elements, and cages made of glass fiber-reinforced PEEK material. The inner and outer rings are made of stainless high nitrogen through-hardened steel, heat-treated. This steel has very good anti-corrosion features, and super fine microstructure, making it suitable for this poor lubrication case [1, 2, 143]. The same composition could also be found for hybrid roller bearings. Moreover, hybrid contacts are less prone to micro-welding of asperities. In the case of PRL, corrosion can appear with hybrid bearings [2]. Therefore, additives could be added to prevent the risk of chemical reactions between the refrigerant and the surfaces. However, the ring surfaces are greatly protected against corrosion by using stainless high nitrogen through-hardened steel [3].

In poor lubrication conditions, hybrid bearings show advantages in comparison with all-steel bearings. A lower friction is obtained and the materials do not weld at high temperatures, contrary to steel-steel contacts [1]. Besides, for all-steel bearings, coatings could be applied on steel surfaces, but it was observed that the refrigerant could penetrate the coating through the pores and by reaching the steel surface, it can corrode the surface below the coating [2].

Next section focuses on the regime occurring with refrigerant lubricated systems.

33

I.3.3 A very thin film lubrication regime in refrigeration compressors with PRL

This project is mainly based on experimental observations and numerical analysis made by Morales-Espejel et al. [3] in 2015 on R1233zd, and by Vergne et al. a few months later on R123 [144]. Both papers have reported interesting results about lubricating contacts with pure refrigerants.

In the following, friction is quantified with the (solid) friction coefficient (Cf), that was introduced by Da Vinci [145] as the ratio between the force resisting the tangential motion of two solids in contact and the normal load.

Morales-Espejel et al. [3] investigated experimentally and theoretically the ability to form a lubricating film with R1233zd. They measured the film thickness using interferometry in a tribometer. To avoid evaporation due to a boiling point of R123zd around 19°C, the interior of the box where the measure is perfomed is cooled down with cold nitrogen gas in order to keep the temperature at 10°C. The authors increased the entrainment speed from 0.001 to 2 m/s and observed an increasing film thickness with a maximum value of around 15 nm, which is, given to the roughness of the ball and disc, close to a full-film regime. Then, surprisingly, by decreasing the entrainment speed, a higher film thickness value was measured. Indeed, a solid layer was formed on the steel ball. The authors assumed that chemical reactions or tribochemical processes could occur at the interface between the refrigerant and the surface. The authors found a very low friction coefficient of around 0.072, in comparison with steel-steel contacts and typical oils, where a value up to 0.15 can be reached [1]. Indeed, low friction coefficient is usually found when using hybrid rolling bearings [146] and it was also assumed that tribochemistry effect leading to the aforementioned solid layer could play a role.
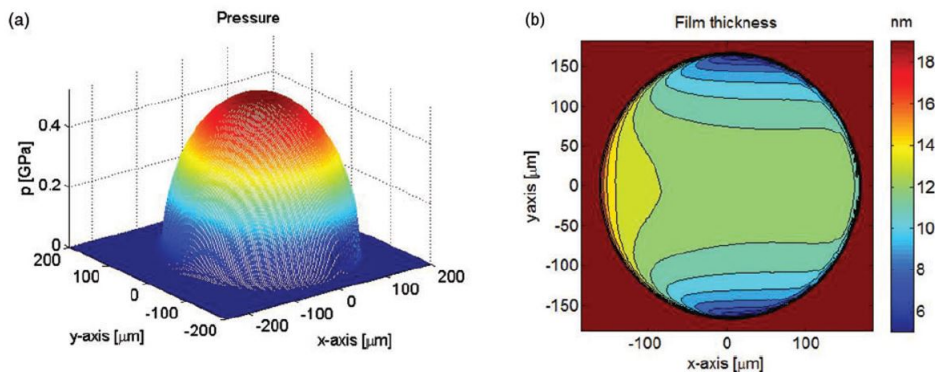
Figure I.10: Example of pressures and film thickness results obtained numerically with an entrainment speed of 2 m/s and a maximum Herzian pressure of 0.5 GPa [3].

Figure I.10 [3] shows pressure profile and film thickness values obtained from simulations with a model describing the R1233zd refrigerant. A minimal film thickness value was

obtained in the side lobes of the contacts. The reduction of thickness at the contact exit is less apparent than usually in EHD contacts with oils: these observations were explained with respect to the small viscosity and viscosity-pressure coefficient of the refrigerant.

Most published data for R1233zd are at saturation pressure, which is much lower than contact pressure. Therefore Morales-Espejel et al. used data furnished by the manufacturer Honeywell in their study [147, 3]. To the knowledge of the author, there is no data available in the literature for the viscosity-pressure coefficient of R1233zd. Since it plays a crucial role in the prediction of the film thickness in EHL, Morales-Espejel et al. used a value published for a similar low-pressure refrigerant $\alpha^* = 4.36\,\mathrm{GPa}^{-1}$, corresponding to the refrigerant fluid A in the paper of Habchi et al. [148]. These values of the viscosity-pressure coefficient and viscosity should also be compared with the ones found in literature for two other refrigerants. Vergne et al. [144] give an α^* value of $6.4\,\mathrm{GPa}^{-1}$ and a viscosity $\eta_0 = 0.4\,\mathrm{mPa.s}$ for R123 at 25°C, while Bair [138] reported a value of $5.0\,\mathrm{GPa}^{-1}$ and Laesecke and Bair [149] gave a viscosity $\eta_0 = 0.2\,\mathrm{mPa.s}$ at 40°C, both values for R134a. These small values of viscosity-pressure coefficients for the refrigerants do not favor the build-up of the film thickness. Indeed, it is interesting to compare these values with classical oil values, which have a viscosity η_0 of around 20 mPa.s and an α^* of around $20.0\,\mathrm{GPa}^{-1}$ [2].

The same observations made with pure R1233zd about the film thickness distribution, were observed with pure R123 [144]. In Figure I.11, the minimal film thickness value obtained from experimental, numerical and analytical analysis is drawn. The entrainement velocity u_e in Figure I.11 is the mean velocity of the two surfaces.
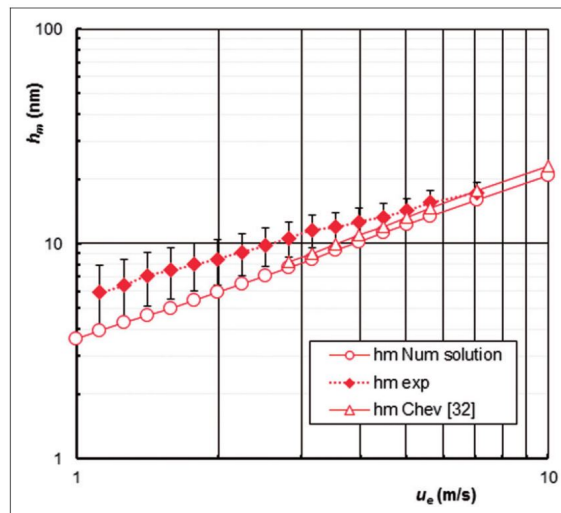
Figure I.11: Numerical solution for the minimum film thickness compared with the experimental results and the Chevalier [150] prediction (T=10°C, SRR=0 and p=0.52GPa) with pure R123 [144].

These values found for the minimal thickness are small. However it still corresponds to

20 to 30 R123 molecule sizes. Furthermore, these order of magnitude for the thickness values are the same than the ones observed by Morales-Espejel et al. with R1233zd [3]. They also carried out density calculations as a function of pressure because the more compressible the refrigerant, the thinner central film thickness will be. Also here, no damage was observed on the surface and a possible explanation was made about a minimal film thickness localized in very restricted area. Vergne et al. [144] concluded that the R123 refrigerant can indeed build up a reasonable film thickness for lubricating rolling point contacts.

After polishing, the roughness maximum value σ of the surfaces was about 5 nm. The authors considered the λ parameter, defined as follows, with h_m the minimal thickness:

$$\lambda = \frac{h_m}{\sigma} \tag{I.3}$$

It is usually accepted that the full film EHL regime is reached for a λ value higher than 3. This value was obtained for an entrainment velocity u_e higher than 5 m/s. It means that a limit is reached for u_e lower than this value and the lubrication occurs in a mixed regime. Nonetheless, as no damage was observed on the surfaces, it could be considered that the lubrication appears between a full EHL regime and a mixed regime. This "in-between" regime is sometimes named "very thin film" (VTF) regime [144].

These two studies guided the direction of this project in order to explore the effects of this very small minimal film thickness, corresponding to a molecular lubrication. The main result here is the presence of a solid layer on the steel ball surface when lubricating with R1233zd and that no damage was observed on this surface.

As a conclusion of this section, in comparison with common lubricants (oils), refrigerants show both a very low viscosity and a low viscosity-pressure dependence. A refrigerant used as a lubricant can cause a lower ability to lubricate in the so-called full film lubrication regime, where solid surfaces are fully separated by the lubricant. At the same time, this smaller viscosity induces a poor load bearing capacity. As a consequence, pure refrigerant-lubricated contacts often work in a VTF lubrication regime.

I.4 Molecular scale investigation

Combined to very thin film of refrigerants, progresses in surface manufacturing enable to design really smooth steel surfaces with a root mean square (RMS) of around 5 nm [144], which favor molecular lubrication [151]. In this section, experimental and numerical investigation methods for molecular lubrication are presented. An overview of the features of the nanoconfined lubricant behavior is reported. Finally, a focus

on adsorbed layers of lubricant will be discussed with examples concerning the new refrigerants.

I.4.1   Investigation methods to study molecular lubrication

I.4.1.1   Experimental tools

In 1961 [152], the fabrication of the Surface Force Apparatus (SFA) enabled observations of a molecularly-thin film located between two perpendicular cylinders brought in contact. The position of the cylinders is driven thanks to piezoelectric elements with a precision of tipically 0.1 nm. Optical interferometry or capacitive methods [153] are used to measure the distance between the surfaces.

In 1981 [154], the scanning tunneling microscope (STM) was invented. A STM is an instrument for imaging surfaces, as well as lubricant molecules, using the quantum tunneling of electrons between a conducting tip and the surface/object under investigation. The tip is approached to the surface and a difference of electric potential is applied between the tip and the surface. When the tip is moved across the surface, the tunneling current is measured. Thanks to a control system, this current is kept constant by adjusting the surface height, which is mapped in order to represent the surface.

The Atomic Force Microscope (AFM), invented in 1985 [155], can characterize interactions at the molecular scale. The AFM is composed of a cantilever with a nanometer scale tip at its end. The tip is moved above the surface or in direct contact, and the force between the tip and the surface leads to a deflection of the cantilever. This deflection is measured for example with a laser beam. This allows force measurement, imaging and atoms manipulation. Thanks to AFM, forces can be measured directly on the surface, or on an adsorbed fluid layer, providing information on wear. Modification of AFM for applications in tribology led to the Friction Force Microscope (FFM) that can measure tangential forces.

The maybe most interesting instrument for this project uses the X-Ray photoelectron spectrometry (XPS) method [156]. The first commercial XPS was built in the late 1960s. The material is irradiated with a X-ray beam while kinetic energy and number of electrons that are ejected, are measured. From the collected data, one can evaluate the sample chemical composition of the topmost few nm. Moreover, by using abacus, the results are compared to the reference and one can determine information about local chemical bonding and in particular about chemisorption. This last point is for instance a key point to study the chemical composition of adsorbed layers.

By using different experimental tools, one can determine the chemical composition and the topographical behavior of an adsorbed layer, as well as the frictional behavior of a

system under shear. However, it remains difficult to get information about the adsorbed layer formation during the frictional process. Therefore, numerical approaches have to be considered.

I.4.1.2 Numerical simulations

At the same time, the improvement of computers performance gives the possibility to study molecular lubrication thanks to different atomistic simulations tools. In this subsection, a listing of the mostly used atomistic and electronic methods is provided.

The monte-carlo (MC) is a method using a stochastic approach to determine the equilibrium properties and configuration of molecular systems in defined thermodynamic ensembles [157]. Atomic configurations are randomly generated and are kept only if they verify a condition depending on their energy states. Since time is not considered in this approach, non-equilibrium behavior related to fluid flow in nanoconfined system cannot be studied. If time-dependent features are needed, molecular dynamics simulations are preferred.

Molecular dynamics (MD) simulation is a deterministic method [23]. The evolution of a system of atoms can be simulated along time and the trajectory of particles is calculated numerically by solving Newton's equations of motion. For each timestep, the forces acting on every atoms are determined thanks to a force field describing interactions between atoms. Hence, a numerical integration of the subsequent accelerations gives the positions of atoms at the following step. Since MD simulations are time-dependent, non-equilibrium phenomena can be explored and a variety of features (friction, thermal conductivity, velocity profile, etc) can be obtained. Therefore MD simulations will be used in this project to characterize nanoconfined systems under shearing. A complete explanation of the MD model will be given in Chapter 3.

The tight-binding (TB) method uses the superposition of wave functions for isolated atoms to calculate the electronic band structure. Coupled with MD simulations, it has already shown ability to treat adsorption phenomena of fatty acids on iron surfaces [158] or to study wear phenomena between two surfaces [159, 160]. However this approach will not be presented in this work. Indeed, parameters describing interactions between orbitals within the solid, the refrigerant, and the interface, would have to be determined first.

Density functional theory (DFT) calculations can be used to analyze electronic structure of a static system [8]. This method can be used to obtain the density of state, the binding energy, the charges and the equilibrium geometry. Features of a many-electrons system can be studied thanks to functionals, which describe (in an approximate manner) electronic exchange and correlations. Some functionals have been recently improved in

order to treat van der Waals (vdW) forces [13]. These interactions are crucial to describe liquids and interfacial behavior. Therefore, this method will be used in this project to study interaction between the refrigerant and the surfaces, specifically to obtain accurate binding energies under different conformations of refrigerant molecules on surfaces. This method and all these enumerated possibilities will be detailed in Chapter 2.

Moreover, ab-initio molecular dynamics (AIMD) simulations can be considered to study molecular lubrication. The difference between standard MD and AIMD is that the interatomic forces are not calculated in the same way. However, with both methods, the trajectory of the atoms is calculated by solving Newton's equation of motion. In standard MD method, the force on each atom is calculated as a gradient of an interatomic potential, which is a function of the atomic coordinates corresponding to the atomic nuclei position. In AIMD, instead of using a force field, DFT is used to determine the interatomic forces derived from the energy, at a given time. Then, the nuclear position of the next step can be obtained and the DFT process is repeated with these new coordinates.

Figure I.12 [28] provides a representation of different scales available for simulations of tribological systems. Features can be determined with DFT from the electronic structure, while MD simulations can be used to study much larger systems with thousands of atoms. At even larger scale, continuum methods, such as finite element method (FEM) or finite volume method (FVM) can be used.
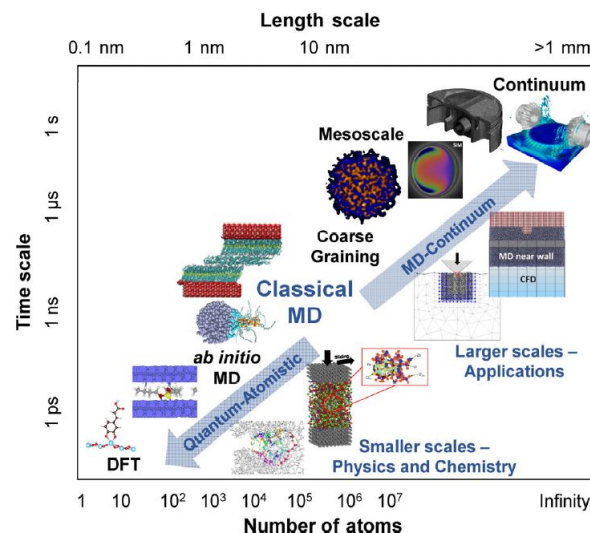
Figure I.12: Representation of different scales available for simulations of tribological systems, from quantum mechanical to continuum descriptions, linked to MD simulations. From Ewen et al. [28].

The choice of one of these methods often depends on what kind of system is considered. On the one hand, density functional theory (DFT) can represent matter at the quantum level, but its high computational costs precludes its use to consider a whole lubricated

contact area. DFT provides accurate adsorption information at the atomic level but is generally limited to static calculations. On the other hand, classical non-equilibrium molecular dynamics (NEMD) simulations, which are based on empirical force fields (FF), are widely used for large systems to characterize the rheology as well as the molecular structure of lubricants over reasonable timescales in some nanometric patch inside lubricated contacts [24, 161, 37, 27, 26]. Ab-initio molecular dynamics (AIMD) calculations become affordable on some systems [162, 110] but is still too demanding for other materials, e.g. those involving magnetism. Ewen et al. [27] used NEMD simulations in order to describe the behavior of stearic acid molecules adsorbed on a hematite surface while Doig et al. [163] considered the structures and friction of different fatty-acids adsorbed on iron-oxide surfaces. Ta et al. [10] used DFT calculations to parametrize a classical force field for the adsorption of n-alkanes on iron and iron oxide surfaces. Then, this force field was implemented into larger scale molecular dynamics simulations to study the tribological behavior of alkanes confined by iron and iron oxide surfaces under shear [26, 11]. Moreover, Vega et al. [164] and Lísal et al. [165] used MD simulations for some HFC and HCFC refrigerants in order to predict thermophysical properties. However, to the best of our knowledge, no numerical study of adsorption phenomena was achieved with any refrigerant. Besides, no MD simulations with confined refrigerants was found in the literature.

I.4.2 Structure and rheological properties of thin films

In this section, the main phenomena occurring in nanoconfined liquid, influencing frictional behavior, are described.

I.4.2.1 Structuration of lubricant at the interface

When the two solid surfaces approach, a particular structure of the fluid appears and the distribution of the lubricant molecules in the contact is influenced. Ordered structures were first observed with Monte Carlo simulations for Lennard-Jones liquids [166, 167]. In 1981, Surface Force Apparatus was used by Horn and Israelachvili [152] to study nanoconfined octamethylcyclotetrasiloxane (OMCTS). They showed that the force between two surfaces does not follow a smooth evolution with the distance between the two surfaces, as predicted by the Van der Waals theory, but oscillates between attractive and repulsive forces with a periodicity approximately equal to the molecular diameter. This phenomenon was called solvation force.

A particular arrangement of the molecules appears at the interfaces between the solids and the liquid. The molecules build a layered structure with distinct densities and the

highest one near the surface, as shown in Figure I.13. The first density peak near the surfaces can have a density of several times the bulk one.
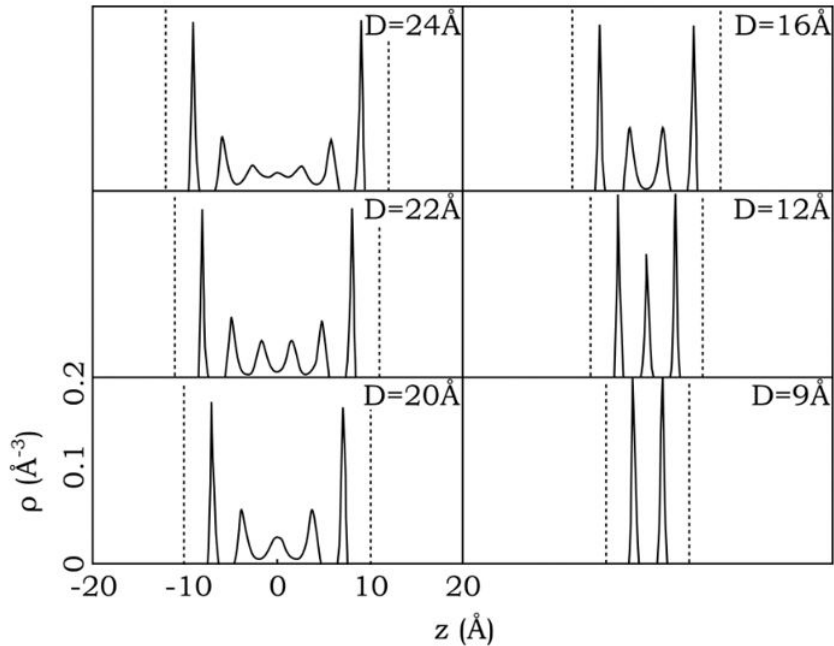
Figure I.13: Density profiles across the lubricant film (z-direction) for a confined Lennard-Jones fluid. The distance h between the walls (dotted lines) is varied from 24 to 9 Å, corresponding to 7 to 2 molecular layers. Results from Gao et al. [168].

This layering phenomenon comes from the solid/liquid interactions and can be influenced by the size and form of molecules and the smoothness of the surfaces. Indeed, nanometer scale roughness can preclude the formation of ordered layer structures [37, 169, 170, 171]. This structuration can be observed to a distance from the surface roughly equal to ten molecular diameters [172]. With ticker film thickness, the lubricant becomes isotropic and continuum mechanics apply. Furthermore, the high shearing and the temperature have no influence on this layering [173, 152, 174, 175] Besides, this layering can affect locally transport properties, like the viscosity [25, 176].

I.4.2.2   Interfacial flow: locking/slip effect

In continuum mechanics, a no-slip boundary condition is often assumed at the solid-liquid interface, implying that the lubricant flows at the same speed as the solid. However in molecularly thin film lubrication, two different phenomena can appear at the interface between the fluid and the solid affecting the flowing ability: locking and slip. The influence ensuing for lubrication properties is non-negligible, specially at small film thickness. A representation of these two phenomena is given in Figure I.14.

Locking appears when the interactions at the liquid/solid interface are strong [177]. Therefore, one or more layers of lubricant are locked on the surface, meaning that no
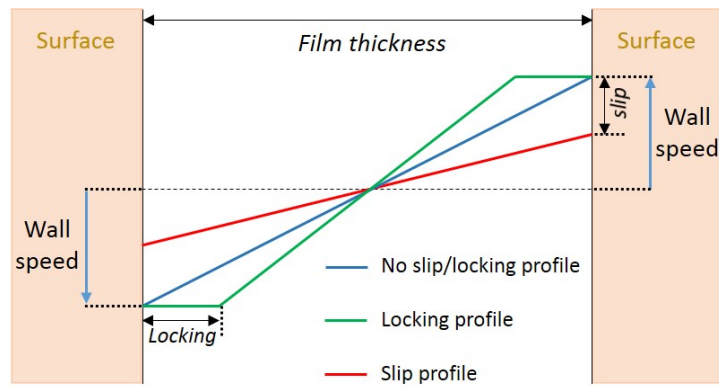
Figure I.14: Representation of locking/slip phenomena at the interface in a nanoconfined fluid under shearing.

relative tangential displacement occurs with the surface. These molecular layers stick to the surface and move with the same velocity than the one imposed on the wall. In this case, effective shearing will appear within a smaller thickness in the central part of the film. The interfacial flow can be modified by chemi- or physisorption of the lubricant itself or lubricant additives [178]. For instance, antiwear additives enable to increase the lubrication efficiency. The additives are chosen for their adsorption ability on the considered surface. Adsorbed layers can therefore be build up to protect the surfaces from wear and corrosion. It precludes direct contact between asperities, which would conduct to a higher friction and to damage the surfaces.

Wall slip can be considered as the opposite of locking effect. When the cohesion of the fluid is stronger than the liquid/solid interaction, a wall slip phenomenon appears at the interface, as shown in Figure I.15 on the left for both linear and branched decane confined between CuO surfaces [161]. As presented in Figure I.15, Berro showed with molecular dynamics simulations that the same fluid could be locked (on the right caption) or slip (on the left caption), as explained below, depending on the wettability of the surface [161].
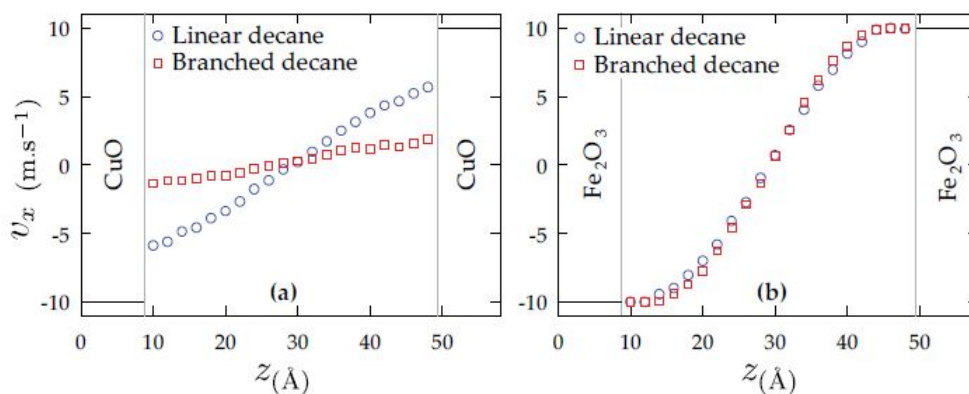
Figure I.15: Velocity profiles across a linear and branched decane films confined between CuO and Fe2O3 surfaces [161].

For both effects, two properties at the solid/liquid interface will define the fluid flow behavior: commensurability, which is linked to the geometry of the surface compared to the size of the fluid molecules [179, 37], and the corrugation [178] which describes the energy needed to initiate a relative tangential motion at the fluid/solid interface.

The influence of environmental parameters on the interfacial flow can be obtained with MD simulations. As an example, wall slip is increased with shear rate [180, 181]. Voeltzel et al. [25] also observed that the larger the slip, the lower the effective shear rate in the liquid, so that the fluid is less heated.

Furthermore, the molecule length and shape can also influence slip. Indeed, the longer and the more complex chains are, the stronger is the fluid cohesion and thus it will enhance slip [182, 161]. As for the layering structuration, the topography influence the interfacial flow. It was shown experimentally [183, 184, 185] and numerically [25, 36, 170, 186, 180] that roughness reduces wall slip.

I.4.2.3   Rheology of nanoconfined fluid

The effective viscosity η_{eff} of nanoconfined fluids has to be distinguished from the bulk viscosity η. This latter describes the resistance of a fluid to flow and only depends on three factors: pressure P, temperature T and shear rate $\dot{\gamma}$ so that $\eta = \eta(P,T,\dot{\gamma})$. However, in nanoconfined fluids, the distance between the two surfaces influences the fluid flow. In nanoconfined systems, the effective viscosity η_{eff} represents the resistance to flow in a molecularly thin fluid. It is defined as the shear stress divided by effective shear rate. Under high confinement, various studies see varied behaviors, which range from no change to viscosity increase by several orders of magnitude, depending on the liquid and the solid [187, 188].

The viscosity increase can be linked to the layering effect. Indeed, the high density observed near the surfaces generates an increase in viscosity, or even a phenomenon of locking. In both cases, the apparent viscosity rises. For this reason, this increase in viscosity occurs only when the thickness of the contact becomes comparable to the thickness of the structured layers formed close to the surfaces. Indeed, SFA experiments showed a rise of the viscosity when less than 10 molecular layers of hexadecane were present in the contact [189]. This observation was confirmed with simulations of n-dodecane [190] and model fluids [174, 191]. Moreover, when the film is thicker than 10 molecular layers, the effective viscosity is comprised within 10% of the bulk value [192]. When the film becomes even thinner with only 1-2 molecular layers, the lubricant crystalizes and a solid-like behavior is assumed, leading to an increase of the effective viscosity [189, 193]. In this case, a stick-slip behavior at the liquid-solid interface was confirmed experimentally [193] , as well as with numerical simulations [191, 194].

Furthermore, as shown in Figure I.16, the effective viscosity shows different regimes, according to the shear rate. At relatively low shear rate, the transition from a solid-like to a liquid-like behavior appears when a critical yield stress is reached [195, 196, 191, 197, 169]. At high shear rate, viscosity decreases with $\dot{\gamma}$. This phenomenon is called shear thinning.
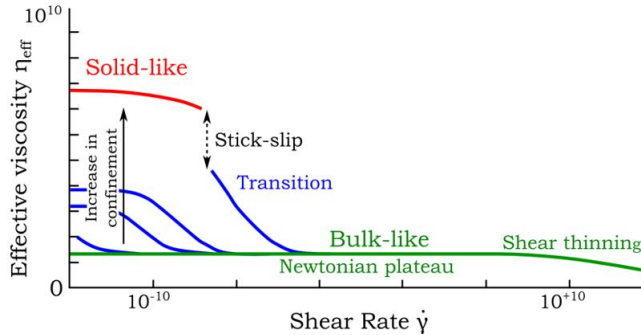
Figure I.16: Generalized map in arbitrary units for the effective viscosity of confined films as a function of the shear rate, load and film thickness. Inspired by Luengo et al. [195] and modified by Savio [37].

I.4.2.4   Thermal effects

High shear produces heat in the contact. In return, heat can be evacuated either by the lubricant flow towards the exit of the contact, or by conduction through the solid surfaces.

Thanks to molecular dynamics simulations, Voeltzel et al. [198] have drawn a typical temperature profile obtained for nanoconfined ionic liquid between two iron oxide surfaces. As shown in Figure I.17, they observed an interfacial thermal slip due to a finite thermal resistance of the interface. They also found that this thermal resistance increases with the effective shear rate.

In conclusion, continuous theories cannot be used anymore for molecular lubrication. Indeed, many properties of the fluid (e.g. slip at the wall, inhomogeneity through the film thickness) deviate from classical continuum assumptions when confined between two surfaces. Nanoconfined systems, though widely studied in the literature, still require investigations. Especially, the physico-chemical behavior at the interface between the lubricant and the surface remains poorly described in literature when considering real surfaces. Besides, as explained above, molecular lubrication with refrigerants is an open field of research.
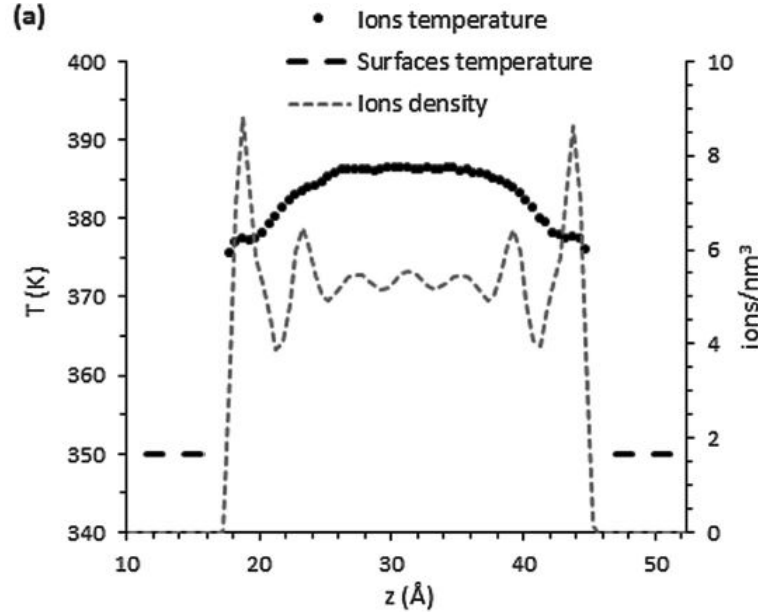
Figure I.17: Typical temperature profile of sheared ionic liquid, for a shear velocity of 40 m/s, a pressure of 500MPa and a wall temperature of 350 K. Results from Voeltzel et al. [198].

I.4.3 Role of adsorbed layers of refrigerant on the surface

Some refrigerants can chemically react with the bearing surfaces. For example, under high velocity and high pressure, ammonia reacts with the oxide layers and free water is released, so that the surface loses its protective oxide layer up to a few millimeters per day. As a consequence, wear increases and the mechanical system fail [139]. In classical lubricants, anti-wear additives can improve tribological performance. Besides, as shown in this Chapter, some refrigerants are prone to react with surfaces and to build-up adsorbed layers protecting the surfaces.

The new HFOs and HCFOs refrigerants have a carbon-carbon double bond C=C, which is known to be more reactive than the single carbon bond. Indeed, the electrons of the π-bonds are less stable than the ones of the σ-bonds. In a lubricated contact, material removal can appear, for example because of two asperities contact, involving breaking bonds in the surface. As a consequence dangling bonds are created at the interface with the refrigerant. The unstable C=C bonds are then inclined to react with these dangling bonds. The formation of this adsorbed layer depends on different parameters.

First, the oil blended with the refrigerant can influence the ability of the adsorption process. As an illustration, the tribological properties of the R1234yf refrigerant were experimentally investigated between two gray cast iron surfaces [119, 22]. During tribotesting, a protective layer appeared. Thanks to X-ray photoelectron spectroscopy (XPS) analysis, the chemical composition of this layer was investigated and fluorine-based species were observed. With gray cast iron surfaces and R1234yf environment representing

45

an aggressive air-conditioning compressor systems in mixed lubrication regime, different oil-refrigerant mixture were used [114]. An adsorbed layer appeared in the case of PAG/R1234yf and mineral oil/R1233yf, but not with the mixture POE/R1234yf, leading to abrasive wear with micro-pitting and break-down of the surface.

Second, the temperature dependence on the formation of protective layer was tested in the same studies. The increase of temperature changed the ability to form an adsorbed layer. At room temperature with R1234yf/PAG and R1234yf/mineral oil mixtures, no sorption appeared, but at 110°C, fluorine-based layer was observed. The pressure can also influence the formation of a tribolayer, as observed with R134a on alumina and zirconia surfaces [199].

Finally, even with R134a or natural CO_2 refrigerants without carbon-carbon double bond, tribolayers were observed on different iron oxides, alumina, zirconia and polymeric coatings [200, 201, 202, 203]. The better tribological performance with CO_2 refrigerant compared to R134a in cast iron air-conditioning compressor was attributed with XPS to the partial transformation of iron oxide into iron carbonates, reducing friction and preventing wear [204, 122].

Muraki et al. [20] observed with XPS the formation of FeF_2 showing antiwear behavior when considering the refrigerant R245mc. Byung Chul Na et al. [21] supposed an iron-chloride coating formation with the former refrigerant dichlorodifluoromethane (R12) to justify a decreasing friction.

However, concerning the HCFO-1233zd in a steel contact no experimental or numerical result about the formation of an adsorbed layer was found in the literature except the experimental works published by Morales-Espejel [3] and Hauleitner et al. [4, 5]. This thesis aims at filling the gap in the point of view of numerical simulations and at providing information about the formation of this layer and its influence on tribological performance in such PRL systems.

I.5   Objectives of the PhD

One of the main industrial challenges consists in reducing the size, weight and environmental impact of tribological systems. In refrigeration systems, compressors are usually lubricated with an oil-refrigerant mixture instead of oil lubricant. However the current trend is to build oil-free systems with compressors only lubricated with pure refrigerants (PRL systems), which are low-viscosity working fluids and have low viscosity-pressure coefficients. Hence, the thickness of lubricant films separating the surfaces can reach the nanometric scale locally and thus the same order of magnitude as surface roughness (few nm). Therefore, contacts between asperities could happen and it would provoke

wear. In the literature, experiments have shown that no damage or wear were observed on the stainless steel surface under certain experimental conditions with PRL systems lubricated using R1233zd. This project aims at understanding the physical chemistry behavior between a steel surface and the new refrigerant R1233zd and its effects on tribological performances.

Experiments with the R1233zd refrigerant suggest that lubrication is still possible in that situation thanks to an adsorbed layer formed on steel surfaces. Because experimental in-situ analysis inside the contact area is still very difficult, we aim at providing numerical simulations to observe the chemical reactions and physical processes at the interface between the refrigerant and the surface.

In that context, we develop a multiscale numerical methodology where DFT calculations, describing matter at the level of its electronic structure, are combined with large scale molecular dynamics simulations, using empirical force fields adapted on the basis of the DFT results. First, the results obtained with DFT are detailed in Chapter 2 and the interactions between refrigerant and hematite are explained. DFT calculations are used to obtain accurate binding energies under different conformations. Then, the methodology used to parametrize a force field at the refrigerant-surface interface based on these DFT results is discussed in Chapter 3. MD simultations are used to predict the difference of interfacial structure observed with the parametrized force field and from those obtained using standard mixing rules. In Chapter 4, large-scale molecular dynamics simulations involving this parametrized force field analyze the existence of a strongly adsorbed layer of R1233zd molecules. The strength of this adsorbed layer is explored under extreme conditions in pressure and sliding velocity in presence of smooth and rough surfaces.

Chapter II

Chemical physics at interfaces within a refrigerant-lubricated contact: an electronic structure study

Contents

The results of this chapter have been partially published in the Journal of Physical Chemistry C [6].

For a few decades, interest for quantum calculations has been increasing. Indeed, quantum calculations can predict the electronic structure of the matter. From physical chemistry aspects and even now from industrial interests, electronic properties are of primary importance.

Ab-initio methods aim at solving quantum mechanics equations, which are mostly simplified forms of the Schrödinger equation. Indeed, this latter is very difficult to solve as soon as many electrons composed the system. One of the most popular among these methods is the density functional theory (DFT), using the electronic density feature to solve a many-body problem. DFT calculations have been tested to describe various phenomena in different areas of science. For example, one can study purely chemical process like ammonia synthesis or hydrogenation [7], or mechanical behavior of metals embrittlement, or even study the materials properties during planetary formation [8]. In particular, DFT method offers the possibility to investigate lubrication phenomena. Indeed, DFT have been tested to investigate friction through chemical reactions at the solid-liquid interface [9]. DFT has also been used to parametrized force fields between lubricant and surfaces in lubricated contacts [10, 11].

This Chapter is divided into three main parts. First, the principles of DFT are explained. Then, our model and its features are detailed. Finally, the results about the adsorption of the R1233zd molecule on hematite surfaces are presented and discussed. In particular, DFT calculations are used to obtain accurate binding energies under different conformations. Moreover, charges analysis are performed with representative adsorption cases.

II.1   Density Functional Theory

II.1.1   Basic elements of quantum mechanic

II.1.1.1   Born-Oppenheimer approximation

The Born-Oppenheimer approximation [205] is the assumption that the motion of electrons and atomic nuclei can be separated. Indeed each neutron or proton in a nucleus is more than 1800 times heavier than the electron [8]. Therefore, the electrons move and interact in the field of a set of immobile nuclei, and the forces between the nuclei can be computed from the relaxed electronic structure at every time.

II.1.1.2 The Schrödinger equation

With the Born-Oppenheimer approximation, the time-independent Schrödinger equation for the electrons can be written as follows.

$$\hat{H}\Psi = (\hat{T}_e + \hat{V}_{n-e} + \hat{V}_{e-e})\Psi = E\Psi \tag{II.1}$$

$\hat{H}$ represents the Hamiltonian operator, which can be decomposed as follows: $\hat{T}_e$ is the kinetic energy of the electrons, $\hat{V}_{n-e}$ is the potential developed by the collection of atomic nuclei and acting on the electrons, $\hat{V}_{e-e}$ describes the electron-electron interactions. Ψ is a set of solutions of the Schrödinger equations and are the eigenvectors of the Hamiltonian, and named electronic wave functions. Each wave function Ψ_n is associated to its eigenvalue, the energy E_n. The many-body problem is solved by finding the wave functions and their ground state energy E_0.

If the spin is neglected, the electronic wave function Ψ is dependent of each spatial coordinates of each N electrons, thus it is a problem with 3N spatial coordinates. With the spin, each electron is completely defined by its three spatial coordinates and its spin. The number of electrons makes practically impossible to solve the Equation II.1 for real systems. The exact solution is limited for very few and small systems such as the H atom.

The system considered in this chapter, as shown later, is composed of one molecule of R1233zd and one hematite ($\alpha - Fe_2O_3$) surface containing 72 atoms of oxygen and 48 atoms of iron. By neglecting the spin, the full wave function of this system requires 192 dimensions for the refrigerant molecule and 5472 dimensions for the surface. The DFT has been developed to overcome this very high number. Indeed, instead of considering 5664 dimensions for the wave function, the systems will be solved by using an electronic density, which is only a 3 dimensional function (when excluding the spin), for 3 spatial coordinates.

II.1.1.3 The electron density

The electron density is defined as the probability of finding any of the N electrons within a volume element. The electron density at a particular position in space $n(\mathbf{r})$ is calculated with the following formula:

$$n(\mathbf{r}) = \sum_{i=1}^{N} \mid \psi_i(\mathbf{r}) \mid^2 \tag{II.2}$$

where ψ_i represents a single-electron wave function and is also named a molecular orbital

(MO). Therefore, the term in the sum is the probability that an electron in the molecular orbital ψ_i is located at the position $\mathbf{r}$. To consider the magnetism of certain systems, the spins of electrons have to be considered. These systems are named spin-polarized and their electron densities depends of three spatial coordinates and one spin each.

II.1.2 Principles of Density Functional Theory

In DFT calculations, the many-body problem of N electrons with 3N spatial coordinates is reduced to 3 spatial coordinates, through the use of functionals of the electron density. A functional is a function, which gives a number from a function. The main idea of DFT is that the ground state energy can be expressed as a functional of the electron density. Indeed, in DFT calculations, the Hamiltonian can be expressed as a function of the electron density. This basis of the DFT appeared with the Hohenberg-Kohn theorems.

II.1.2.1 Hohenberg-Kohn theorems

The first Hohenberg-Kohn theorem demonstrates that the ground state properties of a many-electron system is a unique functional of the electron density.

The second Hohenberg-Kohn theorem provides precisions about the functional. It says that the electron density that minimizes the energy of the overall functional is the true electron density corresponding to the full solution of the Schrödinger equation. It means that the ground state energy can be obtained variationally.

$$E[n(\mathbf{r})] \geqslant E[n_0(\mathbf{r})] = E_0 \tag{II.3}$$

Therefore, the aim is to find the lowest energy value, thus the ground state energy of a system. If the true functional was known, by varying the electron density until the energy is minimized, it would be possible to obtain the electron density corresponding to the ground state energy. Thus, according to the two theorems of Hohenberg and Kohn, one can know the state of an electronic system by determining its electronic density and one can obtain the electronic density of the ground state by minimizing the energy of the system.

However, the Hohenberg-Kohn theorems do not give information on how to calculate the energy with the electron density, i.e. they do not prescribe how to chose or design the functional. Therefore, approximations have to be done. Only by adding the formulations of Kohn and Sham, DFT became a practical method to solve a many-body problem.

II.1.2.2 Kohn-Sham equations

Instead of solving the many-body problem (Equation II.1), Kohn and Sham introduced single-electron equations, named Kohn-Sham (KS) equations (Equations II.4). They replaced the electron-electron potential and the electron kinetic energy of interacting electrons by terms of fictious non interacting electrons system. Effects arising from many-body interactions between electron-electron are put into a new term, named exchange-correlation potential. In KS equations, the wave functions Ψ introduced above, are replaced by single-electron wave functions ψ_i depending on three spatial variables.

$$\left[-\frac{\hbar^2}{2m} \nabla^2 + V(\mathbf{r}) + V_H(\mathbf{r}) + V_{XC}(\mathbf{r}) \right] \psi_i(\mathbf{r}) = \varepsilon_i \psi_i(\mathbf{r}) \qquad \text{(II.4)}$$

The first term describes the kinetic energy of the electron, V is the potential energy of an electron interacting with the collection of atomic nuclei, V_H is the Hartree term describing electron-electron Coulomb repulsion, and V_{XC} is the exchange-correlation potential. This latter describes the effects of electron-electron interaction, excluding Coulomb repulsion already considered in Hartree term, and also corrects the kinetic energy due to the non-interaction. All these four terms are calculated as functions of the electron density $n(\mathbf{r})$. They are functionals of the density. The aim is to solve these KS equations.

II.1.2.3 SCF: self-consistent field procedure: solutions of Kohn-Sham equations

To solve the Kohn-Sham equations, one needs to define the four potentials terms of Equation II.4, which are depending on the electron density $n(\mathbf{r})$. However the density depends on the single-electron wave functions ψ_i which are the solutions of the Kohn-Sham equations, which are initially needed. Hence, it is a circular problem. Therefore, an iterative procedure need to be used to find these molecular orbitals ψ_i. This procedure is named a self-consistent field (SCF) calculation and the different stages are described below.

- An initial electron density $n^0(\mathbf{r})$ is defined, in general a charge density superposition of the isolated atoms.

- With this density, the Hamiltonian is calculated and each N KS equations $\hat{H}\psi_i(\mathbf{r}) = E\psi_i(\mathbf{r})$ are solved with this density. Hence, single-particle wave function $\psi_i(\mathbf{r})$ are calculated.

- The new electron density $n^1(\mathbf{r})$ is determined from the calculated molecular orbitals $\psi_i(\mathbf{r})$ with the Equation II.2.

- This new density is then compared to the previous one and if $\mid n^1(\mathbf{r}) - n^0(\mathbf{r}) \mid$ lower than tolerance, then the SCF calculation stops and the new electron density $n^1(\mathbf{r})$ can be used to obtain energies, forces or other properties. Otherwise, this new density is used as initial density to restart this procedure at the second step.

To summarize the previous steps, the aim is to find the ground state energy of the Schrödinger equation. However, because of the many-body feature, it is too complicated for real systems. Thanks to the Hohenberg-Kohn theorems it is possible to obtain this ground state by minimizing the energy functional depending of the electron density. With the Kohn-Sham equations, the many-body problem of the beginning is simplified and from now, single-electron equations will be solved by using a self-consistent procedure. Nonetheless, the exchange-correlation potential $V_{XC}(\mathbf{r})$ has to be approximated. This latter is linked to an exchange-correlation functional $E_{XC}[n(\mathbf{r})]$ with the following formula.

$$V_{XC}(\mathbf{r}) = \frac{\delta E_{XC}[n(\mathbf{r})]}{\delta n(\mathbf{r})} \tag{II.5}$$

II.1.2.4 Exchange-correlation functionals

Theoretically, DFT is an exact method but one problem is that no analytical formulation of the exchange-correlation functional $E_{XC}[n(\mathbf{r})]$ exists. Two of the most usual kinds of functional are presented here.

The exact exchange-correlation energy can be determined for the case of an uniform electron gas [206]. This energy is used in the **Local Density Approximation (LDA)**. In LDA, the XC functional depends only of the density, as described in the following formula.

$$E_{XC}^{LDA}[n(\mathbf{r})] = \int n(\mathbf{r})\varepsilon_{xc}(n(\mathbf{r}))d\mathbf{r} \tag{II.6}$$

Where, at each spatial position $\mathbf{r}$, $\varepsilon_{xc}[n(\mathbf{r})]$ is the exchange-correlation energy for a particle in a uniform electron gas at the density $n(\mathbf{r})$. Nonetheless, this approximation remains a local approximation in which the non-homogeneity of the electronic density is not considered.

To add more information in the functional that the local electron density, the **Generalized Gradient Approximation (GGA)** can be implemented. In GGA, the gradient of the electron density is included, as shown in the following formula.

$$E_{XC}^{GGA}[n(\mathbf{r})] = \int n(\mathbf{r})\varepsilon_{xc}(n(\mathbf{r}),\nabla n(\mathbf{r}))d\mathbf{r} \tag{II.7}$$

The particular vdW functionals. Dispersion interactions (also named van der Waals interactions or London forces) relate to interactions between instantaneous dipoles. Indeed, within a molecule, an instantaneous dipole can be produced due to the fluctuation of electrons position. This dipole will interact with instantaneous dipoles of other molecules. These long-range correlation interactions are difficult to describe with DFT due to their long-range feature. Indeed, dispersion forces need to be computed in large simulation cells, which increase drastically the computation costs.

Describing these interactions is one of the limit of DFT calculations. However, two main solutions exist to improve description of dispersion interactions. One can either use correction terms which add a dispersion contribution to the total energy between each pair of atoms in a system. Or, one can use vdW density functional (vdW-DF) to approximate dispersion interactions. In contrary to the previous solution, this one implements two terms depending on the electron density, into the exchange-correlation energy term. In this work, we use a GGA functional modified to take into account dispersion interactions, the optB88-vdW.

II.1.2.5 The core electrons

The core electrons do not participate in conductivity or creating-breaking bonds but they have also to be treated. However, consider them in same way than valence electrons is too computationally expensive. One possibility is to use pseudopotentials, as it will be done in our study. With this method, the effects of the core electrons are described through a potential acting on the molecular orbitals of the valence electrons, reducing the calculation costs.

II.1.2.6 Basis sets

The molecular orbitals, thus the single-electron wave functions, are projected on basis functions. These functions can be for example plane-waves functions or localized functions. The plane-waves functions are powerful for calculations involving three dimensional periodic boundary conditions. However, when the adsorption phenomena are studied, a large empty volume is set-up upon the surface. In order to optimize the calculation costs, it is interesting to consider localized functions to keep the vacuum area without basis functions. With CP2K software [12], localized Gaussian basis functions are used, as follows.

$$\psi_i(\mathbf{r}) = \sum_{\alpha}^{N_{BF}} C_{i\alpha} G_\alpha(\mathbf{r}) \tag{II.8}$$

Where N_{BF} is the number of basis functions G_α. $C_{i\alpha}$ represent the coefficients calculated during the SCF procedure. In practice G_α are linear combinations of "contracted Gaussian" (CG) basis functions. CGs are composed of Gaussian functions multiplied by functions depending on spatial coordinates. For example, the single-zeta (SZ) basis function is composed of one contracted Gaussian function per atomic orbital (AO), while double-zeta (DZ) owns two CG functions per AO and triple-zeta (TZ) three per AO.

Furthermore, the basis functions can take into account the polarization. Indeed, by approaching two atoms, the molecular orbitals can be more asymmetrical about the nucleus than the atomic orbitals. To describe the polarization effect, the CGs can have higher angular momentum than in the valence orbitals. This flexibility is obtained by using polarized basis sets, such as double-zeta polarized (DZP) or triple-zeta polarized (TZP) functions. The polarization functions are important to reproduce chemical bondings and will therefore be used in this study.

Besides, as discussed previously, since the core electrons do not participate in bonding phenomena, they are treated separately. Hence, the basis sets will only be applied to valence electrons and not to every electrons of each atoms. For instance, the DZP basis set becomes the double-zeta *valence* polarized (DZVP).

One particularity with CP2K software is that a Gaussian and Plane Waves (GWP) method is used, whereas only Plane Waves (PW) method are used for many other software, such as VASP [207]. While the molecular orbitals are projected on Gaussian functions, a multi-grids system is used to define the points where the electronic density is calculated for hartree and exchange-correlation terms. The distance between two planes of this grid is directly obtained from an energy cutoff value given for the plane waves. The higher the cutoff value, the finer the grid and thus the more precise the calculation.

II.1.3   DFT+U calculations

As explained above, electron-electron Coulomb repulsion is described with the Hartree potential, while all other interactions between electrons are included in the exchange-correlation term. In the single-electron KS equations, the Hartree potential describes the repulsive interactions between the electron and the total electron density, including the considered electron itself. This unphysical repulsive interaction between the electron and itself leads to an energy named self-interaction energy. Theoretically, this latter should be corrected in the exchange-correlation term. However, since the exact exchange-correlation functional is not known, the self-interaction energy can involve non-negligible effects for highly correlated systems. This is particularly true for systems owning many localized states in the atomic center. Such systems are referred to as strongly correlated systems and are for example transition-metal oxides whose d or f shells are incomplete.

To solve this problem, the DFT+U method has been developed. In this method, self-interactions in localized states are calculated with the Hartree-Fock method and all the remaining states are treated with classical DFT calculations. Indeed, self-interactions errors are canceled in Hartree-Fock calculations. The DFT+U method introduces a numerical parameter correcting the self-interaction error [8, 15, 18, 17].

II.2 Our model

II.2.1 Materials

In this section, we study the adsorption of refrigerant molecules at the quantum level by considering a set of positions and orientations of one R1233zd molecule near a steel surface. Steel is a metallic material constituted by crystals of different natures. XPS analyses on steel before PRL experiments with R1233zd [4, 5], reveal that the surface is mainly constituted of different types of iron oxides, among them FeO and Fe_2O_3. As shown in Figure II.1, in this study the surface of iron oxide is described with hematite $\alpha-Fe_2O_3$, which is the most thermodynamically stable form of iron oxide under ambient environment and thus, the most common on earth. The choice was made to consider the $(01\bar{1}2)$ orientation because of the presence of both iron and oxygen atoms on the upper layer. Therefore a representative set of interactions between atoms of the refrigerant and the surface will be considered. For the refrigerant, we consider R1233zd. As represented in Figure II.1, the R1233zd molecule is composed of a CF_3 group next to a double-carbon bond. The sp^2 carbon in the middle is linked to a hydrogen named H2 and the second sp^2 carbon to one hydrogen H1 and one Cl atom. The *(x,y,z)* dimensions of the relaxed hematite is approximately of 10 Å × 10 Å × 10 Å.
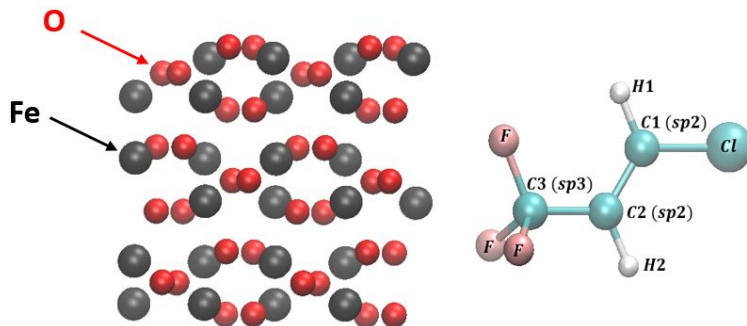
Figure II.1: Hematite $\alpha - Fe_2O_3(01\bar{1}2)$ relaxed surface (left) and R1233zd molecule (right).

In order to study the adsorption of R1233zd molecules on hematite $(\alpha-Fe_2O_3)$ surfaces, the CP2K/QUICKSTEP[12] code (version 3.0) is used to perform DFT calculations. Because van der Waals dispersion forces are of primary importance to describe liquids

and the interfacial behavior, the exchange-correlation term is calculated within the generalized gradient approximation GGA with the non-local optB88-vdW functional[13]. Dabaghmanesh et al. [14] showed that this functional is accurate for methane and benzene adsorption on hematite surface. The pseudopotentials of Goedecker-Teter-Hutte are employed [208].

The aim is to find the lowest energy value of the whole system composed of one molecule of the R1233zd and one Fe_2O_3 surface formed with 120 atoms. Because the surface is already relaxed, iron and oxygen atoms remain fixed during the geometry optimization and only the molecule of refrigerant can move. Note that to study the reactivity of the system (e.g. possible dissociation of the refrigerant molecule), it could have been interesting to let the hematite surface relax. The simulation box dimensions were 10.24 Å × 10.93 Å × 25 Å, which leaves a vacuum gap of ca. 1 nm between the top of the molecule and the bottom of the periodic image of the solid surface. With the standard DFT method, the Fe 3d strong correlated electrons are not well described. Therefore the DFT-GGA+U method, in which a Hubbard-type on-site Coulomb repulsive term is added to the Hamiltonian, was used. The challenging point we face here is to employ a van der Waals functional combined with a spin-polarized system by using the named GGA+U method. The convergence of a geometry optimization process is much more difficult with the DFT+U method and it is often necessary to use different methods (standard DFT followed by DFT+U) to perform this convergence.

II.2.2   Standard DFT - DFT+U setup

Standard DFT method:

For calculations without DFT+U method, geometry optimizations were carried out in order to solve the Kohn-Sham equations. The short range molecularly optimized double-ζ valence polarized (m-DZVP) Gaussian basis functions were used. A cutoff value of 300 Ry was used for the plane wave expansion. The Kohn-Sham matrix is iteratively diagonalized with the Orbital Transformation method.

DFT+U method:

All calculations using the DFT+U method were performed spin-polarized by solving the unrestricted Kohn-Sham equation. In this study, the Dudarev's approach for DFT+U method, is used [15]. A value U = 5 eV predicts correctly the hybridization of 3d-electrons of iron atoms[16, 17]. A ramping method is used from a threshold value of the self-consistent field (SCF) convergence of 10^{-4} to incrementally increase the U value to target U (5 eV) value with an increment of 0.5 eV. Different values were tested and these latter did show the best capacity to converge the calculus. The short range molecularly optimized single-ζ valence polarized (m-SZV) Gaussian basis functions were

59

used for every atom and the final plane-wave cutoff was set to 500 Ry. The modified Broyden mixing method is used in order to improve the convergence behavior of the SCF procedure[209]. Moreover, due to the antiferromagnetic behavior of the hematite this convergence is enhanced by setting an initial multiplicity value to one. The Fermi-Dirac smearing method was used with an electronic temperature of 3000 K. Since smearing can lead to occupied molecular orbitals (MOs) in conduction band, additional empty MOs were added to represent the initially unoccupied orbital in this band. Finally, the Kohn-Sham matrix was diagonalized with standard methods.

II.2.3   Binding energy

The adsorption behavior of R1233zd on the $(01\bar{1}2)$ $\alpha - Fe_2O_3$ was studied and the binding energy values Eb were calculated with the following formula:
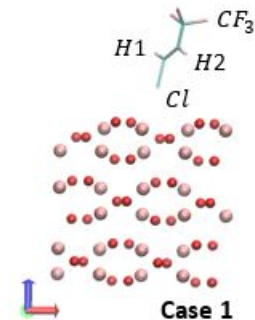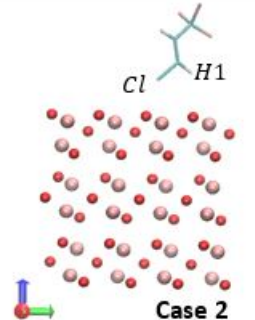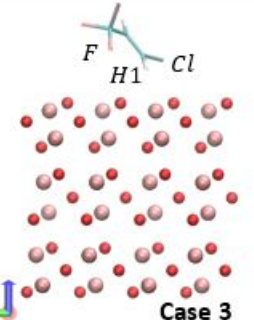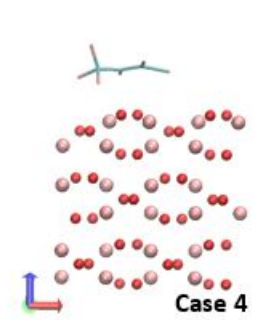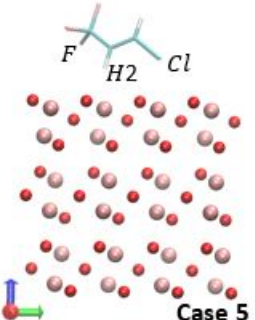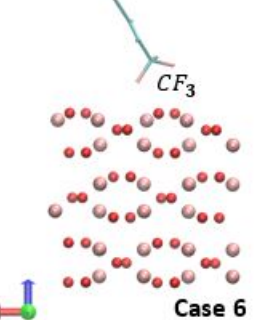
$$Eb = E_{\{surface+1mol_{R1233zd}\}} - E_{\text{surface}} - E_{1mol_{R1233zd}} \qquad \text{(II.9)}$$

where $E_{surface+1mol_{R1233zd}}$ is the total energy of the relaxed adsorbate-substrate system, E_{surface} is the energy of the clean surface slab and $E_{1mol_{R1233zd}}$ is the energy of the isolated R1233zd molecule. The two last terms are calculated by using the same geometry as the $\{surface + 1mol_{R1233zd}\}$ system optimized one. A negative value of the binding energy means that the obtained geometry is more stable than the unbounded state.

II.3 Adsorption behavior of R1233zd molecule on iron oxide surfaces

II.3.1 Binding energies

Sixteen different initial configurations have been obtained by translating and rotating randomly the refrigerant molecule with respect to the three directions. As shown in Table II.1 below, the adsorption possibilities could be classified into six different cases (each corresponding to similar positions and orientations), associated to six ranges of binding energy values. Every adsorption results is visualized with the visual molecular dynamics (VMD) software[19].

Case 1	Case 2	Case 3
$E_b \in [-0.45; -0.22]\, eV$	$E_b \in [-0.57; -0.50]\, eV$	$E_b \in [-0.66; -0.64]\, eV$
$E_b\; 4, 12, 13, 14$	$E_b\; 2, 10, 11, 16$	$E_b\; 5, 9, 15$
Case 4	Case 5	Case 6
$E_b \in [-0.92; -0.82]\, eV$	$E_b \approx -0.70\, eV$	$E_b \approx -0.47\, eV$
$E_b\; 6, 7, 8$	$E_b\; 1$	$E_b\; 3$

Table II.1: Six different kinds of adsorption possibility with the ranges of binding energy values and the geometry optimization number.

The first important result is that chlorine atoms strongly interact with iron atoms, as shown in Table II.1, case 1. The chlorine can interact with the oxygen atoms as well. However, it involves to decrease the distance between iron and chlorine and the binding energy will decrease. Therefore we can conclude that the Cl-Fe interaction is of major importance. During geometry optimization process, it is also possible that the molecule of refrigerant leans and the hydrogen H1 located near the chlorine will play a non-negligible role of stabilization, as shown in case 2. In case 3, it is shown that the fluorine has to be taken into account, with a lower energy value of around -0.65 eV. The assumption of possible interaction between iron and fluorine atoms had been raised[20], although it was with another refrigerant. We obtained the strongest interaction for case 4. Indeed, the binding energies with refrigerant molecules parallel to the hematite surface are higher than the ones with vertical orientations of the molecule. Therefore it means that the horizontal positions of the refrigerant molecules are more stable than the vertical ones. Indeed both interactions between fluorine – surface and between chlorine – surface will play a role. Moreover, the π-bonding of the double carbon bond could play a role. For case 5, the molecule rotated along the double-carbon bond axis and both chlorine and fluorine, as well as the hydrogen H2 bonded with the carbon located in the middle of the molecule, interact with the surface. In case 6, only the fluorine atoms interact with the surface. The geometry optimization for the latter orientation of the molecule was the less trivial to obtain numerically. It is also interesting to observe that we could obtain the same binding energy value with one molecule adsorbed either thanks to the three fluorine atoms or with only the chlorine atom. It shows what was hypothesized in the paper of Na et al. [21] with another refrigerant, dichlorodifluoromethane R12, about an iron-chloride coating formation. Indeed, chlorine and iron atoms strongly interact and the R1233zd molecule can be adsorbed with a major contribution of van der Waals interactions between these two atoms and of course because of all coulombic interactions. Moreover, Akram et al. reported the formation of a fluorine-enriched film FeF_3 for the R1234yf[22]. Therefore it is possible to link this observation to case 6 optimized geometry.

It could happen that organic molecules decompose by approaching a metal surface and build an amorphous film mostly composed of the molecule atoms[210]. It would be problematic here because it would mean that the refrigerant would not be able to interact with any iron or oxygen atoms because of presence of an amorphous phase at the interface. Furthermore, R1233zd molecules may not remain stable when approaching the surface due to the double-carbon bonds. However, in this study no dissociation phenomenon was observed.

In this ab-initio study, we have shown that the R1233zd molecule could strongly adsorb on an iron oxide surface. This adsorption was characterized by considering a set of position and orientation of the molecule upon the surface, which could be found in a

lubricated contact. These information about reactivity of the surface with the refrigerant obtained from DFT calculations will then be retained in a force field in order to study much larger systems, as detailed in Chapter 3.

II.3.2 Basis set superposition error

Using finite Gaussian basis sets leads to an error named "basis set superposition error (BSSE)" [211]. When two atoms approach, basis sets of both atoms can overlap and one atom can use the basis of the second atom to project its molecular orbitals. In this study, adsorption energies were calculated between one R1233zd molecule and the hematite surface. In particular, the BSSE can deteriorate the binding energy values when basis sets of the surface are used to project molecular orbitals of refrigerant atoms.

To estimate the basis set superposition error, the total energy of the molecule for 6 representative orientations is calculated by considering two basis sets: first, the basis set of the isolated molecule, and second, the basis set of the whole system. The errors obtained because of basis set superposition are calculated for six representative cases, as shown in Table II.2.

	Difference [meV]
Eb1	-21.7
Eb2	-19.9
Eb3	-19.8
Eb5	-27.3
Eb7	-47.0
Eb13	-11.1

Table II.2: Basis set superposition errors. These energies are calculated in 6 representative cases, in reference to the ones in II.1.

The difference in energy was always lower than 47 meV, this maximum value corresponding to a flat orientation of the molecule. Indeed, this case represents the adsorption geometry that is the more favourable for sharing basis sets between the surface and the R1233zd molecule.

II.3.3 Dipole correction

Because of considering here a periodic system only in x and y directions, an empty space of ca. 1 nm between the top of the molecule and the bottom of the periodic image of the solid surface is added. However, the R1233zd molecule is polar and can therefore interact with its periodic polar images through dipole-dipole interactions. To

eliminate these artificial interactions, the dipole correction method can be used where an additional compensating field is added in the z direction.

In this work, no dipole correction was included in the DFT calculations. However, we computed the effect of the dipole correction for the six representative cases, reported in the Table II.3 below.

	Difference [meV]
Eb1	0.4
Eb2	-18.1
Eb3	-4.8
Eb5	-15.6
Eb7	-13.3
Eb13	-9.3

Table II.3: Difference between the total system energy by considering the dipole correction and without the correction. These energies are calculated in 6 representative cases, in reference to the ones in II.1.

The maximum error obtained on total energy of optimized geometries is ca. 18 meV while the number of steps needed to converge the SCF is doubled when including the dipole correction. Because of these small error values compared to the high increase of simulation time, we decided to neglect the dipole correction in z-direction.

II.3.4 Charge analysis: physisorption or chemisorption?

This section is devoted to the analysis of charges within R1233zd molecule during adsorption process to distinguish the kind of sorption occuring. While methods like CHELPG (CHarges from ELectrostatic Potentials using a Grid-based method) [212, 31, 213] are used to calculate atomic charges, other charges distribution analysis schemes give an answer about the kind of sorption resulting. Besides, CHELPG calculation scheme was used by Raabe to design atomic charges of R1233zd for Coulombic potential [31].

On the other hand, Bader charges analysis are more adapted to determine exchanged charges between atoms and molecules. Bader charges are computed using the approach developed at the Henkelman group [214, 215, 216, 217]. Bader's theory divides molecules into atoms, only based on the electron density. In molecular systems, the charge density reaches a minimum between atoms and therefore, the atoms are separated from each other at this place, dividing the total volume in smaller volumes assigned to each atoms in which electron density is calculated. Bader's theory is known to be useful for charge analysis. In particular, this approach can be used to describe chemical bonding between interacting atoms and molecules.

As this method is developed for plane wave based DFT calculations, VASP software is used in this section to calculate Bader charges distribution. To represent the electrons exchange between R1233zd molecule and hematite surface during the adsorption process, exchanged charges are calculated as a difference between the charges of each R1233zd atoms in the total {surface+R1233zd} system in adsorbed geometry and the charges of each R1233zd atoms of the isolated molecule in adsorbed geometry. Then, the charges difference of each atoms are added in a global exchanged charge. Figure II.2 represents this global exchanged charge for the six representative adsorption cases. Every representative adsorption case is associated to a snapshot of the adsorption geometry to better understand the chemical behavior.
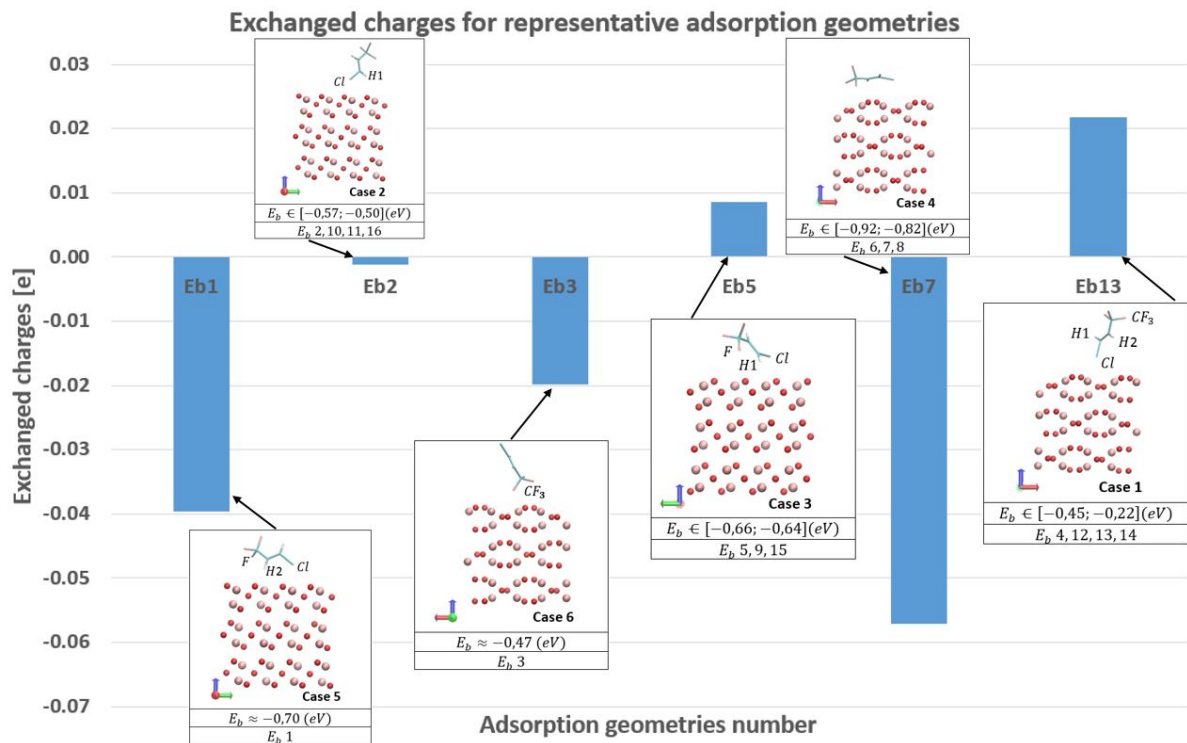
Figure II.2: Exchanged charges of R1233zd molecules with the surface during adsorption process. These charges are calculated in 6 representative cases, in reference to the ones in Table II.1.

A negative exchanged charge means that the surface gained an amount of the R1233zd charge, whereas a positive value means that the R1233zd gained an amount of charge. To investigate the role of each atom in adsorption process, the exchanged charge distribution is represented for each of the nine atoms of the molecule and every representative adsorption geometry in Figure II.3.
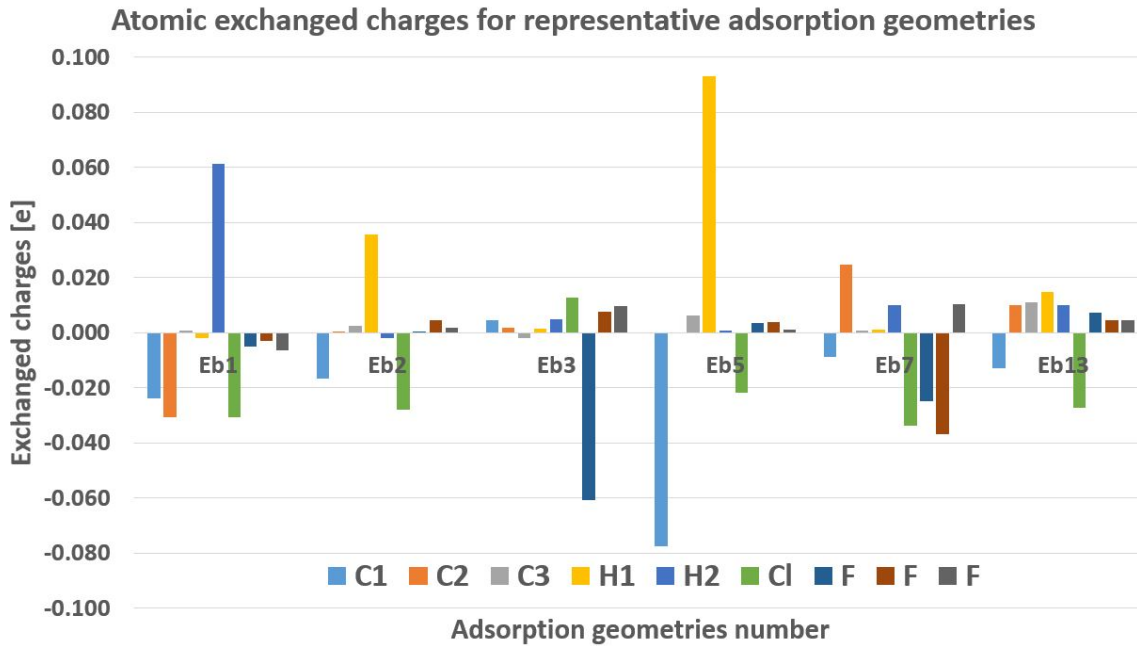
Figure II.3: Exchanged charges of R1233zd molecules with the surface during adsorption process. The distribution is represented for each refrigerant atom and theses charges are calculated in 6 representative cases, in reference to the ones in Table II.1.

- Case 1 (Eb13): In this adsorption geometry, R1233zd molecule takes around 0.02e from the surface. Carbon C1, the closer one of the surface, loses around 0.01e, the two other carbons takes 0.01e each. In this case, chlorine atom is close to the surface and loses around 0.03e. Even if the molecule takes 0.02e from the surface, atoms close to the surface (chlorine and carbon C1) lose both charges, meaning that this lose is spread all over the molecule. Indeed, the two other carbons C2 and C3, as well as hydrogen H1 et H2 gained around 0.01e each.

- Case 2 (Eb2): This case can be compared to case 1. Indeed, molecule tilts and hydrogen H1 gained around 0.035e, while Cl atom still loses around the same charge. Therefore, the total exchanged charge between R1233zd and the surface becomes negligible. This case is also interesting because it means that the high binding energy of around 0.5 eV is not due to exchange charges between R1233zd molecule and the surface.

- Case 3 (Eb5): R1233zd molecule gained almost 0.01e. Here, hydrogen H1 gains around 0.09e, not from the surface but from the carbon C1 which loses around 0.08e. This difference justify to look at the exchanged charges between all the atoms inside the molecule and not only between the molecule and the surface. Besides, chlorine atom still gives 0.02e to the surface.

- Case 4 (Eb7): This case represents a flat molecule on the surface. Here, R1233zd molecule loosed 0.057e. In contrast to what could be assumed, most of the exchanged charges are located in fluorine and chlorine atoms and not in the carbon-

carbon double bond area. While the two fluorine atoms near the surface lost around 0.04e and 0.025e each, the fluorine at the opposite gained only 0.01e. Chlorine atoms also lost around 0.034e. Only carbon C2 gained 0.025e, thus from fluorine or chlorine atoms. Furthermore, only for the two other optimized geometries (Eb6 and Eb8) within case 4, the same calculations were performed in order to obtain more accurately the charge distribution for a flat molecule upon the surface. In Eb6 and Eb8, only one fluorine atom is located near the surface and the two others are at higher distance. In these geometries, the lost of electron of CH$_3$ group is mainly supported only by the fluorine next to surface with a charge exchange of 0.05e for Eb6 and 0.07e for Eb8. Nevertheless, the same charges distribution than with Eb7 occurred.

- Case 5 (Eb1): R1233zd molecule gives a total of around 0.04e to surface. In this case, fluorine atoms play a negligible role, while chlorine lost around 0.03e. The two sp^2 atoms C1 and C2 lost 0.025e and 0.03e, respectively. At the same time, hydrogen H2 gained around 0.06e.

- Case 6 (Eb3): R1233zd molecule lost around 0.02e. Even if the fluorine atom next to surface lost around 0.06e, a part of this lost is spread through the molecule due to a gain in other atoms.

As a more general point of view, the values of total exchanged charges remains small and always lower than 0.1e in each case. Therefore, we assume that no chemisorption appears and that R1233zd are only physisorbed on hematite surfaces. In particular, due to these low exchanged charges relating to both carbons C1 and C2, we conclude that the double carbon-carbon bonds do not break during the adsorption process.

II.4   Conclusion

In this Chapter, the principles of DFT simulations were firstly presented and our model was introduced. Ab-initio calculations have been carried out in order to study the adsorption of R1233zd on an iron oxide Fe$_2$O$_3$ surface, complementing gaps from the experimental literature. The challenging point was to employ a vdW functional combined with a spin-polarized system by using the GGA+U method. The main findings can be summarized as follows:

- a range of surface-refrigerant molecule binding energy values of -0.92 eV to -0.22 eV is observed,

- the iron atoms play a major role in the adsorption process,

- the hydrogen H1 located near the chlorine plays a non-negligible role of stabiliza-

tion,

- the horizontal positions of the refrigerant molecules are the most stable with a binding energy value of around -0.92 eV,

- no dissociation phenomenon of the refrigerant on hematite was observed, nor double carbon-carbon bond breaking,

- between R1233zd molecule and surface only small exchanges of charge are found with a maximum value of 0.1e,

- R1233zd molecules are physisorbed on hematite $\alpha - Fe_2O_3(01\bar{1}2)$ surfaces and no chemisorption is observed.

Now that DFT calculations are completed, a parametrization of the interfacial force field will be performed. In the next chapter, the methods used to calculate the interfacial potential parameters are presented.

Chapter III

Towards large-scale molecular dynamics simulations

Contents

The results of this chapter have been partially published in the Journal of Physical Chemistry C [6].

III.1 Introduction to molecular dynamics

In molecular dynamics (MD), contrary to DFT, the interactions between atoms are described within force fields (FF) [23]. Since MD simulations are time-dependent, non-equilibrium phenomena can be explored and a large set of parameters regarding thin film shearing (friction, thermal conductivity, velocity profile, etc) can be obtained [24, 25, 26, 11, 27, 28, 29]. Therefore MD simulations are used in this project to characterize nanoconfined systems under shearing.

As shown in the previous Chapter, the high computational costs needed with DFT calculations preclude their use to study large systems. That is why, in this chapter, the principles of MD simulations used for larger scale systems, are presented. Then, the FF used for the refrigerant and the surface are described. Afterwards, the methodology used to parametrize a force field at the refrigerant-surface interface based on these DFT results is discussed. This FF is implemented in non-equilibrium molecular dynamics (NEMD) simulations in order to compare its predictions with the ones obtained using standard mixing rules. Specifically, the differences about structure and flow behavior in a system of refrigerant molecules confined between two hematite ($\alpha - Fe_2O_3$) surfaces are presented. Moreover, orientations of the molecules are calculated to illustrate this difference at the refrigerant/surface interface. Using this parametrized FF to study tribological behaviors at different extreme conditions will be the subject of Chapter 4.

III.1.1 Numerical methods

III.1.1.1 Molecular dynamics principles

Molecular Dynamics is a numerical method based on the resolution over the time of Newton's equation of motion on all interacting atoms in a molecular system [23]. The force $\mathbf{F}_i$ acting on each atom i located at a position $\mathbf{r}_i$ is obtained from the potential energy V:

$$\mathbf{F}_i = -\nabla_{\mathbf{r}_i} V \tag{III.1}$$

$$\ddot{\mathbf{r}}_i = \frac{\mathbf{F}_i}{m_i} \tag{III.2}$$

where m_i is the atomic mass. The potential energy V used to obtain forces describes the interactions of atom i with all neighboring atoms. The acceleration vector $\ddot{\mathbf{r}}_i$ can then be calculated.

III.1.1.2 Integration methods

MD simulations are time-dependent and the atomic trajectories are computed by solving equations of motion (Equation III.2). When atomic positions, velocities and accelerations are know at a time t, these features can be computed at the next time $t + \delta t$ with finite difference methods. δt is the timestep and the choice of its value influences the accuracy of the integration. A modified version of the standard Verlet algorithm is implemented in LAMMPS software, the Velocity-Verlet algorithm. The integration method of this algorithm is detailed below. First, the position at $t + \delta t$ is calculated with the following formula.

$$\mathbf{r}_i(t + \delta t) = \mathbf{r}_i(t) + \dot{\mathbf{r}}_i(t)\delta t + \frac{1}{2}\ddot{\mathbf{r}}_i(t)\delta t^2 \tag{III.3}$$

Then, the acceleration $\ddot{\mathbf{r}}_i(t + \delta t)$ is calculated from the interaction potential from the position $\mathbf{r}_i(t+\delta t)$. Finally, the velocity at $t+\delta t$ is determined with the following formula.

$$\dot{\mathbf{r}}_i(t + \delta t) = \dot{\mathbf{r}}_i(t) + \frac{1}{2}(\ddot{\mathbf{r}}_i(t) + \ddot{\mathbf{r}}_i(t + \delta t))\delta t \tag{III.4}$$

III.1.2 Force fields

III.1.2.1 Different kinds of force fields

Forces fields represent interactions between all particles as a function of their position in the system. FFs include both functional form of the potential energy representing these interactions and parameter sets used to calculate it. Several kinds of force fields exist in the literature.

Classical FFs can be divided into three types depending on different molecular structure considerations. "All-atom" (AA) FFs define every type of atom in the molecule, whereas "united-atom" (UA) FFs handle methyl (CH_3) and methylene (CH_2) groups as a single "pseudo-atom", leading to faster computational times. The UA model is particularly powerful to simulate the behavior of long-chain molecules, decreasing computation times. However, it can lead to unphysical properties, like under-prediction of the viscosity for long-chain linear alkanes[218]. Because R1233zd is a small molecule only containing nine atoms, classical AA force fields will be considered in all MD calculations. The third type

of classical FF is the coarse-grained (CG) model, where groups of atoms are replaced by pseudo-atoms at a larger scale. This last type increases even more the computational efficiency by reducing the number of degrees of freedom. CG models are widely used for long time simulations to model biomolecules, like proteins[219, 220].

The literature also proposes reactive force fields (ReaxFF), which consider chemical reactivity and determine possible breaking and new bonds between pairs of atoms during MD simulations[221]. In this project, we tried to use this force field. However, despite several exchanges with the reaxFF authors, we did not succeed to adjust the FF parameters to obtain an accurate description of the refrigerant. Hence, reaxFF will not be considered here.

HFO compounds have been in the market for only a few years and therefore experimental data for these molecules are rare[100, 222]. That is why Raabe et al. [32] recently developed a force field in order to study this kind of refrigerants. This FF will be named Raabe's FF in the following chapters. As detailed later in this chapter, parameters sets of this FF are obtained from both quantum calculations or by fitting experimental data.

III.1.2.2 Classical force fields formulation

Usually, the functional form of the potential energy is divided into two contributions, as shown in the formula below [23]. Bonded (or intramolecular) terms represent interactions between atoms that are linked by covalent bonds. Non-bonded (or intermolecular) terms describe interactions between atoms which are not linked with covalent bond.

$$V_{\text{total}} = V_{\text{bonded}} + V_{\text{non-bonded}} \tag{III.5}$$

The bonded and non-bonded terms considered in the present model are detailed here.

Non-bonded interactions

$$V_{\text{non-bonded}} = V_{\text{Coulomb}} + V_{\text{LJ}} \tag{III.6}$$

In classical force field, non-bonded terms represent Pauli repulsive and Van der Waals attractive forces, grouped in the so-called Lennard-Jones potential, but also Coulomb electrostatic interactions. Therefore, two different potentials have to be used.

Lennard-Jones: The following formula represents the Lennard-Jones 12-6 potential between each atom pair i and j, only applied if the distance between two atoms is lower than a cutoff distance.

$$V_{\text{LJ}}(r_{ij}) = 4\varepsilon_{ij} \left(\left(\frac{\sigma_{ij}}{r_{ij}} \right)^{12} - \left(\frac{\sigma_{ij}}{r_{ij}} \right)^{6} \right) \tag{III.7}$$

Where r_{ij} is the distance between two atoms' nuclei. The ε_{ij} energy corresponds to the depth of the potential well and σ_{ij} the distance corresponding to a zero value of the potential between both atoms. The equilibrium distance between both atoms is given by $2^{1/6}\sigma_{ij}$. The denomination 12-6 comes from the power in LJ terms, where the first term (to the power 12) represents the repulsive feature while the second term (to the power 6) represents the attractive one.

Values of the parameters σ_i and ε_i are affected to each atom i. Lorentz-Berthelot mixing rules are applied to obtain LJ parameters with two atoms i and j of different natures, as follows.

$$\begin{cases} \varepsilon_{ij} = \sqrt{\varepsilon_i \varepsilon_j} \\ \sigma_{ij} = \dfrac{\sigma_i + \sigma_j}{2} \end{cases} \tag{III.8}$$

Buckingham, another option: Sometimes, the Buckingham potential is used instead of the Lennard-Jones one. As shown in the following formula, the repulsive term is then modeled with an exponential while the attractive term has the same form as the Lennard-Jones one.

$$V_{\text{Buckingham}}(r_{ij}) = \left(A e^{-\frac{r_{ij}}{\rho}} - \frac{C}{r_{ij}^6} \right) \tag{III.9}$$

Coulombic potential: In order to represent partially charged atoms, electrostatic interactions have to be considered. They are calculated between two charged atoms, either belonging to the same molecule or not, thanks to a long-range Coulombic potential, as shown below:

$$V_{\text{Coulomb}}(r_{ij}) = \frac{q_i q_j}{4\pi\varepsilon_0 r_{ij}} \tag{III.10}$$

where q_i and q_j are the atomic charges of atoms i and j, respectively, r_{ij} is the distance between the two atoms, and ε_0 the vacuum permittivity equal to $8.85 \times 10^{-12}\,\text{F/m}$.

As shown in Equation III.10, Coulombic interactions decrease as $\frac{1}{r}$, whereas Van der Waals attractive interactions decrease as $\frac{1}{r^6}$. Hence, electrostatic interactions can remain non-negligible at long-range, and thus, have to be considered even farther than the cutoff value. For distances bigger than the cutoff value, electrostatic interactions can be determined using the particle-particle particle-mesh (PPPM) algorithm[223]. Indeed,

with periodic boundary conditions, it is not possible to compute the interactions with the infinite number of atoms in periodic images of the simulation cell. The charges are assigned to a 3d mesh and the Fast Fourier Transform is used to solve Poisson's equation for the electrostatic potential. Then, after calculation of the potential at each mesh point, the force of each particle is determined from the mesh field by interpolation.[23].

Bonded interactions:

In most force fields, bonded interactions between atoms belonging to the same molecule are modeled with harmonic springs. To describe all the degrees of freedom and the flexibility of the molecule, bonded interactions are divided into three independent terms called bonds stretching, angles bending and dihedrals (describing torsion). Figure III.1 is a schematic representation of bonded interactions.
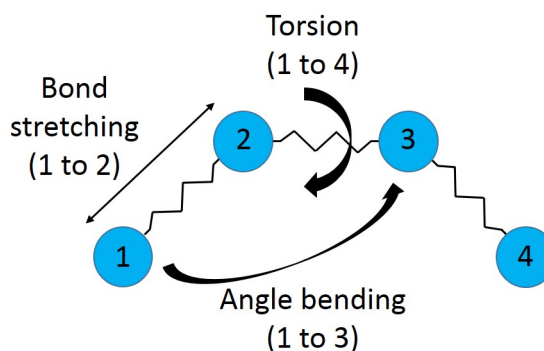
Figure III.1: Schematic representation of bonded interactions.

$$V_{\text{bonded}} = V_{\text{bond}} + V_{\text{angle}} + V_{\text{dihedral}} \tag{III.11}$$

Bond stretching: The covalent bond between two atoms (1 to 2 in Figure III.1) is modeled with an harmonic spring, enabling compression and extension. The following formula is used:

$$V_{\text{bond}} = K_b(r - r_0)^2 \tag{III.12}$$

With K_b the bond stiffness, r the distance between two atoms and r_0 the equilibrium distance.

Angle bending: The bending features obtained with a triplet of atoms (1 to 3 in Figure III.1) are also represented with a harmonic spring as shown in Equation III.13.

$$V_{\text{angle}} = K_\theta(\theta - \theta_0)^2 \tag{III.13}$$

75

With K_θ the angle stiffness and θ_0 the equilibrium angle.

In this work, for both bond stretching and angle bending terms, the stiffness constant comprises the classic $\frac{1}{2}$ factor coming from Hooke's law.

Dihedral torsion: Torsion between four atoms (1 to 4 in Figure III.1) belonging to the same molecule is represented by a dihedral potential as in Equation III.14:

$$V_{\text{torsion}} = \sum_{i=1}^{m} K_i[1 + cos(n_i\phi - d_i)] \tag{III.14}$$

where n is the multiplicity and d the phase. To improve the accuracy of the dihedral term to reproduce torsional behavior, the torsion can be described by a sum of m dihedral terms.

Non-bonded interactions scaling:

It is usual to exclude or to just include partially (using scaling factors) non-bonded terms between two atoms in the same molecule bonded with covalent bond, either directly or via one or two intermediate bonds. Indeed, bonded interactions are usually designed to describe the whole set of interactions between bonded atoms, including Pauli repulsive, VdW attractive and electrostatic terms. By keeping non-bonded interactions between these atoms, they would thus be counted twice.

For example, the Raabe's FF used in this study to describe the R1233zd interactions, involves scaling factors from the AMBER FF. In this latter, non-bonded LJ and electrostatic interactions between atoms separated by exactly three bonds (1 to 4 interactions) are scaled by a factor of 1/2 and 1/1.2, respectively. Non-bonded interactions between atoms separated by one or two bonds are excluded.

III.1.3   Importance of the force field for nanoconfined systems

The interactions between every atoms control the accuracy of materials behavior description. These interactions are described in the FF. The FF parameter sets will strongly influence properties of the system. Hence, the parameters have to be carefully chosen in order to provide realistic results. As shown in the next section, the FF parameter sets used for the refrigerant have been tested in the literature by comparing with experimental features. Two main issues come by applying FF in nanoconfined systems.

First, a force field is usually developed in a limited range of environmental conditions. As shown previously, a key point in lubricated systems is that conditions are extremes regarding temperature, pressure and shearing states. Indeed, a FF parameter set established for a pressure as small as a few MPa will not necessarily reflects correctly the

behavior of the same molecule at high pressure such as a few GPa.

The second point which is often not discussed in MD simulations is the interfacial parameter sets used between two phases of different materials, such as a solid surface and a fluid. The non-bonded interactions can be modeled with Coulombic and Lennard-Jones potentials. The FFs are rarely developed to represent a system with both fluid and solid surface together, but rather the parameter sets are obtained for fluid and surface separately, from different studies. As shown in the previous section, between the surface and the fluid molecules, the LJ parameters can be obtained thanks to the Lorentz-Berthelot mixing rules. However, no guarantee can be given that the interfacial reactivity will be correctly represented, just because both bulk fluid and surface FF were not initially developed to do so. Therefore, the interfacial force fields at the interface between R1233zd molecules and hematite $\alpha - Fe_2O_3$ surfaces will be discussed.

In the next section, our model used for R1233zd and hematite surface is described. Moreover, the methodology and results about parametrization of the interfacial force field are provided.

III.2 Parametrization of interfacial force field

III.2.1 R1233zd force field

HFO compounds have been in the market for only a few years and therefore experimental data for these molecules are rare[100, 222]. That is why Raabe et al. developed a force field in order to study this kind of refrigerant [32]. In 2015 an extension of this force field was published for the R1233zd refrigerant in order to study its thermophysical properties [31]. This FF has been designed by fitting experimental data from the literature for LJ parameters and by using ab-initio simulations for bonded terms and partial charges [31]. In this work, we will use this empirical FF to represent the bulk refrigerant behavior. This FF has shown a good reproduction ability of vapor-liquid equilibrium properties from 273 K to 383 K, at a few MPa [31]. Bonds, angles, dihedrals and non-bonded LJ parameters of this FF can be found in Table III.1.

The partial charges of each atoms used for Coulombic potential are gathered in Table III.2.

Thermophysical properties, such as vapor pressure, liquid density and heat of vaporization, have been determined by Raabe [31]. In particular, a boiling point of 290.9 K at atmospheric pressure has been calculated with this FF, to compare with the experimental reference value of around 292 K, as detailed in Chapter 1.

Interactions (All Atoms)	Type	Coefficients		
Bond		$K_b \left[kcal.mol^{-1}.\text{Å}^{-2}\right]$	$l_0 \left[\text{Å}\right]$	
$V_{bond} = K_b (r - r_0)^2$	Cm-H1	388.62	1.086	
	Cm-Cl	227.80	1.734	
	Cm-Cm	676.34	1.331	
	Cm-Ct	317.39	1.511	
	Cm-H2	388.62	1.086	
	Ct-F	371.31	1.353	
		$K_\theta \left[kcal.mol^{-1}.rad^{-2}\right]$	$\theta_0 \left[deg\right]$	
Angle	H2-Cm-Cm	36.33	120.6	
	H2-Cm-Ct	32.31	115.1	
$V_{angle} = K_\theta (\theta - \theta_0)^2$	H1-Cm-Cm	36.33	120.6	
	F-Ct-F	87.80	107.5	
	Cm-Ct-F	74.80	111.3	
	H1-Cm-Cl	36.45	113.8	
	Cl-Cm-Cm	67.07	122.95	
	Cm-Cm-Ct	50.09	124.1	
Torsion		$K_{tor} \left[kcal.mol^{-1}\right]$	n	$d \left[deg\right]$
	Cl-Cm-Cm-H2	6.65	1	180
$V_{tor} = K_{tor}[1 + \cos(n\phi - d)]$	Cl-Cm-Cm-Ct	6.65	1	0
	H1-Cm-Cm-H2	6.65	1	0
	H1-Cm-Cm-Ct	6.65	1	180
	Cm-Cm-Ct-F	0.1421	3	0
	H2-Cm-Ct-F	0.178	3	0
Non-bonded LJ		$\varepsilon \left[kcal.mol^{-1}\right]$	$\sigma \left[\text{Å}\right]$	
	Cm	0.09793	3.40	
$V_{LJ} = 4\varepsilon \left[\left(\frac{\sigma}{r}\right)^{12} - \left(\frac{\sigma}{r}\right)^6 \right]$	Ct	0.07426	3.40	
	H1	0.01569	2.47	
	H2	0.01569	2.65	
	Cl	0.26214	3.55	
	F	0.05641	2.94	

Table III.1: Bonds, angles, dihedrals and non-bonded LJ parameters for R1233zd, obtained from Raabe's FF [32, 31].

Partial Charges q [e]	
C1	-0.001
C2	-0.307
C3	0.781
H1	0.171
H2	0.196
Cl	-0.094
F	-0.249
F	-0.249
F	-0.249
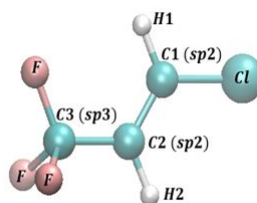
Table III.2: Partial charges of atoms within the R1233zd molecule. [31].

78

III.2.2 Force field of the hematite ($\alpha - Fe_2O_3$) surface

As shown in Figure III.2, the size of an elementary cell of hematite ($\alpha - Fe_2O_3$) surface considered in this chapter is 30 Å × 33 Å × 10 Å.
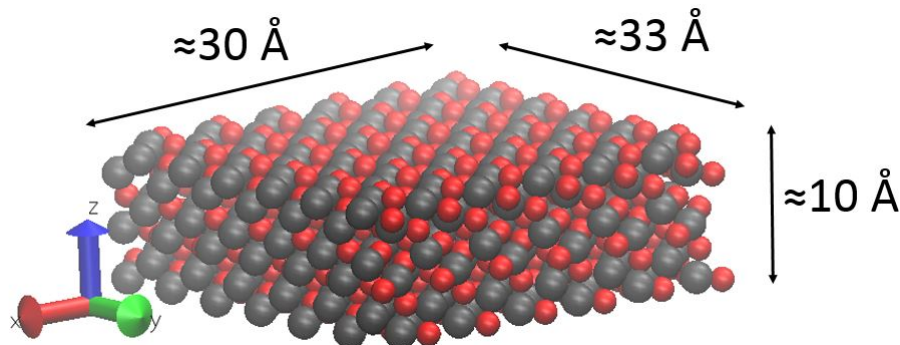
Figure III.2: Hematite ($\alpha - Fe_2O_3$) surface of around 30 Å × 33 Å × 10 Å.

In this MD study, the hematite surface built by using ab-initio calculations (Chapter 2) was duplicated considering periodic boundaries. Moreover, the surface used in Chapter 2 to obtain results of adsorption has to be considered in MD simulations with exactly the same structure and lattice parameters. Instead of using a FF of the literature that would, in best case, approximately reproduce the lattice parameters, each atom of the hematite surface is bonded with a spring to a virtual atom located at its equilibrium position [224]. At zero temperature, a virtual surface will thus be superimposed with a real one. No interaction are defined within the virtual surface, between the two virtual surfaces, and between the virtual surfaces and the refrigerant. The only interactions between virtual and real surfaces are the springs linking one virtual atom with one real atom. However, it will have several consequences, as detailed below.

On the one hand, one can not study the surface deformation with this method. Indeed, the virtual atoms involve an infinite stiffness and no plasticity. Nevertheless, it is not the aim here to study the surface. In this work, the interest lies on the refrigerant and the refrigerant/surface behavior. The surface by itself, with only a few atoms in the thickness, can not have both a quantitative elastic and thermal behavior and compromises have to be found [161]. Here we chose to focus on ensuring a good thermal conduction (i.e., much larger than that of the fluid) to the walls.

One the other hand, the value of spring stiffness applied between one real and one virtual atoms has to be carefully chosen. Indeed, this value influences both mechanical and thermal features.

- The bond between real and virtual atoms must be stiff enough to prevent any incursion of fluid atoms inside the surface. This property was qualitatively investigated by testing different values of spring stiffness.

- Reproducing exactly the thermal conductivity of hematite surface is not the aim here. The surface has to evacuate the heat created within the contact. With that regard, the higher the spring stiffness, the higher the thermal conductivity is.

- However, by increasing the spring stiffness values, the period of atomic vibrations decreases, requiring a smaller timestep to resolve the vibrations. While large bond stiffness seemed preferable for the two preceding aspects, this one imposes an upper limit on the bond stiffness.

Figure III.3 represents the temperature distribution in hematite surface with different spring stiffness value of 200, 300 and 400 kcal/mol at two sliding velocity of 20 m/s (left) and 10 m/s (right).
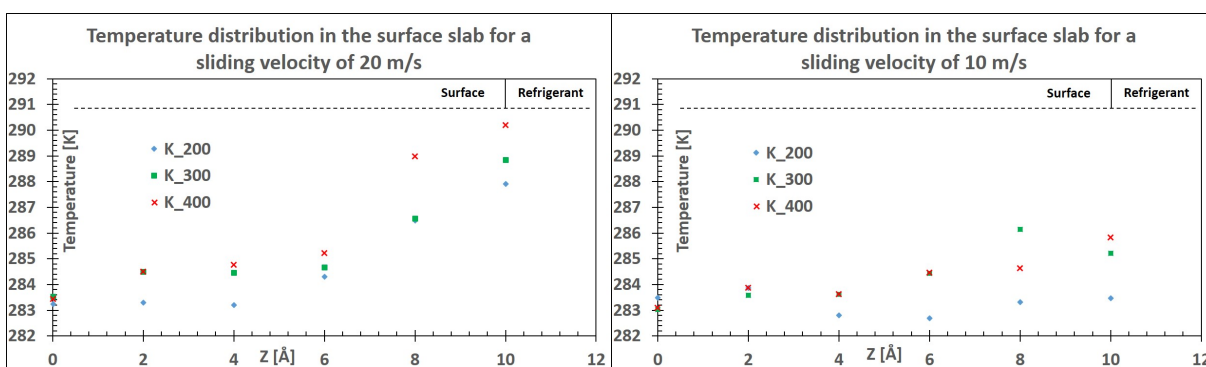
Figure III.3: Temperature distribution in the hematite slab for a sliding velocity of 20 m/s (left) and 10 m/s (right). The results are obtained with three different values of real-virtual spring stiffness of 200, 300 and 400 kcal/mol.

As detailed in the simulation setup in the next section, only the two third outermost layers of atoms in the hematite slabs are thermostatted (here at 283 K). A value of 200 kcal/mol is chosen for this study. Indeed, the surface remains rigid enough from a qualitative view and a temperature gradient in the surfaces up to 5 K over 3 angstroms is found. This latter value is higher than in reality, but the heat produced by the shearing of the lubricant can still be evacuated through the surface by the thermostat.

The pressure in the contact and the shearing velocities are obtained by applying forces and velocity on each atom of the virtual surfaces, while the temperature is regulated through the real surface atoms.

The next section aims at analyzing the influence of the timestep, to justify the last of the three listed points above.

III.2.3 Influence of the timestep

A timestep of 1 fs is a standard value used in many studies of MD simulations for nanoconfined lubricants [178, 225, 226, 29]. However in this system, it is possible that

this value is too large because of fast-moving hydrogen atoms. One can calculate the period τ of the fastest vibrating atoms in the system with the following formula.

$$\tau = 2\pi\sqrt{\frac{m}{k}} \qquad (III.15)$$

Where m is the mass of hydrogen atoms, and k is the higher spring stiffness coefficient involving a hydrogen atom. In Raabe's FF, both kinds of bond linking hydrogen to carbon atoms (C1-H1 and C2-H2) have the same stiffness constant value, thus $\frac{k}{2} = 388.62\,\text{kcal/(mol.Å}^2)$. The calculation gives a period τ of around 11 fs, thus around 10 times higher than a timestep δt of 1 fs, validating the choice made in this study.

As described above, in NVE ensemble, the total energy should be constant. However in MD simulation, the total energy of a system in NVE ensemble can fluctuate on a short time scale and drift on a long time scale for Verlet intergrator [227], as shown in Figure III.4. In order to verify that the drift is acceptable with this system and a timestep of 1 fs, a pure NVE calculation, thus without any temperature or pressure, is done. The system is composed of 1000 molecules of refrigerant. The results shown in Figure III.4 represents the total energy variation as a function of the time.
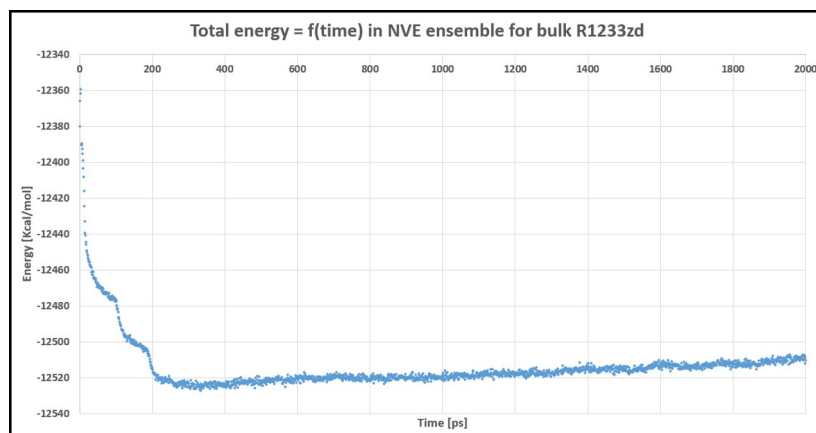
Figure III.4: Energy drift of the total energy over time for bulk simulations with 1000 molecules of R1233zd.

The system stabilizes during around 500 ps and then we observe the energy drift, which has a value of $4,5.10^{-5}$ eV/atom over 1 ns, on the order of 0.1 % of the average kinetic energy per atom. This negligible energy drift confirms that a timestep of 1 fs is low enough to ensure well designed simulations.

In this section was exposed FFs used for R1233zd and hematite surfaces, separately. However and as explained above, one can not have the insurance that the interfacial FF obtained with mixing rules reproduces accurately the real behavior. Therefore, a parametrized FF is calculated using the ab-initio results.

III.2.4 Parametrization of interfacial force field between R1233zd and hematite surfaces

III.2.4.1 Methodology

In Chapter 2, the adsorption ability of R1233zd on hematite was studied. An adapted force field of the interface between the refrigerant and the surface will be derived from this ab-initio behavior. In this section the ab-initio post processing is described and the force field parameters used at the interface for large scale MD simulations are determined. Even if periodic boundary condition (PBC) are used for all MD simulations, no PBC is used for the parametrization, and therefore a larger surface than the one presented in Chapter 2 has to be considered. Indeed, electrostatic interactions have to be included with a large amount of pairs between the surface and the refrigerant molecule. By using the periodicity of the small surface composed of 120 atoms, a new bigger one was built, multiplying the smaller one by three in the x and y directions. Hence, the new surface used for ab-initio post processing is composed of 1080 atoms, and the molecule of refrigerant is placed upon the central small surface with the position obtained at the end of ab-initio geometry optimization process. In this study 16 different positions and orientations of the refrigerant molecule on the surface are used and an algorithm detailed in Figure III.5 is performed to determine the interfacial parameters.

With a similar problematic, Ta et al.[10] studied the adsorption of n-alkanes on various kinds of iron oxide surfaces. They used a trial-and-error approach in order to adjust the force field parameters to the DFT results. They ran the adsorption energy calculations repeatedly until they obtained a good match between ab-initio and MD results. They also published an interfacial FF between an aqueous copolymer solution and an iron surface, by deriving parameters from DFT calculations[228].

Here, the choice was made to transcript the refrigerant-surface interactions by using pairwise Coulombic and Lennard-Jones (LJ) 12-6 potentials between each atom pair i and j. Equation III.16 represents the model we used for the interfacial interactions.

$$V = \sum_{i,j} \left[\frac{q_i q_j e^2}{4\pi\varepsilon_0 r_{ij}} + 4\varepsilon_{ij} \left(\left(\frac{\sigma_{ij}}{r_{ij}}\right)^{12} - \left(\frac{\sigma_{ij}}{r_{ij}}\right)^{6} \right) \right] \qquad (III.16)$$

Where q_i and q_j are atomic charges of atoms i and j, respectively, r_{ij} the distance between atoms i and j, ε_{ij} the well-depth energy and σ_{ij} the distance corresponding to a zero value of the potential between the two atoms. To remain consistent by using the Raabe's FF for the refrigerant with large-scale MD calculations, the partial charges of Raabe[31] will be used for the ab-initio postprocessing and only the 12-6 LJ parameters between the fluid and the surface will be adjusted. For hematite surface, the partial

charge of iron is fixed of $q_{Fe} = +0.6$ and that of oxygen to $q_O = -0.4$. Because LJ parameters have to be distinguished depending on atom types, sp^2 and sp^3 carbons are named Cm and Ct, respectively.

The idea of this postprocessing is explained in this paragraph, to read with the help of Figure III.5. From ab-initio results, it is possible to find four (k=4,12,13,14 in Figure III.5) converged geometries related to DFT case 1 (see Table II.1) in which the chlorine atom is directly placed upon the iron and oxygen atoms. Therefore these four results are used in order to find in step 1 (i=1 in Figure III.5) the interactions between chlorine and the surface. Then four other converged geometries (k=2,10,11,16) describing a molecule adsorbed thanks to chlorine and hydrogen H1 are used within steps i=2 and i=3 in order to obtain the interactions between this hydrogen and the surface. Afterwards the parameters between fluorine and the surface are found within steps 4 and 5. Then the interactions parameters between the hydrogen H2 and the surface are found by using four optimized geometries in steps 6 and 7. In order to reproduce the binding energies obtained with horizontal positions of the molecule, ε values between surface and the Ct carbon are adapted as well within steps 8 and 9.

The mathematical approach will now be detailed. Analyzing situations where R1233zd molecules adsorbed at least partially either with O-Cl or with Fe-Cl interactions, $\sigma_{(Fe-Cl)}$ and $\sigma_{(O-Cl)}$ are fixed to 2.46 Å and 2.53 Å, respectively, on the basis of adsorption distances obtained from ab-initio calculations. Moreover, σ values for interactions including carbons remain fixed as explained below. The values of ε for LJ potential including sp^3 carbon will be adapted to take into account the strong interactions obtained between fluorine atoms and the surface. The ε values for LJ potential including sp^2 carbon will be fixed.

Sixteen unknown LJ parameters remain to be determined. The resolution of the global system of 16 equations with 16 unknown parameters is difficult, so that the solving process is split into 9 steps. At every step, only a limited number k of the 16 optimized geometries is taken into account by choosing the geometries for being relevant to the parameters calculated in this step. For each of the k corresponding equations, we calculate each distance between the 9 atoms of the molecule and the 1080 atoms of the surface. A system composed of k nonlinear equations named f_k with an amount of unknown LJ parameters smaller than k is obtained. Eb_k is the binding energy associated to the geometry optimization number k, while r_{kij} represents the distance between both atoms i and j for this geometry k. The vector x is composed of the 16 LJ-parameters including the unknowns, the ones determined on previous steps, and the ones initially fixed as detailed below, which will be calculated on next steps. By using a trust-region reflective method we solve the following least squares problem for each step and we find the x vector minimizing the following sum:
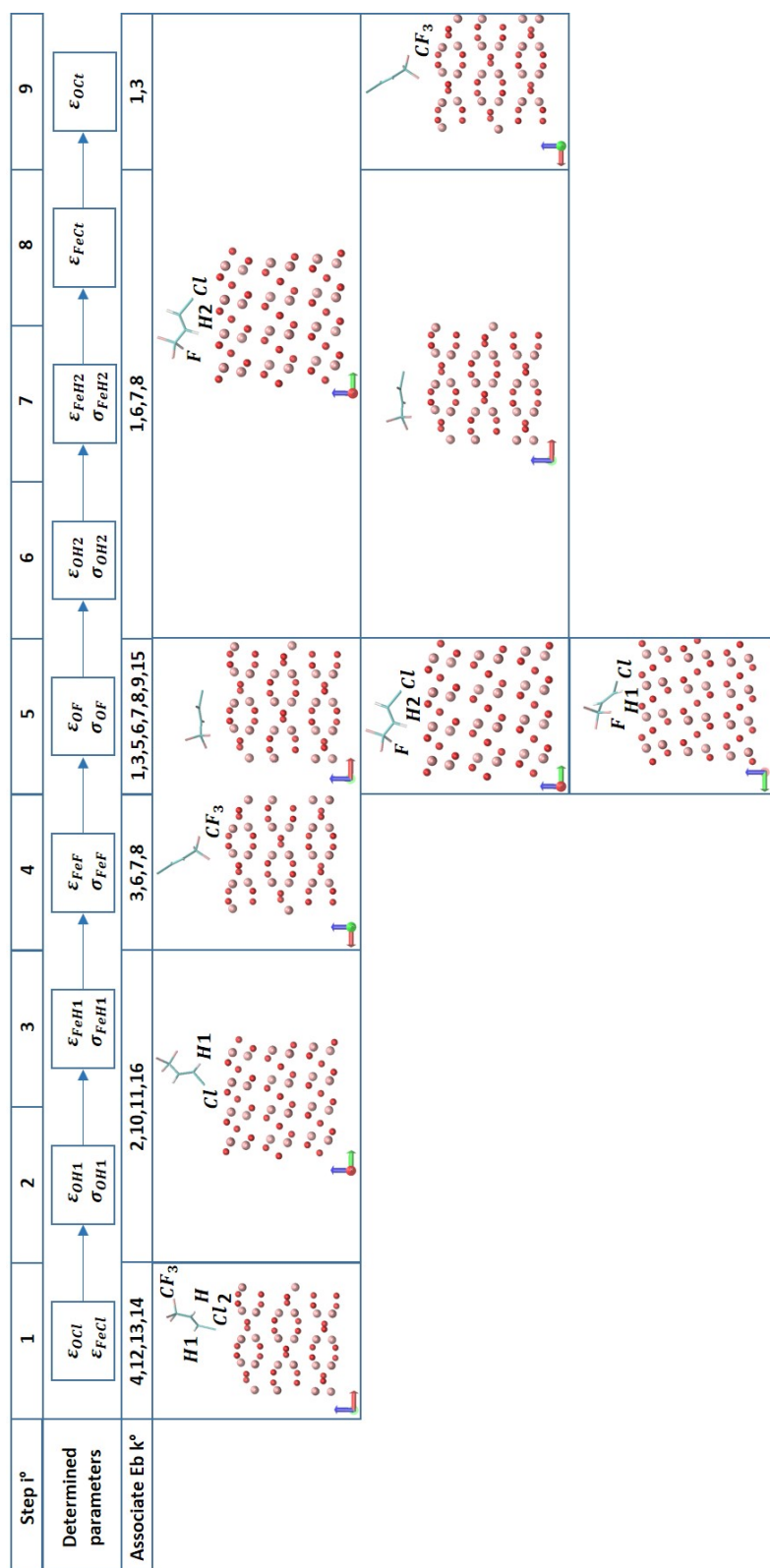
Figure III.5: Postprocess algorithm in order to obtain LJ 12-6 parameters between R1233zd molecule and hematite surface.

$$\min_x \left(\sum_k (f_k(x))^2 \right) \qquad (III.17)$$

with

$$f_k = Eb_k - \sum_{i,j} \left[\frac{q_i q_j e^2}{4\pi\varepsilon_0 r_{ij}} + 4\varepsilon_{ij} \left(\left(\frac{\sigma_{ij}}{r_{ij}} \right)^{12} - \left(\frac{\sigma_{ij}}{r_{ij}} \right)^6 \right) \right]. \qquad (III.18)$$

Because of physical considerations, for each postprocessing step, both initial points and boundary conditions for the solutions are fixed between 1 Å and 5 Å for every σ value. Concerning the values of ε, they must be positive and lower than 1 eV. Indeed the maximum value of binding energy obtained with ab-initio calculations remains lower than 1 eV for the whole set of position possibilities and thus the energy represented by ε between only two atoms cannot exceed this value. For each step of this process numbered from 1 to 9, 100 initial points are randomly chosen within the bounds specified above. The LJ parameters still not obtained at the step i, are fixed by using the Lorentz-Berthelot mixing rules (see Equation III.8). As discussed previously, Raabe's FF parameters [32, 31] are used for the refrigerant molecule and the consistent valence force field (CvFF) is used for iron and oxygen atoms[229, 230, 231].

III.2.4.2   Results and analysis

The results obtained for the parametrization of the interfacial FF are summarized in Table III.3

pairwise	ε_{ij} kcal/mol	σ_{ij} Å
O-Cm	0.149	3.13
O-Ct	0.196	3.13
Fe-Cm	1.090	2.86
Fe-Ct	0.479	2.86
O-H1	0.408	2.34
O-H2	0	1.00
O-Cl	0.618	2.53
O-F	0.174	2.95
Fe-H1	0.068	3.70
Fe-H2	0	1.00
Fe-Cl	1.147	2.46
Fe-F	0.740	1.97

Table III.3: LJ 12-6 parameters for the interactions between hematite surface and R1233zd.

Iron atoms play a major role in the adsorption process with strong ε values of Fe-Cl and Fe-F pairs. Moreover, the strong interaction observed for horizontal orientation is described with a high ε value between iron and sp^2-hybridized carbon atoms. The hydrogen H2 bonded to the second carbon is well described by zero well-depth energy values with both oxygen and iron. The binding energy values obtained with this optimized interfacial force field are compared with the ones determined from ab-initio calculations. The results summarized in Table III.4 show a maximal difference of 54 meV, and a maximum relative difference of around 10 %. Overall, the new LJ 12-6 parameters reproduce quite well the ab initio results.

N°	Energy of adsorption [eV]		Relative difference [%]	Absolute difference [meV]
	MD with modified FF	ab-initio		
Eads1	-0.728	-0.696	4.56	32
Eads2	-0.507	-0.521	2.63	14
Eads3	-0.421	-0.468	10.06	47
Eads4	-0.376	-0.393	4.21	17
Eads5	-0.680	-0.663	2.48	16
Eads6	-0.903	-0.874	3.29	29
Eads7	-0.869	-0.922	5.83	54
Eads8	-0.840	-0.825	1.71	14
Eads9	-0.649	-0.639	1.54	10
Eads10	-0.487	-0.507	4.00	20
Eads11	-0.530	-0.551	3.80	21
Eads12	-0.361	-0.343	5.26	18
Eads13	-0.479	-0.446	7.55	34
Eads14	-0.219	-0.224	2.24	5.0
Eads15	-0.629	-0.649	3.08	20
Eads16	-0.534	-0.572	6.59	38

Table III.4: Comparison between binding energies obtained with the optimized force field and the ab-initio ones for every system geometry.

The optimized interfacial force field will be used in larger scale MD simulations; the simulations setup and results concerning this following step are presented in the next subsection.

III.3   Assessment of the new parametrized force field: comparison with standard mixing rules

III.3.1   System setup

MD calculations in this section are performed by using the LAMMPS software (version: May 14th 2016)[30]. (01$\bar{1}$2) slabs of hematite with *(x,y,z)* dimensions of around 30 Å ×

33 Å × 10 Å are used in all simulations. The upper surface is built by rotating the lower surface by 180°. Each surface is composed of 1080 atoms (excluding virtual atoms).

The liquid is made of 192 refrigerant molecules, thus 1728 atoms. Raabe's FF introduced in the previous section is used to represent the refrgierant in a bulk behavior [31, 32]. The Lorentz-Berthelot mixing rules are applied to determine LJ parameters between different atoms in the bulk refrigerant (Equation III.8). Surface-refrigerant interactions are represented with LJ and Coulomb potentials. LJ parameters obtained with the postprocessing and partial charges exposed in the previous section are implemented. No LJ interaction are considered within the surfaces.

The Verlet integration algorithm is used with a 1 fs time step. The non-bonded interactions are represented by the LJ 12-6 potential coupled with the long-range Coulombic interactions including a cutoff value of 12 Å for both non-bonded kinds of interactions. Intramolecular nonbonded interactions between atoms separated by one or two bonds are set to zero. Scaling factors of 1/2 and 1/1.2 from the AMBER FF are applied to nonbonded LJ and electrostatic interactions respectively, between atoms separated by exactly three bonds. Electrostatic interactions were determined using the particle-particle particle-mesh (PPPM) algorithm. A slab correction is used for the PPPM solver because of the non-periodic system in z direction [232].

III.3.2   Temperature-pressure regulation and initialization stages

Each simulation is linked to a statistical ensemble. In the NVE ensemble, the number of atoms, the volume and the total energy, which is the total of the potential and kinetic energies, is fixed. In the NPT ensemble, the number of atoms is fixed, the pressure is controlled by a barostat (which affects the volume), and the temperature is controlled by a thermostat (which affects the energy). The thermostat is particularly important in NEMD to remove the heat generated by viscous dissipation from the system.

First of all, depending on the initial distance between each molecules, a minimization of the potential energy can be needed to avoid too large interactions between molecules at the beginning of the simulation. During MD simulations, the pressure and temperature can be regulated through different methods depending on the kind of simulation and system considered.

In NEMD, although the system is not at an equilibrium state, a steady state is required for averaging over time the studied quantities. Therefore an initialization stage is needed after the minimization. The initialization stage contains first a compression stage where a normal load is applied. At the same time, a thermostat is applied to a temperature-control region in order to keep the surface at a desired temperature during all the MD calculations. At the end of the compression stage, the thickness of the film separating

the surfaces is fluctuating around a constant value. During the second (sliding) stage of initialization, the normal load remains and velocity is applied in a velocity-control region, which is often the same as the pressure-control one.

III.3.3 Simulations setup: compression and shearing

All initial systems are created with the Moltemplate software[33]. An initial vacuum gap of around 30 Å in the z direction between refrigerant molecules and the surface is set up, in order not to disrupt energy minimization and refrigerant bulk stabilization before applying the normal load. The pressure $P_z = 500\,\text{MPa}$ is controlled by applying an additional external force to the virtual surface in such a way that every virtual atom experiences the same force, so that the virtual surface moves rigidly. After the compression stage, a velocity of $v_x = \pm\frac{v_s}{2}$ is implemented in the x direction for all virtual atoms with a shearing velocity value v_s of 20 m/s, while the normal load remains fixed. A Langevin thermostat with a damping time of 0.1 ps is applied to the two third outermost layers of atoms in the hematite slabs, in order to keep them at a temperature of 283 K during all the MD calculations. Indeed, it was shown that direct thermostatting of the confined fluid can lead to unrealistic properties [35]. During the sliding stage, the Langevin thermostat is applied to both hematite surfaces but only perpendicularly to sliding and compression directions, thus only in y direction[34]. Figure III.6 is a representation of an R1233zd fluid confined between two hematite surfaces where mechanical conditions, as well as thermostats, are outlined. The shearing step lasted for 10 ns and results are averaged upon the last 2 ns for the velocity and density profiles.
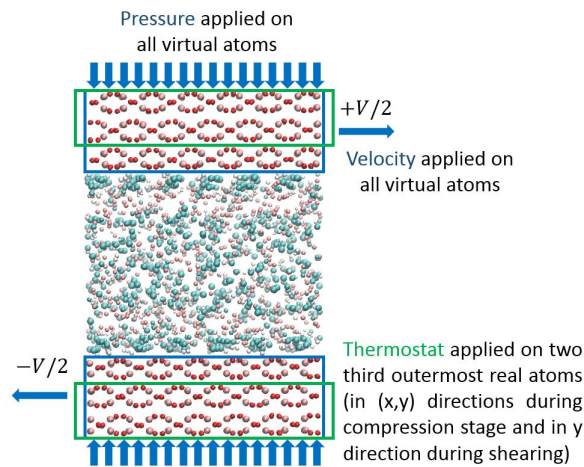
Figure III.6: Representative system setup for the NEMD simulations of R1233zd confined between two hematite surfaces.

III.3.4   Consequences of interfacial FF parametrization

This section aims at highlighting the differences and similarities of using the parametrized FF or the standard FF obtained with Lorentz-Berthelot mixing rules associated with Raabe's FF [31, 32] and the consistent valence force field (CvFF)[229, 230, 231] for the solid/liquid interface. Both structure and dynamics of R1233zd confined between two hematite surfaces are explored in this section. Moreover, orientation of the refrigerants molecules at the interface is studied.

III.3.4.1   Velocity profiles

Figure III.7 shows the velocity profiles of R1233zd and hematite surfaces with both standard FF and parametrized FF.
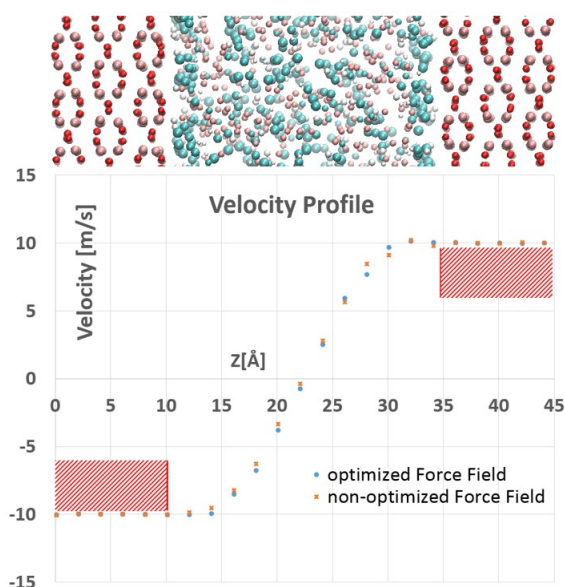
Figure III.7: Flow velocity profile with $P_z = 500\,\mathrm{MPa}$, $v_x = \pm 10\,\mathrm{m/s}$ and wall temperature $T = 283\,\mathrm{K}$. Blue points represent the velocity profile in the x direction with the optimized FF and the orange crosses with the non-optimized FF. Each point is an average over a 2 Å thick layer in z direction. The red crossed lines indicate the position of the surfaces.

R1233zd molecules close to the surface are locked with the two FFs. It means that effective shearing will occur within a smaller film thickness than without locking effect. This latter is reminiscent of experimental observations made by Morales-Espejel et al. and detailed in Chapter 1 about formation of a thick solid layer on the steel ball surface[3]. The layer observed here resists under high pressure (500 MPa) and high shearing with $v_x = \pm 10\,\mathrm{m/s}$. It could protect the bearing surfaces against wear when two asperities are close, what was firstly assumed by Morales-Espejel et al[3]. The velocity profile does not vary much by using either the optimized FF or the non-optimized one. However, as shown in the following section, the density profiles are affected.

III.3.4.2   Density profiles

Figure III.8 compares density profiles obtained using the classical interfacial FF (a) and the optimized FF (b).
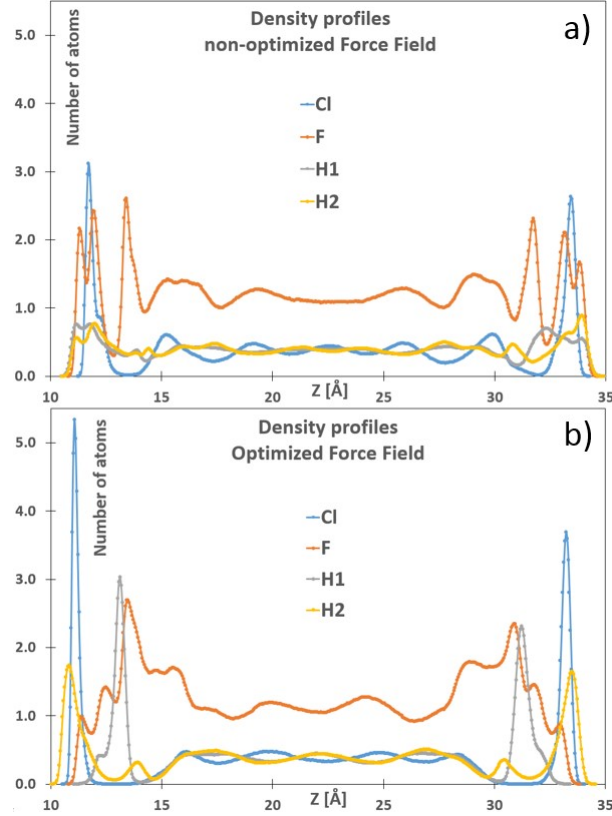
Figure III.8: Number density profiles in the contact, with $P_z = 500\,\mathrm{MPa}$, $v_x = \pm 10\,\mathrm{m/s}$ and wall temperature $T = 283\,\mathrm{K}$. a) with the non-optimized FF, thus obtained with classical Lorentz-Berthelot mixing rules; b) with the optimized FF.

Figure III.8 underlines a difference in the refrigerant molecular structure at the surface. In case (b) of Figure III.8, a high concentration of refrigerant molecules is observed next to the surfaces. Specifically, in case (b), hydrogens H2 are localized close to the surface and the density of chlorine atoms at the interface becomes higher than that in case (a). In contrast, H1 atoms are repelled from the surface. This high presence of chlorine at the interface reproduces well the ab-initio results. Indeed, it was concluded that the refrigerant molecule could be strongly adsorbed on the surface thanks to chlorine atoms. The nonsymmetrical features of the density profiles suggest that desorption timescales are much higher than the 10 ns of this shearing stage, so that molecules locked at the surface do not have the time to equilibrate with the bulk. The presence of hydrogen H2, chlorine and a non-negligible amount of fluorine atoms near the surface suggests that the fifth ab-initio adsorption case (see Table II.1) is the most representative here at the interface. Case 5 owns the second highest binding energy ($E_b \approx -0.70$ eV) just following case 4 obtained with horizontal positions of the molecule ($E_b \in [-0.92; -0.82]$ eV) (see

Table II.1). The ab-initio studies were all single molecule studies, and the preference for case 5 over case 4 is more likely a coverage effect in large scale MD simulations. A preference for perpendicular orientation to the shear at high coverage over a flat conformations at low and medium coverage has also been observed in MD simulations of organic friction modifiers [29, 163].

III.3.4.3   Orientation at the interface

Figure III.9 represents orientations of the refrigerant molecules for classical FF and parametrized FF. 200 snapshots of all atom positions are produced every 50 ps of the global 10 ns to calculate the molecule orientations. For each snapshot and molecule, the angle $\alpha_{z\text{-}C2C3}$ between the C2-C3 bond and the z direction is calculated. The number of molecules is then ranked depending on the value of this angle. Afterwards, the results are averaged over all snapshots. The choice of this angle is justified because it represents well the different orientations obtained at the refrigerant/surface interface with parametrized and classical FF.
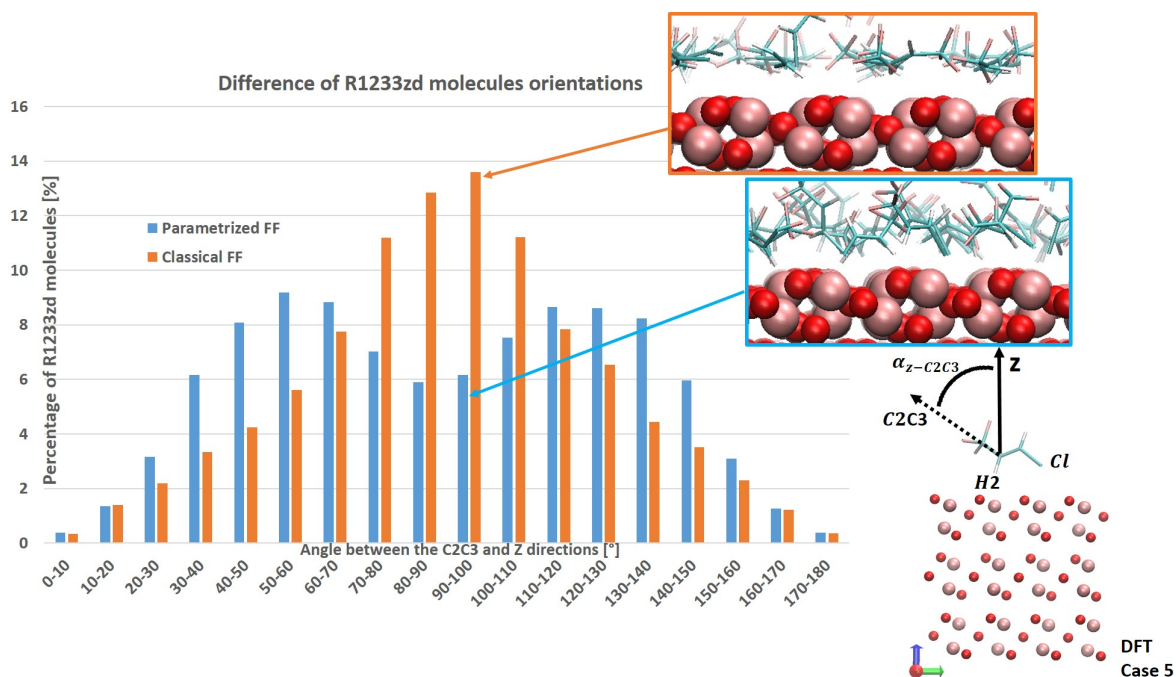
Figure III.9: Angle between C2-C3 bond and z direction obtained with parametrized FF (blue) and classical one (orange).

The refrigerant molecules do not behave similarly at the interface with both FF. Moreover, the double peak observed with the parametrized FF corresponds to a peak for the lower surface and a peak for the upper surface. As described above, the ab-initio Case 5 (see Table II.1) is the more representative for parametrized FF, corresponding to $\alpha_{z\text{-}C2C3}$ fluctuating around 60° at the bottom interface and 130° at the top interface.

On the other hand, with classical FF, the molecules tend to lie flat on the surface, equivalent to $\alpha_{\text{z-C2C3}}$ around 90°. Therefore, the percentage of molecule with $\alpha_{\text{z-C2C3}}$ around 90° is clearly bigger with the classical FF in comparison with orientations obtained with parametrized FF. The remaining flat oriented (around 90°) molecules with parametrized FF are probably located in the center of the film.

III.4 Conclusion

This Chapter firstly presented the MD simulations principles and methods. Then Raabe's FF used to describe the R1233zd refrigerant was introduced, as well as the FF for hematite surfaces. Furthermore, postprocessing methodology is developed to parametrize a force field at the refrigerant-surface interface on the basis of ab-initio results presented in Chapter 2. The information about reactivity of the surface with the refrigerant obtained from DFT calculations is then retained in a parametrized force field in order to study much larger systems. The binding energy values obtained with this parametrized interfacial force field are compared with the ones determined from ab-initio calculations. The maximum difference between MD with parametrized FF and ab-initio results is 10%.

Larger scale MD simulations including this parametrized force field were analyzed. A locked layer of refrigerant on hematite surface was observed and resisted to compression ($P_z = 500\,\text{MPa}$) and shearing ($v_s = 20\,\text{m/s}$). As a consequence the adsorbed molecules of refrigerant could be able to protect the surface against wear in a lubricated contact. Moreover, the high binding energy values could in fine lead to the initial formation of a tribolayer.

Besides, to validate the postprocessing approach, the velocity and density profiles, as well as orientations of the refrigerant molecules in the contact, are compared to the ones obtained with classical mixing rules. The velocity profile does not vary much by using either the parametrized FF or the classical one. However, the density profiles and the orientations at the refrigerant-solid interface are affected. Indeed, with the classical FF, molecules tend to lie flat on the surface, while with the parametrized FF, they lie in direction corresponding to $\alpha_{\text{z-C2C3}}$ fluctuating around 60° at the bottom interface and 130° at the top interface, describing one of the most probable configuration found with ab-initio results. In real conditions (high pressure, small film thickness, rough surfaces), this structural organization might have a large impact on tribological behavior (wear and fatigue resistance). More generally the parametrized force field developed in this study provides the opportunity to study complex systems, more representative of lubricated contact, as detailed in Chapter 4.

Chapter IV

Tribological performance of R1233zd in extreme confinement

Contents

As presented in Chapter 1, rolling bearings in PRL technologies are lubricated within a very thin film (VTF) lubrication regime where the minimum film thickness can be of a few nanometers. Real bearing experimental tests with pure R1233zd as lubricant under variable operating conditions (Hertzian contact pressure around 1.2 GPa in average) were run by SKF company [4, 5]. XPS analysis of the ring steel surfaces revealed that:

- the surface were indeed constituted mainly of iron(II) oxide (FeO) and iron(III) oxide (Fe_2O_3),

- elements constitutive of the R1233zd molecules such as chlorine and fluorine were adsorbed at the surface,

- the thickness of the tribolayer could reach up to 25 nm for long test duration.

These experimental conclusions are qualitatively in line with the main findings of Chapter 3 concerning adsorption of R1233zd at Fe_2O_3 surfaces. Unfortunately, they do not tell much about structure or flow of the confined refrigerant. At this stage, large scale MD simulation of confined R1233zd is an opportunity to test the tribological performance of such a system, providing an in situ and ante-mortem analysis.

Orientations and structurations of refrigerant molecules at the refrigerant/surface interface have been identified in Chapter 3, and the existence of an adsorbed layer of R1233zd at the Fe_2O_3 surface has been shown. In this Chapter, the parametrized FF is implemented in MD simulations to investigate extreme conditions of lubrication. The strength of the adsorbed layer is tested and friction is evaluated at different pressures and sliding velocities. Reducing the quantity of refrigerant one molecule at a time, structural, flow, as well as frictional behaviors are investigated until the film can break down locally. Afterwards, the strength of the adsorbed layer is determined for a contact between a rough surface and a smooth one, where the local pressure undergone by the adsorbed layer is far bigger than the averaged one.

IV.1 R1233zd confined between two smooth iron oxide surfaces

This section aims at studying locking at the refrigerant/surface interface as a function of pressure and sliding velocity when R1233zd is confined between two Fe_2O_3 smooth surfaces. The velocity profiles and the frictional behavior are considered.

We use the system described in Chapter 3, section 3. We consider a 2.1-2.5 nm-thick film (measured at P = 4 GPa and P = 0.5 GPa, respectively), and the wall temperature is fixed at 283 K [3]. The systems are first compressed during 2 ns and then sheared with different sliding velocities from 1 m/s to 100 m/s. In order to compare simulations with

the same sliding distance of 30 nm, sliding stage simulations were run during (30, 15, 6, 3, 1.5, 0.6, 0.3) ns for sliding velocities of (1, 2, 5, 10, 20, 50, 100) m/s, respectively. Due to the periodic boundary conditions, no squeeze-out of the refrigerant molecules is considered in this section. Therefore, structural, flow and frictional behaviors are only studied here in the framework of a full separation of the two surfaces.

IV.1.1   Mobility of confined R1233zd

Figure IV.1 represents the velocity and number density profiles of R1233zd confined between two smooth iron oxide surfaces for three sliding velocities: $v_s = 5\,\text{m/s}$, $10\,\text{m/s}$ and $100\,\text{m/s}$ at P = 4 GPa and for three applied pressures: P = 0.5 GPa, P = 1.5 GPa and P = 4 GPa at $v_s = 100\,\text{m/s}$.
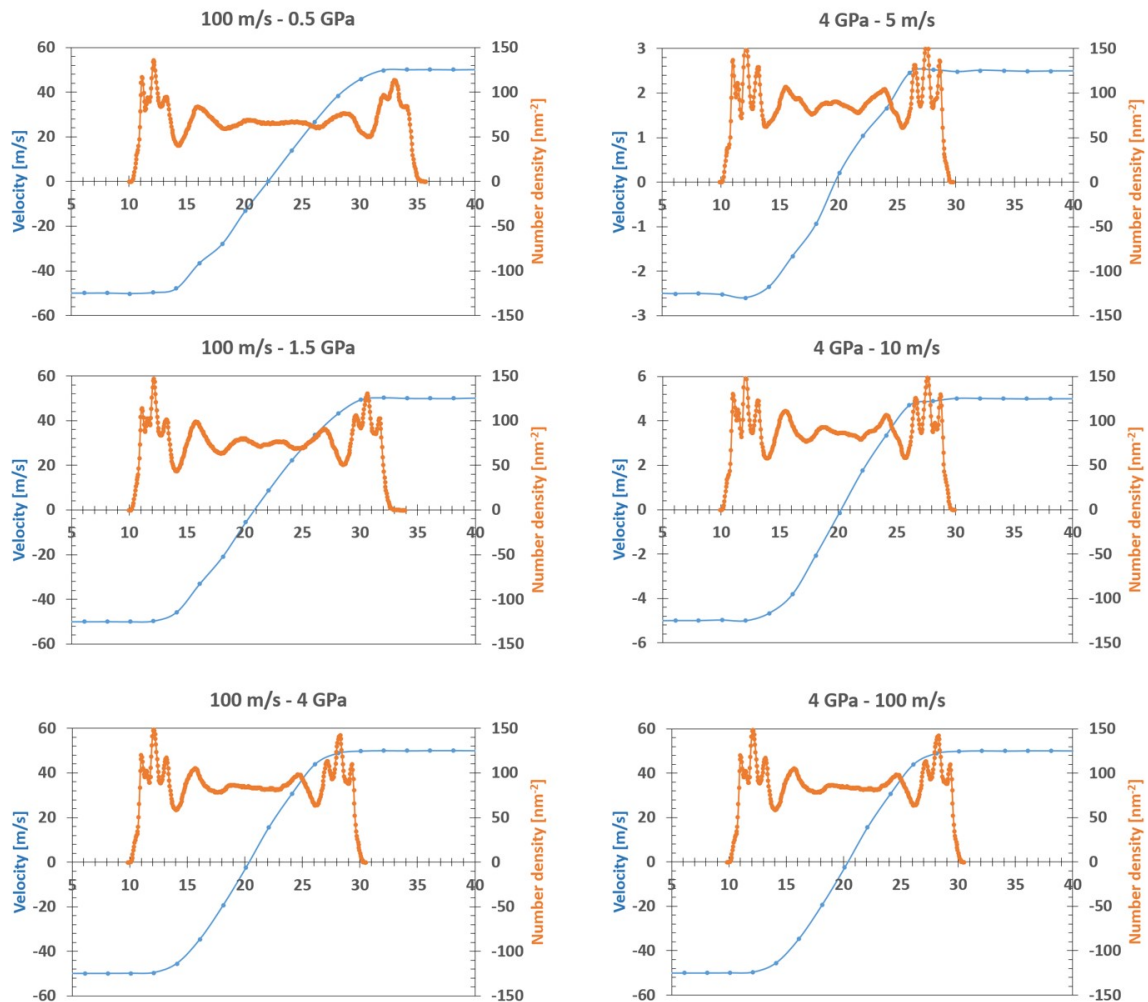
Figure IV.1: Variation of velocity (blue) and number density (orange) profiles within the contact at three different pressures (0.5, 1.5, 4) GPa for $v_s = 100\,\text{m/s}$ and at three sliding velocities v_s: 5 m/s, 10 m/s and 100 m/s for P = 4 GPa.

In all cases, a linear (Couette) velocity profile is observed in the central part of the film

thickness. However, locking appears at the walls: one layer of R1233zd molecules sticks to each wall, whatever the pressure and shear velocity, making the velocity profiles all similar, and refered in the literature [233, 225] as central localization. Both increasing the pressure and increasing the sliding velocity appear to reduce the thickness of adsorbed layers. However, to ensure a better description of these influences, a more precise description is needed.

In order to better represent the dependence of the locking with the pressure and sliding velocity, the locking length is estimated as follows. As a linear velocity profile is observed in the central part of the film thickness, the locking length is calculated here as the distance between the highest atom of the lower surface and the crossing point between the linear part of the velocity profile and the wall speed of the lower surface. The correlation coefficient of the linear calculated part is always higher than 0.99. Figure IV.2 represents the variation of the locking length as a function of the pressure for three sliding velocities: $v_s = 5$ m/s, 20 m/s and 100 m/s.
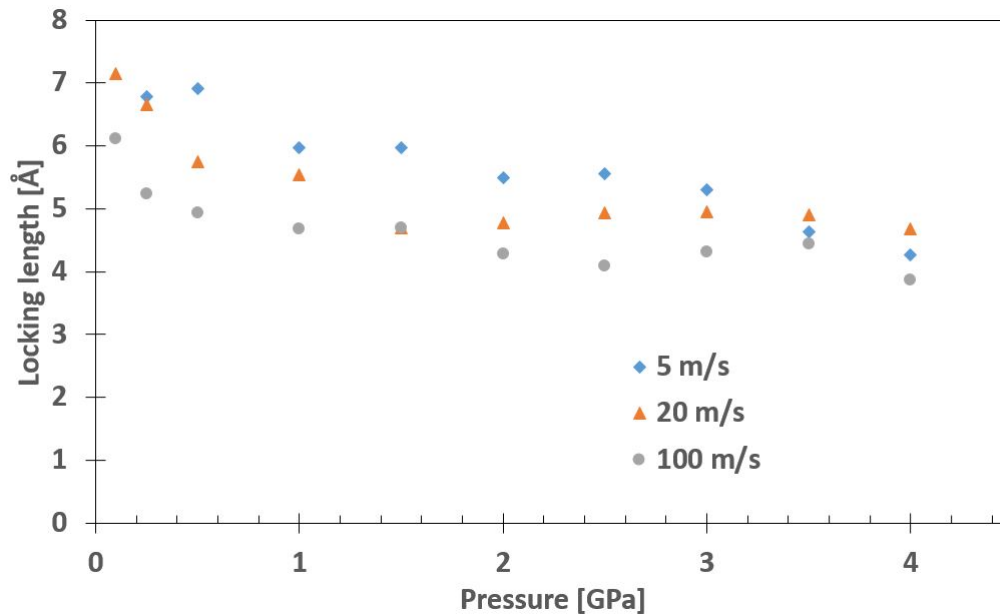
Figure IV.2: Variation of the locking length as a function of pressure for three sliding velocities: 5 m/s, 20 m/s and 100 m/s.

At the lowest sliding velocity of 5 m/s, the profiles become noisy, especially at the lowest pressures of 0.1 GPa and 0.25 GPa. Therefore the locking length of the first points is not represented at $v_s = 5$ m/s in this Figure. Figure IV.2 confirms the previous suggestions. Indeed, the higher pressure forces refrigerant molecules to approach the surface and due to the strong refrigerant/surface interactions, these molecules are locked to the surface in a more compact manner than at lower pressure. Increasing the sliding velocity also reduces the thickness of adsorbed layers. It is possible to imagine that molecules of this layer can be pull-off by the fast moving liquid. Furthermore, for high sliding velocities $v_s = 20$ m/s and 100 m/s and at low pressure (lower than 0.5 GPa), the locking length

decreases strongly with the pressure whereas at higher pressure, the decrease is smaller.

The main result is that the adsorbed molecules at the surfaces stay stuck, whatever the conditions, up to P = 4 GPa and $v_s = 100\,\text{m/s}$.

IV.1.2 Frictional behavior

The friction coefficient Cf is defined as the ratio between the tangential force resisting to the motion and the normal load. In practice, the normal load is imposed, and shearing forces are measured in x direction for each atom of the two virtual surfaces where the velocity is applied (see Chapter 3 Figure III.6). Indeed, in the steady state regime, the mechanical equilibrium of the system requires that the shearing force between the top virtual surface and the top real surface be equal to the shearing force between the top real surface and the liquid. Following the same reasoning with the real and virtual bottom surfaces, we calculate Cf from the average of the top and bottom shearing forces, improving the statistic.

Figure IV.3 presents the variation of Cf with respect to the sliding velocity v_s for four different pressures P = (0.5, 1.5, 3, 4) GPa.
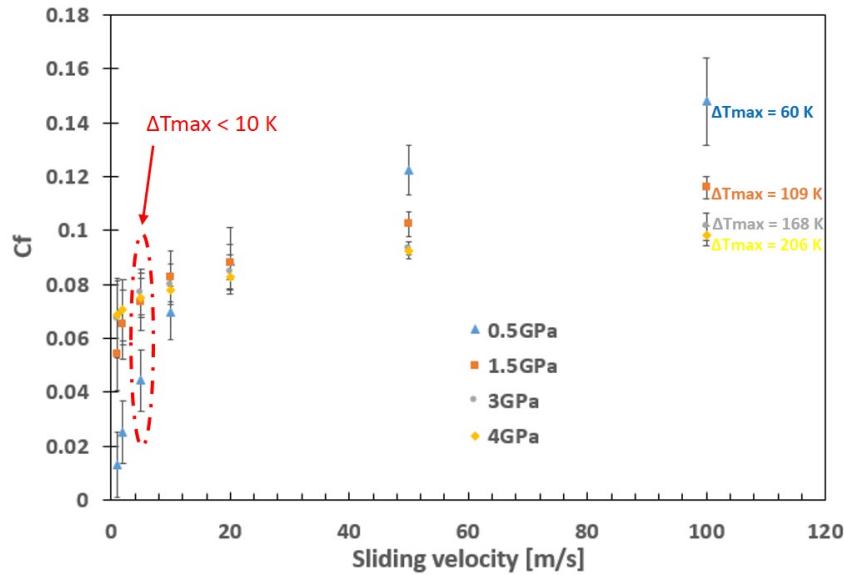
Figure IV.3: Variation of Cf as a function of the sliding velocity for 4 pressures: 0.5 GPa, 1.5 GPa, 3 GPa, 4GPa. The values of the maximum temperature increase in the lubricant film $\Delta Tmax$ at $v_s = 5\,\text{m/s}$ and $v_s = 100\,\text{m/s}$ are also indicated.

At low sliding velocities, the lubricant viscosity is expected to reach a plateau (Newtonian viscosity). Accordingly, Cf should be proportional to the sliding velocity, with the slope being itself proportional to the Newtonian viscosity. The slope should therefore increase with increasing pressure, following a typical piezo-viscous behavior. This is compatible with the results presented in Figure IV.3: at the lowest simulated velocity,

Cf increases with increasing pressure. Figure IV.3 also shows a shear-thinning behavior at large sliding velocities, i.e. the slope of the Cf versus velocity curves decreases with increasing velocity. Shear-thinning is more pronounced (the slope decreases faster) for larger pressures, so that at very large sliding velocity Cf decreases with increasing pressure. At the largest simulated pressures, Cf even seems to reach a plateau as a function of the sliding velocity.

This friction saturation at high shear velocity was observed by several authors [11, 225, 234]. Its interpretation is delicate, and could involve phase change at high pressure [233, 235], or thermal effects. With that regard, Figure IV.3 shows that at the largest sliding velocities, the temperature of the lubricant increases strongly, and depends largely on the pressure. However, differences in shear-thinning behavior as a function of pressure can already be observed for the lowest simulated velocities, for which the increase of the lubricant temperature is very small. Consequently, we suggest that, while thermal effects certainly play a role, they cannot fully explain the observed behavior.

Partial conclusion

In this section, the tribological performance of the R1233zd refrigerant confined between two smooth $\alpha - Fe_2O_3$ surfaces has been studied. MD simulations enriched by the previously defined parametrized FF show that a layer of R1233zd is adsorbed at the surfaces. In all tested cases, the adsorbed layers resist, to both sliding velocity up to 100 m/s and pressure up to 4 GPa. Furthermore, the friction coefficient increases with the sliding velocity and reaches a plateau-like behavior for pressure higher than 3 GPa at high sliding velocity.

IV.2 Towards film breakdown of R1233zd confined between smooth surfaces

In full film regime, no contact between surfaces appear. However, as detailed in Chapter 1, rolling bearings in PRL technologies are lubricated within a VTF lubrication regime where the minimum film thickness reaches a few nanometers. In this case, the separation of surfaces is not guaranteed in the whole contact area and contacts between asperities may occur locally. Therefore, this section aims at describing the case where iron oxide surfaces are very close and only separated by few layers of refrigerant molecules.

As this scale, the influence of the fluid/surface interfacial interactions increases and a deviation from bulk properties is expected. This extreme case has been investigated with MD simulations for linear and branched alkanes [236, 170, 237]. Oscillating solvation forces as well as step-like decrease of the film thickness were observed. A further study describes the step-like evolution of the film thickness, related to the formation of a discrete number of lubricant layers [36]. It was also shown that longer alkanes provide a better surface separation than shorter ones [238]. Here, due to the small size of R1233zd molecules, a detailed investigation of its ability to protect the surfaces in extreme confinement is required.

Local film breakdown can be analyzed by reducing the film thickness down to a dry contact. In this section, the transition between a bilayer to an incomplete monolayer is investigated. Structural and tribological properties are analyzed as the number of molecules is reduced one by one. Specifically, film thickness and density variations with a decreasing number of refrigerant molecules are studied. Then, the orientation of the molecules is considered to examine the film structure during the film breakdown. Finally, the effects of the thickness reduction on velocity accommodation and friction are discussed.

The system is composed of the same materials and force field parameters than the ones described previously in Chapter 3. However, because surfaces become very close one to the other in these new simulations, an additional Buckingham potential with parameters gathered in Table IV.1 is considered between the two Fe_2O_3 surfaces, which has been tested to reproduce thermodynamic and structural properties of Fe_2O_3 [239].

Non-bonded Buckingham $V_{Buck} = Ae^{-\frac{r}{\rho}} - \frac{C}{r^6}$		A [kcal/mol]	ρ [Å]	C [kcal/mol]
	O - O	208074.373	0.265	1962.298
	O - Fe	184954.990	0.190	0.000

Table IV.1: Buckingham parameters for oxygen and iron atoms between the surfaces. Values from [239].

Long-range Coulombic interactions are considered for every atom pair. Two values for

the imposed normal pressure (500 MPa and 1.5 GPa) are considered, with a shearing velocity $v_s = 20$ m/s and a wall temperature fixed at 283 K. Each point of the following curves is obtained after compression and shearing stages, each one during 3 ns. Therefore, 88 initial, very diluted, systems obtained with the Moltemplate software [33] are used for each pressure. Periodic boundary conditions are applied along the x and y directions. Therefore, the number of refrigerant molecules N_{zd} trapped within the contact remains constant during the simulation.

Film thickness, density, velocity and friction coefficient values are calculated and averaged during the shearing stage. The film thickness is calculated every 5 fs and averaged along the simulation. It is defined as the distance between the lowest atoms of the upper virtual surface and the highest atoms of the lower virtual surface. Furthermore, densities and velocity profiles are calculated every 5 fs and 10 fs, respectively, and then averaged over the simulation time.

IV.2.1 Film thickness and density

The film thickness h variation with the number of refrigerant molecules N_{zd} is drawn in Figure IV.4 for P = 0.5 GPa (orange) and P = 1.5 GPa (blue).
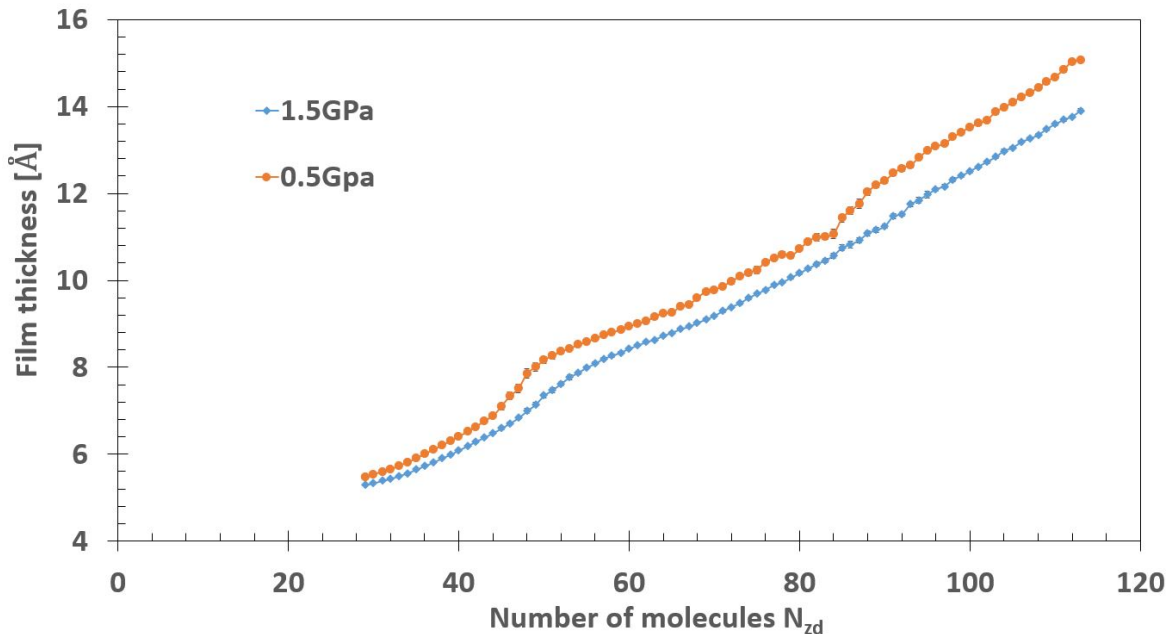
Figure IV.4: Film thickness as a function of the number of refrigerant molecules within the contact with a sliding velocity $v_s = 20$ m/s, at P = 0.5 GPa (orange) and P = 1.5 GPa (blue).

A first result is that h increases monotonously with the number of molecules. Nonetheless, monitoring the height evolution molecule per molecule gives precise information about the formation of bi- and monolayers. Indeed, at P = 0.5 GPa, two inflection

points can be observed with N_{zd} around 44 and 84 molecules respectively, corresponding to the creation/destruction of full layers.

However, it is difficult to locate precisely the inflection points. In particular, the noise on the curves precludes determining them as the points where the second derivative of the curves vanish. An alternative approach to estimate the number of molecules forming full layers is to look at the film density.

The film density is determined as $\rho = \frac{N_{zd} M_{1zd}}{Sh}$, with N_{zd} the number of refrigerant molecules, M_{1zd} the mass of one molecule, S the surface area (roughly $10\,\text{nm}^2$) and h the film thickness between the two virtual surfaces. For comparison, h was also computed as the minimal distance between real surface atoms, or as the maximal distance between fluid atoms, but the results presented below were not affected by the different ways of calculating h. Moreover, the error is calculated as $\rho\frac{\Delta h}{h}$, with Δh the film thickness standard deviation. Figure IV.5 represents the evolution of the film density with the number of molecules, for P = 0.5 GPa and P = 1.5 GPa.
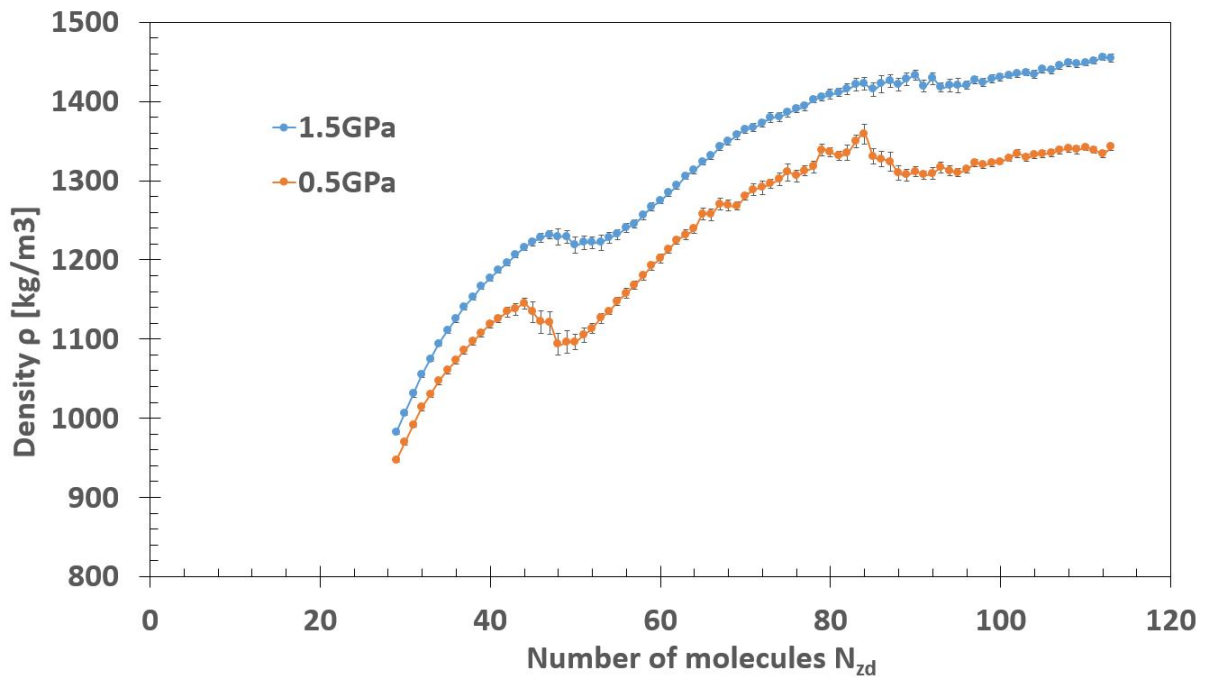
Figure IV.5: Film Density as a function of the number of refrigerant molecules within the contact, with a sliding velocity $v_s = 20\,\text{m/s}$, at P = 0.5 GPa (orange) and P = 1.5 GPa (blue).

Figure IV.5 shows greater variations in comparison with Figure IV.4. Defining full layers as corresponding to maxima in density, at P = 0.5 GPa, a full monolayer is obtained for 4.4 ± 0.1 molecules per nm^2 within the contact. A bilayer is obtained from 5.0 ± 0.1 to 8.4 ± 0.1 molecules per nm^2, with full twin layers at 8.4 ± 0.1 molecules per nm^2. At P = 1.5 GPa, the monolayer is found at 4.7 ± 0.2 molecules per nm^2 and a full bilayer corresponds to 9.0 ± 0.1 molecules per nm^2. Two additional observations can be made. First, the film density increases slightly with higher pressures. Secondly, the density of

101

the bilayer is roughly 20 % larger than the density of a monolayer. Indeed, in the case of a monolayer, refrigerant molecules are more constrained by the surfaces whereas the atoms of two layers can be compacted.

To better understand the structuration and formation process of the full layers and in particular the density drop after mono and bilayers density peaks with increasing the number of molecules, the orientations of R1233zd molecules within the contact are considered.

IV.2.2   Molecule orientation

To describe the process leading to mono and bilayers formation, the orientation of the molecules is analyzed. For a given set of P, v_s and N_{zd}, 60 snapshots of all atom positions are produced over short periods of the global 3 ns of shearing stage to calculate the molecule orientations. For each snapshot and molecule, the angle $\alpha_{\text{z-ClH2}}$ between the Cl-H2 bond and the z axis is calculated. Molecules are then classified according to this angle. Afterwards, the results are averaged over all snapshots. The choice of this angle is justified due to its ability to represent well the perpendicular molecules where chlorine atoms are located near the surface and the CF_3 away from the interface. A small value of $\alpha_{\text{z-ClH2}}$ corresponds to a perpendicular molecule. A molecule is considered perpendicular when $| \alpha_{\text{z-ClH2}} |$ is lower than 30° or comprised between 150° and 180°. Figure IV.6 superimposes the film density (in orange) and the percentage of perpendicular molecules (in blue) between the two surfaces. These features are drawn as a function of the total number N_{zd} of molecules within the contact at P = 0.5 GPa and a sliding velocity $v_s = 20 \, \text{m/s}$.

These curves give information about the transition processes between the last layers. Indeed, when the quantity of refrigerant is progressively reduced, the film density sharply increases just before reaching a full bilayer at 84 molecules or before a monolayer at 44 molecules, corresponding to a fast decrease of the volume. This process can be linked to the orientation of the molecules in this area. Indeed, the number of perpendicular molecules strongly increases during these two density rises as the quantity of refrigerant is reduced. This percentage of perpendicular molecules rises up to around 13% of the total number of molecules. It corresponds to the trend of the molecules to bridge layers until one is eliminated. Then this percentage sharply decreases and only around 4% of the total molecules are orientated perpendicularly when a full mono- or bilayer is reached. By reducing further the quantity of refrigerant after reaching the monolayer, the percentage of perpendicular molecules reaches zero due to a flat orientation of the remaining molecules.
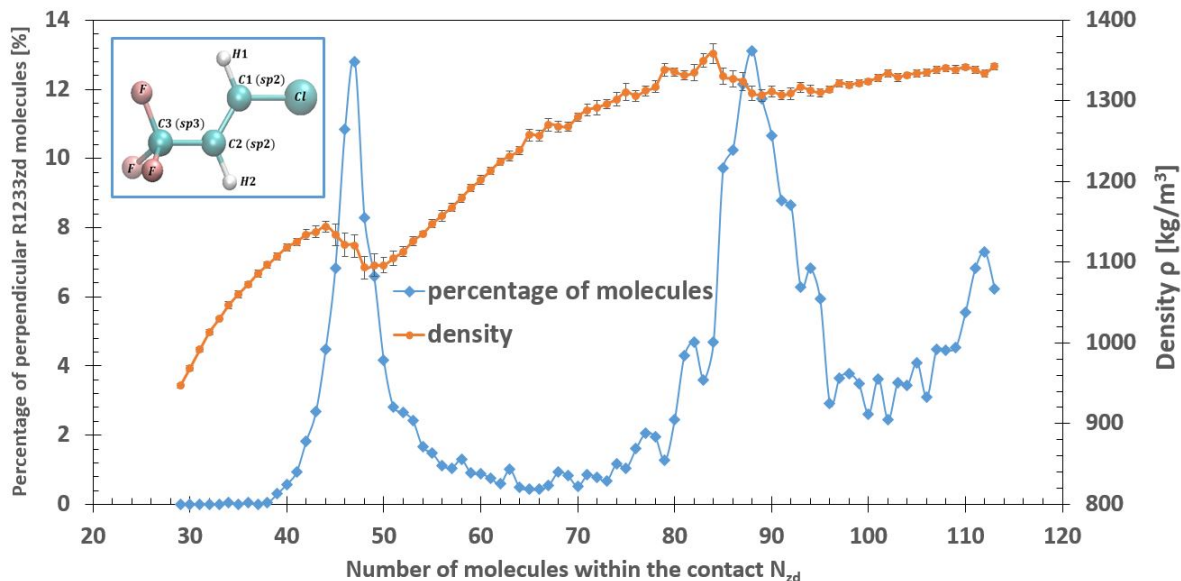
Figure IV.6: Percentage of perpendicular molecules (in blue) as a function of number of molecules within the contact in comparison with the density (in orange), at P = 0.5 GPa and with a sliding velocity $v_s = 20\,\mathrm{m/s}$.

Self-assembled monolayer (SAM) showing compact arrangements of adsorbed molecules to the surfaces, were not found in these MD simulations, neither as in similar MD works involving fatty acids [158], where they were expected. This is possibly because MD simulations can only consider very short periods of time compared to real experiments. Indeed, the SAM formation is expected to take more than few nanoseconds. To check the robustness of predefined potential SAM structures for R1233zd on Fe_2O_3 surfaces, a full study would be required. Nevertheless, XPS experimental analysis with this refrigerant suggest that a thick tribolayer (up to 25 nm) can be formed after a long period of test, confirming the interest for such a characterization.

IV.2.3 Structure and flow

At the nanometer scale, the film structure is far from the bulk behavior and the density, as well as the velocity profiles, can provide further insight. In comparison with the long-chain alkanes in the previously cited studies [236, 170, 36, 238], the R1233zd molecule is composed of several atom types with different molar masses. Thus, in order to better represent the distribution of atoms across the film thickness, the number density will be drawn instead of the mass density. Figure IV.7 represents four characteristic cases of structuration and particular dynamics across the film thickness at an applied pressure of 0.5 GPa. By reducing the quantity of refrigerant, case a) describes a full bilayer (8.4 molecules per nm^2); case b) (5.0 molecules per nm^2) represents the highest N_{zd} for which wall slip appears at the interfaces; case c) is representative of a full monolayer (4.4

molecules per nm^2); finally, case d) represents a half-filled monolayer, thus 2.2 molecules per nm^2.
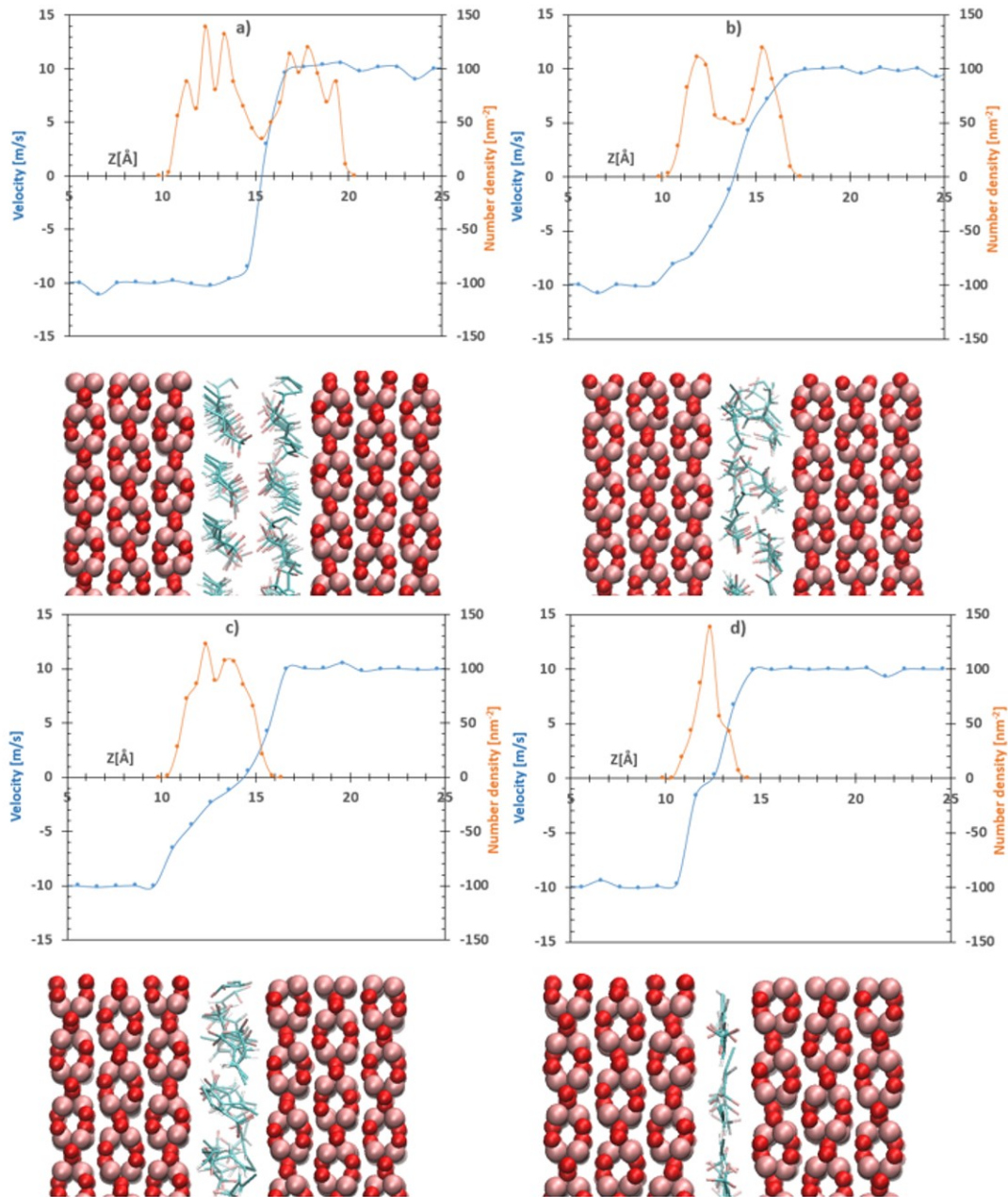
Figure IV.7: Number density and velocity profiles across the film thickness for four different N_{zd} – a)$N_{zd} = 84$, b)$N_{zd} = 50$, c)$N_{zd} = 44$, d)$N_{zd} = 22$ – at 0.5 GPa, a sliding velocity of 20 m/s and a wall temperature of 283 K.

For a full bilayer (case a), the refrigerant molecules are located within a thickness of around 10 Å. In this case, both layers are locked to the nearest surface, due to the high interfacial interactions. Therefore, the shearing occurs between the two layers (central localization), as shown with the velocity profiles. It is of particular interest to underline that the two layers of R1233zd are still adsorbed to the surfaces even at such an extremely high shear rate (higher than $10^{10}\,\text{s}^{-1}$). This remark contributes to explain

why a tribolayer is expected even in severe conditions, as shown experimentally [4, 5] and how far lubrication with such a refrigerant can be considered. Case b represents the first situation where a wall slip occurs at the interface. Indeed, the cohesion between the two layers increases due to bridging molecules, and slip between the layers and the surfaces becomes favorable. At the lower fluid/surface interface (at z = 10 Å), the speed of the point directly located after the interface is different from that of the wall. However, it is less clear at the interface with the top surface (at z = 17.4 Å), where a weak locking seems to remain. In the middle of the density profile, the number of atoms is larger than in case a (full bilayer), meaning that bridges appear between the two layers. As a consequence, the thicknesses of both layers are reduced, together with the width of density peaks. Case c describes a full monolayer where a broad foreseeable wall slip is observed. A large part of the velocity difference between the surfaces is also accommodated by shear of the monolayer itself, molecules moving independently from the others. In case d, the density peak is thinner because molecules are in flat orientations, as detailed previously, and slip at the wall is predominant.

IV.2.4 Consequences on the shear stress

Figure IV.8 represents the variation of the shear stress τ and of the density as a function of N_{zd}, the number of refrigerant molecules within the contact, at P = 0.5 GPa and P = 1.5 GPa.

Starting from the maximum number of molecules, when the quantity of lubricant is reduced, the shear stress τ increases, corresponding to the appearance of molecules perpendicular to the surfaces bridging the layers (see Figure IV.6), before reaching a full bilayer. With two full distinct layers in the film, a local maximum of shear stress is observed. By reducing the number of refrigerant molecules, the shear stress decreases slightly because of decreasing the number of molecules countering the surface movement. Then τ strongly rises until a monolayer is obtained. During this increase, the two layers progressively merge into a single monolayer and therefore the percentage of perpendicular molecules, bridging the two layers, rises (see Figure IV.6). As soon as the two layers are merging into one layer at 5.0 molecules per nm^2 for P = 0.5 GPa, the refrigerant film is sheared, and starts slipping on both walls.
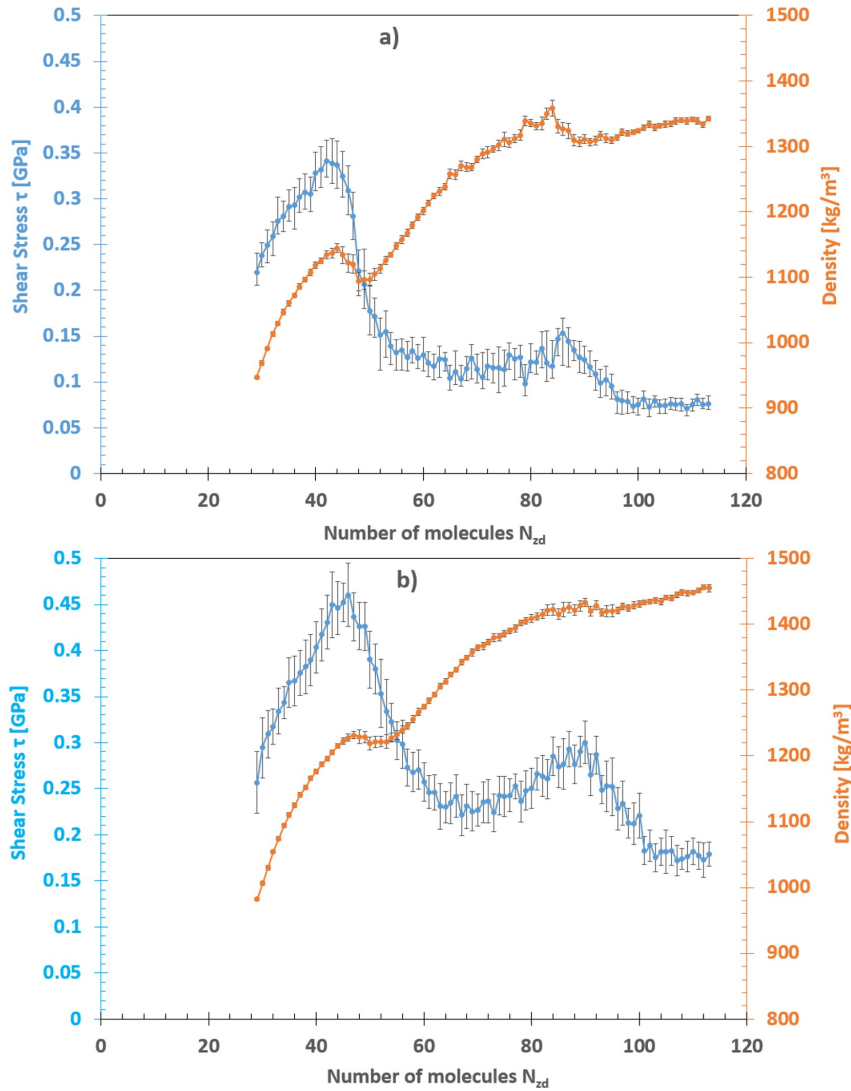
Figure IV.8: Refrigerant film density (orange) and shear stress τ (blue) as a function of N_{zd}, the number of refrigerant molecules within the contact for P = 0.5 GPa (a) and P = 1.5 GPa (b).

A maximum value of τ is obtained for a full monolayer separating the surfaces. At this point, wall slip is unavoidable. Indeed, both surfaces move in opposite directions and the shearing only occur within one refrigerant layer. Therefore, only the refrigerant/surface interfacial interactions determine the frictional behavior. As shown in Chapter 3, the well-depth energy ε_{ij} of Lennard-Jones potential are high to represent adsorption ability of the R1233zd molecule on hematite surfaces. These strong interactions lead to a very high shear stress $\tau = 0.34\,\text{GPa}$ at P = 0.5 GPa and $\tau = 0.46\,\text{GPa}$ at P = 1.5 GPa. Furthermore, as the film thickness is very small with only a monolayer separating the two surfaces, adhesion pressures between the two surfaces, due to Van der Waals and electrostatic interactions can increase friction [36].

Then, the shear stress τ decreases when the number of refrigerant molecules is reduced further. Less R1233zd molecules have to be sheared involving a lower resistance to the

movement of surfaces and thus a lower tangential force. Therefore a lower τ is found in comparison with a full monolayer.

Comparing Figure IV.8 (a) and (b), the same trends are depicted. Quantitatively, the shear stress τ at P = 1.5 GPa is always higher than at P = 0.5 GPa. This can be attributed to the viscosity-pressure dependence.

Partial conclusion

The properties of R1233zd under extreme confinement between two approaching iron oxides surfaces have been investigated. For P = 0.5 GPa and P = 1.5 GPa, film density peaks appear when full layers are formed (bilayer, monolayer). The number of molecules perpendicular to the surfaces increases drastically when decreasing the number of molecules down to bi- and monolayer, corresponding to bridging molecules between layers. With two full layers separating the surfaces, the film thickness is roughly 10 Å. With a shear velocity $v_s = 20\,\mathrm{m/s}$, the two layers are still adsorbed at the surfaces, despite an extremely high shear rate (higher than $10^{10}\,\mathrm{s^{-1}}$). The adsorbed layers start slipping the surfaces for less than 5.0 molecules per $\mathrm{nm^2}$ (at P = 0.5 GPa). Finally, a local maximum of shear stress is obtained with two full distinct layers in the film. Friction reaches its global maximum exactly when a full monolayer is formed.

IV.3 Layers formation and film breakdown within a rough contact

This section aims at investigating a contact between an asperity and a smooth surface in order to study the adsorbed layers strength in more realistic, extreme cases. Indeed, roughness can have a severe structural impact [37]. The design of the roughness and its implication on the system will be explained. Then, the structure and strength of the adsorbed layer located in the contact area with the roughness will be investigated at different pressures and sliding velocities.

All simulations setups not detailed in this section are the same as in previous ones. To analyze the roughness effects, systems larger than the ones considered previously must be used. In real systems, the root mean square (RMS) roughness can be at least of several nanometers [3] but to limit computational costs, we will consider here a smaller system representative of the apex of an asperity. $(01\bar{1}2)$ slabs of hematite with (x,y,z) dimensions roughly equal to 205 Å × 33 Å × 10 Å are used in this section for the top surface. Moreover, the lower surface is built by rotating the upper surface by 180°, and deforming its shape with a Gaussian function of amplitude A = 15 Å, as follows.

$$Z_{\text{rough}} : x \longmapsto Z_{\text{init}} + Ae^{-\frac{(x-\frac{L_x}{2})^2}{2\sigma^2}} \qquad (IV.1)$$

Where σ is chosen to have a full width at half maximum $H = 2\sqrt{2ln(2)}\sigma = \frac{L_x}{4}$ with L_x the total surface length of 205 Å, Z_{init} the initial z coordinate of each atom and Z_{rough} the new z coordinates. This function is also applied to atoms of the virtual surface. The length of the surface is chosen large enough to increase the radius of curvature at the apex, given by $\frac{\sigma^2}{A} = 31$ Å.

Sinusoidal nanometer-scale roughness [36] or nanoscale fractal roughness[27] can also be found in the literature. However, this latter was used for single iron atom surfaces and not with iron oxide surfaces. Here, owning to the very large radius of curvature of the simulated roughness, we decided to (slightly) deform the ab-initio-optimized structure rather than cutting a rough surface in the bulk crystal. Indeed, the latter procedure would involve to carefully consider the atom charge distribution. Furthermore, with the deformed surface, we can use the parametrized FF obtained from DFT calculations with the $(01\bar{1}2)$ hematite surface orientation. With fractal distribution, one can imagine that other surface orientations would have to be considered. A Langevin thermostat (283 K) with a time relaxation of 0.1 ps is applied to the two third outermost layers of atoms in both planar and rough hematite slabs.

Different amount of refrigerant molecules were tested to ensure a high enough quantity

of molecule spreading on the whole surfaces to form an adsorbed layer and low enough to ensure that a bubble remains trapped between the flat surface areas after compression for each pressure. The aim of this procedure is to ensure that we are indeed testing the strength of the adsorbed layer, and not the compressibility of the fluid. As a result, 600 R1233zd molecules are implemented in the system and each surface is composed of 7200 atoms (not including the virtual atoms). Both compression and shearing stages last 5 ns. Contrary to the previous NEMD studies, only the top surface moves in this section. Pressures from 50 MPa to 3 GPa are applied to the virtual top surface. The velocity is implemented in the x direction for all virtual atoms of the top surface with a shearing velocity value v_s varying from 2 m/s to 50 m/s, while the normal load remains fixed.

In the next sections, the structure and strength of the adsorbed layer located in the contact between the smooth and rough surfaces are analyzed at different pressures and sliding velocities.

IV.3.1   Load bearing capacity at equilibrium

Figure IV.9 presents two compression cases, without shearing at P = (0.1, 1, 3) GPa.

a) 0,1 GPa

b) 1 GPa

c) 3 GPa
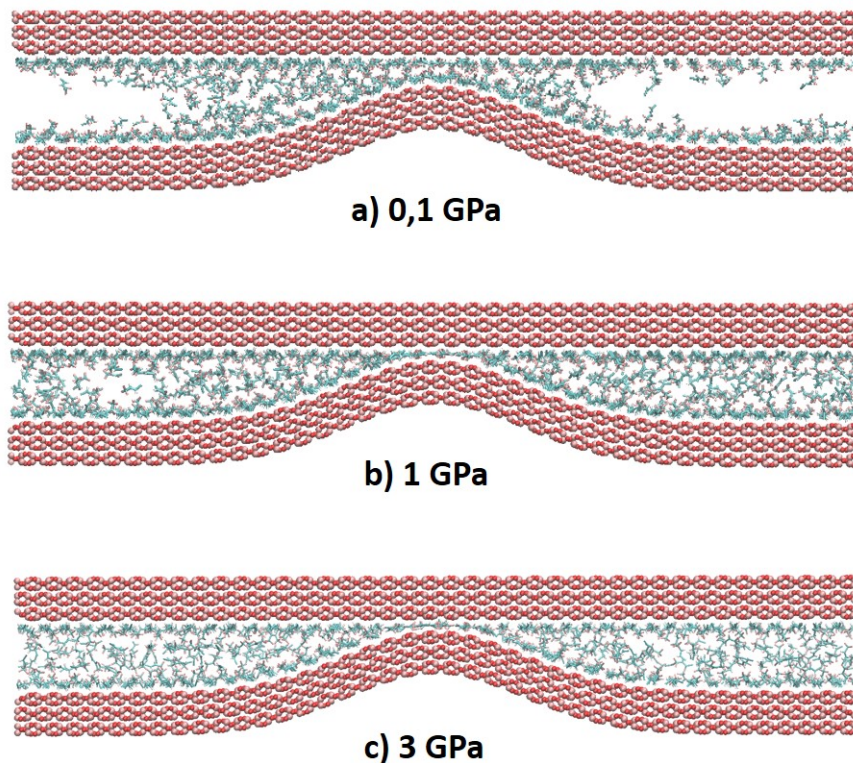
Figure IV.9: Compressed R1233zd refrigerant within a smooth/rough contact at a) P = 0.1 GPa, b) P = 1 GPa and c) P = 3 GPa.

As shown in this Figure, the structure of the adsorbed layer can vary in the contact area.

At 0.1 GPa, a bilayer separates the surfaces, while a monolayer remains at 1 GPa and 3 GPa. In the three cases, the bubble between both surfaces away from the roughness allows for a possible breakdown of adsorbed layers. At P = 3 GPa, the bubble becomes small but can still be observed. Table IV.2 represents the structure of the adsorbed layers compressed within a smooth/rough contact, at different applied pressures P = (0.05, 0.1, 0.3, 0.5, 1, 1.5, 2, 3) GPa. Moreover, the estimated pressures P_c in the contact area are given. The methodology to calculate this local pressure will be explained in the next section.

Pressure [GPa]		Structure
Applied	Estimated in the contact	
0.05	0.3	Bilayer
0.1	0.7	Bilayer
0.3	2.0	Bi-Monolayer transition
0.5	3.3	Monolayer
1	6.6	Monolayer
1.5	9.9	Monolayer
2	13.2	Monolayer
3	19.8	Monolayer

Table IV.2: Structure of the adsorbed layer compressed within a smooth/rough contact at 0.05, 0.1, 0.3, 0.5, 1, 1.5, 2, 3 GPa.

A bi- or monolayer holds at all tested pressures. However, the structure changes in the contact area. For pressure lower than 0.3 GPa ($P_c \approx 2\,\text{GPa}$), a bilayer is still remaining while from 0.5 GPa ($P_c \approx 3.3\,\text{GPa}$) up to 3 GPa ($P_c \approx 19.8\,\text{GPa}$), the quantity of refrigerant in the contact area decreases and a monolayer appears. At 0.3 GPa ($P_c \approx 2\,\text{GPa}$), the simulations remains in a unstable configuration, with mainly two layers, but bridges forming at time interval, probably reflecting a transition to a monolayer.

IV.3.2   Resistance to shearing

The effects of the sliding velocity on the strength and structure of adsorbed layers are analyzed. Four different sliding velocities (2, 5, 10, 50) m/s are considered with the

following pressures: 0.05, 0.1, 0.3, 0.5, 1, 1.5, 2, 3 GPa. Because the force between the two surfaces is transmitted through a very small contact area, the local pressure in this area is much larger than the average pressure imposed in the simulations. To estimate the local pressure in the contact area, the following methodology is used to measure the contact length, as shown in Figure IV.10.
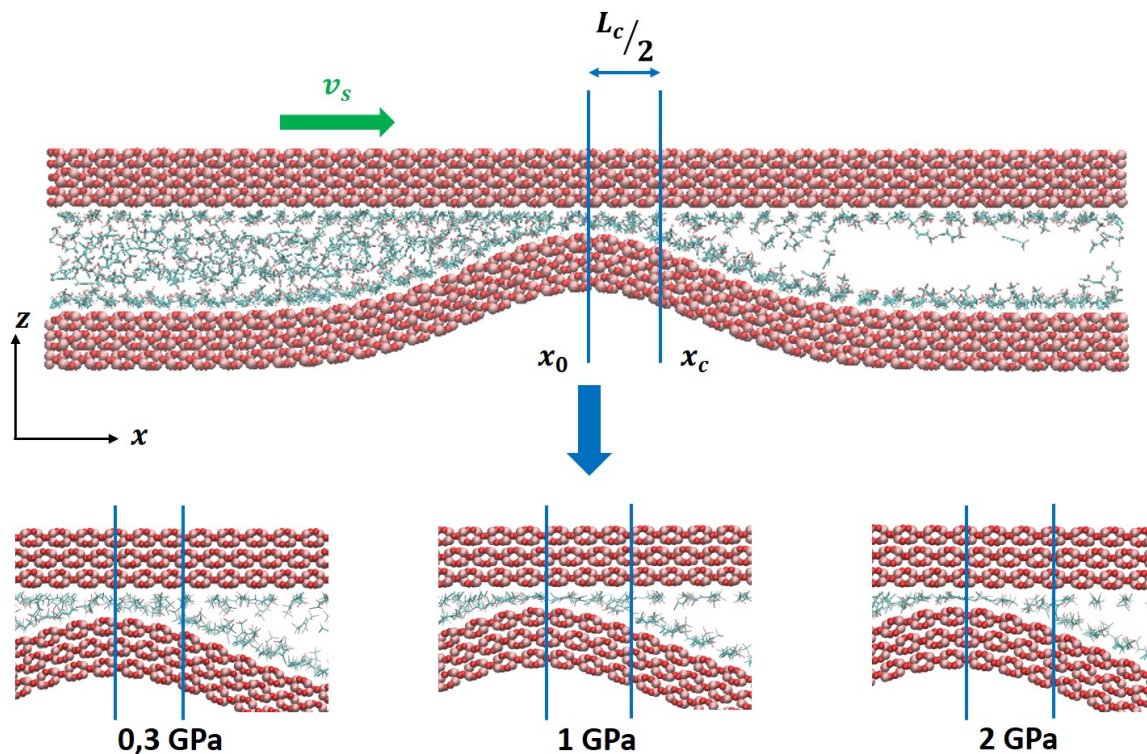
Figure IV.10: Visual estimation of the contact area used to estimate the contact pressure from the global applied pressure.

As the bottom surface does not move, the roughness peak is always located at the position x_0, the middle of the total length $L_x = 205\,\text{Å}$ of the simulations box. Considering the divergence at the exit of the asperity contact region, a bubble zone of vacuum can be identified, starting at position x_c (see Figure IV.10). A rough estimation of the real contact length L_c is proposed as $L_c = 2(x_c - x_0)$.

We would like to emphasize here that this method only provides a qualitative estimate of the local pressure at the contact. Nonetheless, the local pressure is the relevant property for comparison with experiments, and the uncertainty on the estimated value remains small as compared to the range of tested pressures (almost two orders of magnitude). Moreover, the local atomic stress tensor has been used to validate this approach, as shown in Appendice.

From pressure P applied uniformly on the atoms of the virtual top surface, one can derive the effective contact pressure P_c as:

111

$$P_c = P\frac{L_x}{L_c},$$ (IV.2)

where contact boundary x_c varies around $118\,\text{Å}$, thus a ratio $\frac{L_x}{L_c}$ constant for all cases: $\frac{L_x}{L_c} = 6.6$. P_c represents a rough estimation of the real pressure undergone by the refrigerant layers, for comparison purpose only.

Table IV.3 gathers structure information concerning the refrigerant layers under compression and shearing. Moreover, the estimated pressures P_c in the contact area are given.

Pressure [GPa]		Sliding velocity Vs [m/s]			
Applied	Estimated in the contact area	2	5	10	50
0.05	0.3	Bilayer	Bilayer	Bilayer	Bilayer
0.1	0.7	Monolayer	Monolayer	Bi-Monolayer transition	Bilayer
0.3	2.0	Discontinuous	Monolayer	Monolayer	Monolayer
0.5	3.3	Discontinuous	Discontinuous	Monolayer	Monolayer
1	6.6	Discontinuous	Discontinuous	Discontinuous	Monolayer
1.5	9.9	Discontinuous	Discontinuous	Discontinuous	Discontinuous
2	13.2	Breakdown	Discontinuous	Discontinuous	Discontinuous
3	19.8	Breakdown	Breakdown	Breakdown	Breakdown

Table IV.3: Structure of the adsorbed layer compressed and sheared within a smooth/rough contact at 0.05, 0.1, 0.3, 0.5, 1, 1.5, 2, 3 GPa and at sliding velocities of 2, 5, 10, 50 m/s.

At P = 0.05 GPa ($P_c \approx 0.3\,\text{GPa}$), the bilayer resists regardless of the sliding velocity. For the intermediate case with P = 0.1 GPa ($P_c \approx 0.7\,\text{GPa}$), a high sliding velocity v_s, which is here equal to the entrainment velocity of fluid into the asperity contact, is beneficial to keep a stable bilayer ($v_s = 10\,\text{m/s}$ and $50\,\text{m/s}$). In contrast, for smaller sliding velocities, the shearing motion tends to disrupt the bilayer that was stable at rest, resulting in a stable monolayer. No bilayer was obtained at larger pressures under shear.

Figure IV.11 presents top views of the contact area, where both solid surfaces are hidden, in different typical configurations. In particular, at P = 0.3 GPa ($P_c \approx 2\,\text{GPa}$) and the smallest sliding velocity ($v_s = 2\,\text{m/s}$), and at P = 0.5 GPa ($P_c \approx 3.3\,\text{GPa}$) and $v_s = 2\,\text{m/s}$ or $v_s = 5\,\text{m/s}$, Figure IV.11 (a) shows that the refrigerant film is slightly discontinuous. Specifically, holes of one molecular size can appear in the contact area. From P = 1 GPa ($P_c \approx 6.6\,\text{GPa}$) to P = 2 GPa ($P_c \approx 13.2\,\text{GPa}$), the refrigerant film is mainly discontinuous. As illustrated in Figure IV.11 (b), molecules succeed to enter the contact area one by one, but significant gaps appear between them. This case barely represents a single layer of refrigerant. Hydrodynamic entrainment is also observed at P = 1 GPa ($P_c \approx 6.6\,\text{GPa}$) and $v_s = 50\,\text{m/s}$ where a monolayer is formed whereas a discontinuous film stands at lower velocity, and at P = 2 GPa ($P_c \approx 13.2\,\text{GPa}$), where $v_s = 2\,\text{m/s}$ is not sufficient to entrain any molecules inside the contact area, whereas it is the case for higher velocities.

Finally, film breakdown occurs for the smallest velocity at P = 2 GPa ($P_c \approx 13.2\,\text{GPa}$), and for any velocities at P = 3 GPa ($P_c \approx 19.8\,\text{GPa}$). Simulations are stopped when total breakdown of the refrigerant film – and thus a direct contact between surfaces – is detected. Figure IV.11 (c) shows the top view of the contact just before the simulation stops, thus just before the contact of surfaces. Note that, while the estimated local pressures in the contact region seem very high, the situation is similar in real systems, where the local pressure at the contact between asperities can largely overcome the global applied pressure.
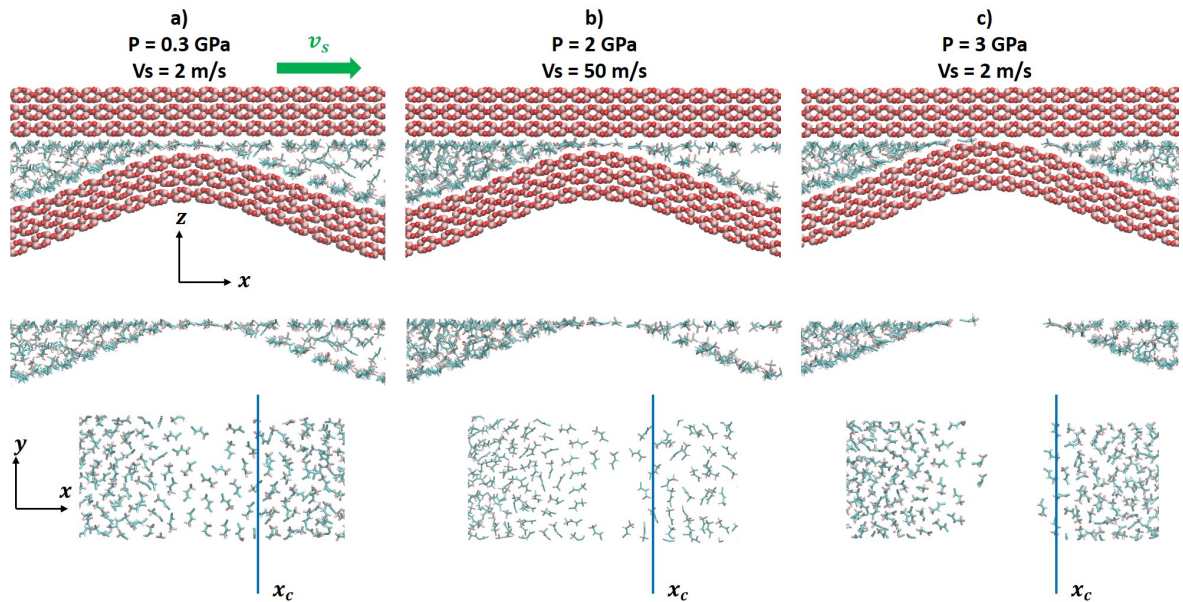
Figure IV.11: Top views from the contact area upon the roughness (both solid surfaces on the top and the bottom are hidden). Slightly discontinuous film (a) at P = 0.3 GPa ($P_c \approx 2\,\text{GPa}$) and $v_s = 2\,\text{m/s}$. Strongly discontinuous film (b) at P = 2 GPa ($P_c \approx 13.2\,\text{GPa}$) and $v_s = 50\,\text{m/s}$. Step before contact (Breakdown) between the two surfaces (c) at 3 GPa ($P_c \approx 19.8\,\text{GPa}$) and $v_s = 2\,\text{m/s}$.

113

Partial conclusion

In this section a rough contact was simulated in order to study the strength and the structure of the refrigerant film located in the contact area, at different pressures and sliding velocities. For pure compression, the film bears up to P = 3 GPa (effective contact pressure $P_c \approx 19.8$ GPa). At P = 0.3 GPa ($P_c \approx 2$ GPa) though, a transition from bilayer presuming adsorbed layer at both surfaces, to monolayer is observed. During the shearing stage, a discontinuity of the adsorbed layer in the contact area appears at P = 0.3 GPa ($P_c \approx 2$ GPa) and small sliding velocity ($v_s = 2$ m/s). From P = 1 GPa ($P_c \approx 6.6$ GPa) to P = 2 GPa ($P_c \approx 13.2$ GPa), the refrigerant film is mainly discontinuous, meaning that molecules enter one by one in the contact area. A high sliding velocity proves to be beneficial for the film formation, due to hydrodynamic entrainment. At P = 2 GPa ($P_c \approx 13.2$ GPa) and $v_s = 2$ m/s or at P = 3 GPa ($P_c \approx 19.8$ GPa) regardless of the velocity, a complete breakdown of the refrigerant film is observed.

IV.4 Conclusion

The goal of Chapter 4 was to analyze the performance of R1233zd lubricated contacts, with iron oxide (Fe_2O_3) surfaces and under extreme conditions, using large scale MD simulations, parametrized by the adapted FF developed in the previous Chapters.

The first case study considers a 2.1-2.5 nm-thick film (measured at P = 4 GPa and P = 0.5 GPa, respectively), confined between atomically smooth surfaces under normal pressure up to 4 GPa, with a shear velocity up to 100 m/s. The main finding is that an adsorbed layer of R1233zd remains adsorbed on both iron oxide surfaces, whatever the tested operating conditions. This is in accordance with experimental XPS analysis of real bearings surfaces under various conditions. Friction increases with the sliding velocity, in a full-film, EHD-like manner, but it saturates for high pressures (P = 3-4 GPa) at very high sliding velocities (Vs = 50-100 m/s, corresponding to shear rates higher than 10^{10} s^{-1}).

The second case study considers ultra-thin film thicknesses from 1.5 nm to 0.5 nm, with atomically smooth surfaces, two pressures of 0.5 GPa and 1.5 GPa and a sliding velocity of 20 m/s. Under these conditions, the refrigerant film develops layers parallel to the surfaces. With 8.4 refrigerant molecules per nm^2 at 0.5 GPa, two twin saturated layers are formed, each one adhering to the nearest surface, and forming adsorbed layers. In this case, the shear velocity is fully accommodated in the central part of the film, by a slip plane between the two layers. With two full distinct layers in the film, a local maximum of friction is observed. However, after a slight decrease of shear stress, when the number of molecules decreases further, molecules perpendicular to the surfaces,

bridging the two layers, are observed, and the two layers progressively merge into a single monolayer. Friction increases drastically during that transition, and the maximum is reached when the monolayer is saturated, with 4.4 molecules per nm^2 at P = 0.5 GPa, and 4.7 molecules per nm^2 at P = 1.5 GPa. As soon as the two layers are merging into one layer, the refrigerant film is sheared, and slips on both walls. A minimum value of 5 refrigerant molecules per nm^2 is necessary at 0.5 GPa for the two adsorbed layers to stick on the surfaces. Finally, the shear stress continuously decreases when molecules are removed from the monolayer.

The third case study aims at representing a more realistic rough contact. A rigid Gaussian-shape longitudinal asperity is created on one fixed surface, while the other surface is flat. At rest, under up to P = 3 GPa applied pressure (corresponding to an estimated local pressure on the asperity $P_c \approx 19.8\,\mathrm{GPa}$) the refrigerant film bears the normal load. A transition appears at P = 0.3 GPa ($P_c \approx 2\,\mathrm{GPa}$) where the structure of the film changes from a bilayer to a monolayer. When a sliding velocity is applied to the smooth surface (from Vs = 2 m/s to 50 m/s) , the film strength decays. For the lowest velocity, transition from bilayer to monolayer appears at P = 0.05 – 0.1 GPa ($P_c \approx 0.3$–$0.7\,\mathrm{GPa}$), and the monolayer splits into individual molecules entering one by one the micro-contact area at P = 1 GPa ($P_c \approx 6.6\,\mathrm{GPa}$). In this pure sliding tests, the imposed shearing velocity also represents hydrodynamic entrainment velocity of R1233zd molecules into the micro-contact area. That is why the refrigerant film resists more at higher velocities. At P = 3 GPa ($P_c \approx 19.8\,\mathrm{GPa}$), film breakdown appears at any tested sliding velocity, and the solid surfaces touch each other.

Conclusion and perspectives

Using a multiscale modeling approach, this PhD thesis explored how physical chemistry of the interface between a refrigerant and an iron oxide surface impacts the tribological performance in a lubricated contact under pure refrigerant lubrication (PRL) conditions.

First, quantum calculations with density functional theory (DFT) have been carried out in order to study the adsorption of the R1233zd refrigerant on iron oxide surface (Chapter 2). The challenging point was to employ a van der Waals (vdW) functional combined with a spin-polarized system by using the DFT+U method. R1233zd molecules are physisorbed on hematite $\alpha - Fe_2O_3(01\bar{1}2)$ surfaces and no chemisorption is observed, as well as no double carbon-carbon bond breaking, and no dissociation of the refrigerant on the surface. Between the R1233zd molecule and the surface, only small exchanges of charge are found with a maximum value of 0.1e. A range of surface-refrigerant molecule binding energies of -0.92 eV to -0.22 eV is observed with sixteen different orientations and positions of the R1233zd molecule on top of the surface. The horizontal positions of the refrigerant molecules are the most stable with a binding energy value of around -0.92 eV. At the surface, iron atoms play a major role in the adsorption process. In the refrigerant molecule, the hydrogen H1 located near the chlorine plays a non-negligible stabilization role.

Second, a postprocessing methodology is developed to parametrize a force field (FF) at the refrigerant-surface interface on the basis of the ab-initio results (Chapter 3). The binding energy values obtained with this parametrized interfacial FF implemented in molecular dynamics (MD) simulations, are compared with the ones determined from ab-initio calculations. The maximum difference between MD with parametrized FF and ab-initio results is on the order of 10 %. Besides, larger scale MD simulations including this parametrized force field were performed. A locked layer of refrigerant on hematite surface was observed. The existence of this strongly adsorbed layer is reminiscent of the tribolayer observed at SKF company. Furthermore, to validate this approach, flow, structure and orientations of R1233zd molecules in the lubricated contact are compared to the ones obtained using standard mixing rules. The density profiles and the orientations of the molecules within the adsorbed layer are affected by the specific parametrization. The orientation of the molecules confirms that the most probable configuration

found with ab-initio results is described with the parametrized FF, considering coverage effects.

The parametrized FF developed in this work provides the opportunity to study complex systems, more representative of lubricated contacts (Chapter 4). In particular, the strength of the adsorbed layer and its ability to protect the surface against wear are tested in large scale MD simulations. This study is divided into three parts, from the less extreme lubrication conditions to the more severe ones. The first case study considers a 2.1-2.5 nm-thick film, confined between atomically smooth surfaces under normal pressure up to 4 GPa, with a shear velocity up to 100 m/s. The main finding is that the adsorbed layer of R1233zd resits on both confining surfaces, whatever the tested operating conditions. This is in accordance with experimental XPS analysis of real bearing surfaces under various conditions. Friction increases with the sliding velocity, in a full-film-like manner, but it saturates for high pressures (3-4 GPa) at very high sliding velocities (50-100 m/s, corresponding to shear rates higher than $10^{10}\,\text{s}^{-1}$). The interpretation of this saturation is complex and could involve, among other phenomena, thermal effects.

The second case study considers ultra-low film thicknesses from 1.5 nm to 0.5 nm, with atomically smooth surfaces, a pressure of 1.5 GPa and a sliding velocity of $20\,\text{m/s}$. Under these conditions, the refrigerant film develops layers parallel to the surfaces. With 8.4 refrigerant molecules per nm^2, two twin saturated layers are formed, each one adhering to the nearest surface. In this case, the shear velocity is fully accommodated in the central part of the film, by a slip plane between the two layers. With two distinct layers in the film, a local minimum of shear stress is observed. However, when the number of molecules decreases, molecules perpendicular to the surfaces, bridging the two layers, are observed, and the two layers progressively merge into a single monolayer. At this point (5 molecules per nm^2), the refrigerant film is sheared, and slips at both walls. Friction increases drastically during that transition, and the maximum is reached when the monolayer is saturated, with 4.4 molecules per nm^2 at 0.5 GPa normal pressure, and 4.7 molecules per nm^2 at 1.5 GPa. Finally, the shear stress continuously decreases when molecules are removed from the monolayer.

The third case study aimed at representing a more realistic rough contact. A rigid Gaussian-shape longitudinal asperity is created on one fixed surface, while the other surface is flat. At rest, under up to an estimated local pressure on the asperity around 19.8 GPa, the refrigerant film bears the normal load. A transition appears at a local pressure around 2 GPa, where the structure of the film changes from a bilayer to a monolayer. When a sliding velocity (from 2 m/s to 50 m/s) is applied to the smooth surface, the film strength decays. For the lowest velocity, transition from bilayer to monolayer appears at local pressure in the range 0.3 – 0.7 GPa, and the monolayer

splits into individual molecules entering one by one the asperity contact area at local pressure around 6.6 GPa. In this pure sliding tests, the imposed shearing velocity also represents hydrodynamic entrainment velocity of R1233zd molecules into the micro-contact area. That is why the refrigerant film resists more at higher velocities. At around 19.8 GPa local pressure, film breakdown appears at any tested sliding velocity, and the solid surfaces touch each other.

The results of this thesis can help industrial manufacturers to understand the physical chemistry and lubrication mechanisms involved with the new generation of refrigerants when dealing with PRL. In the following, perspectives of this work and further investigations are discussed.

- <u>Limits of the current study</u>

One of the main drawback of atomistic numerical models is the prohibitive simulation time required to reach experimental time scales. This precludes the analysis of the formation of potentially thick self-assembled monolayers (SAM) of refrigerant molecules on surfaces, as observed after long experimental tests. A possible continuation of this work, inspired by literature works on fatty acids [29, 158], is to test predetermined thick SAM structures with the help of DFT and large scale MD, and analyze the more likely structures. On the other hand, ab-initio MD (AIMD) should be considered to study the effects of high pressures on chemical reactions, either in the bulk refrigerant or in R1233zd confined between iron oxide surfaces, within a very constrained simulations time.

- <u>Materials</u>

DFT calculations have been shown to be a powerful tool to investigate physical chemistry at the interface between a refrigerant and iron oxide surfaces. Different surface orientations and different iron oxides types could be studied. More importantly, chromium oxide could be considered as this material is typically present at the surface of stainless steel, which is used in PRL bearings. For that purposes, DFT+U simulations have been shown in the literature to represent well this oxide.

As introduced in Chapter 1, mixture of different refrigerants are considered to suppress issues encountered with pure HFO refrigerants, like the flammability. It could be of interest to use the numerical tools to determine the blends properties. In particular, quantum calculations could be considered to predict chemical reactions between the different molecules of refrigerant.

- <u>Rheology</u>

Rheological properties of R1233zd and more generally of any new HFO refrigerant, at high pressure and shear rate, can be investigated further. Indeed, all publications related to R1233zd physical properties consider very low pressure (a few MPa). As the pressure can rise to a few GPa in tribological systems, it is questionable to use these results to predict the film thickness in macroscale models. Experiments with refrigerants at high pressure would be vital, but remain difficult due to their low boiling point leading to evaporation during set up of the test. Besides, because of their potentially high reactivity, HFO molecules can react with elements of high pressure viscometers or densimeters, in particular with sealing elements. On the other hand, MD simulations could be used to predict the density and viscosity variations at high pressure.

- <u>Towards macroscopic contacts</u>

A multi-scale approach was developed in this thesis from the electronic structure to atomistic simulations. A great scientific and industrial breakthrough would be to extend this strategy up to continuum descriptions of macroscopic lubricated contacts. A nano-EHL multi-scale approach was developed [240, 241] to bridge the gap between atomistic simulations and continuous models in presence of interfacial slip behavior. An extension of this approach would be to implement the occurrence of locking of adsorbed layer into continuum models such as the Reynolds equation.

Appendice

The Table IV.4 shows a small difference between the pressure obtained with the rough estimation explained in Chapter 4 and the pressure calculated from the local atomic stress tensor, validating the approach performed in this work.

Applied pressure [GPa]	Local pressure [GPa]	
	Rough estimation	Local atomic stress tensor
0.05	0.3	0.7
0.10	0.7	1.0
0.30	2.0	2.6
0.50	3.3	4.0
1.00	6.6	7.5
1.50	9.9	10.6
2.00	13.2	13.5
3.00	19.8	19.3

Table IV.4: Comparison between the rough estimated pressures and the pressures obtained from the local atomic stress tensor.

Bibliography

[1] Guillermo E Morales-Espejel, R Hauleitner, and HH Wallin. Pure refrigerant lubrication technology in oil-free centrifugal compressors. *Evolution Online, http://evolution.skf.com/pure-refrigerant-lubrication-technology-in-oil-free-centrifugal-compressors/ (accessed Fev 21, 2018)*, 2017.

[2] Guillermo E Morales-Espejel, Hans H Wallin, Rudolf Hauleitner, and Magnus Arvidsson. Progress in rolling bearing technology for refrigerant compressors. *Proceedings of the Institution of Mechanical Engineers, Part C: Journal of Mechanical Engineering Science*, page DOI: 10.1177/0954406217725772, 2017.

[3] Guillermo E Morales-Espejel, Ralph Meeuwenoord, Armando F Quiñonez, and Rudolf Hauleitner. Film thickness and traction measurements of refrigerant R1233zd used as lubricant in elastohydrodynamic conditions. *Proceedings of the Institution of Mechanical Engineers, Part C: Journal of Mechanical Engineering Science*, 229:244–253, 2015.

[4] Rudolph Hauleitner, G E Morales-Espejel, and M Arvidsson. Tribological aspects of rolling bearings lubricated with refrigerant. *The 6th World Tribology Congress, Beijing, China*, 2017.

[5] Rudolph Hauleitner, G E Morales-Espejel, and M Arvidsson. Forthcoming communication at Herrick conference. *Perdue University, USA, July 9-12*, 2018.

[6] Stéphane Tromp, Laurent Joly, Manuel Cobian, and Nicolas Fillot. Chemical physics at interfaces within a refrigerant-lubricated contact: From electronic structure to large scale molecular dynamics simulations. page DOI: 10.1021/acs.jpcc.7b11267, 2018.

[7] Thomas Reichenbach, Krishnakanta Mondal, Marc Jäger, Thomas Vent-Schmidt, Daniel Himmel, Valentin Dybbert, Albert Bruix, Ingo Krossing, Michael Walter, and Michael Moseler. Ab initio study of co 2 hydrogenation mechanisms on inverse zno/cu catalysts. *Journal of Catalysis*, 360:168–174, 2018.

[8] David Sholl and Janice A Steckel. *Density functional theory: a practical introduction*. John Wiley & Sons, 2011.

[9] Laurent Joly, Gabriele Tocci, Samy Merabia, and Angelos Michaelides. Strong coupling between nanofluidic transport and interfacial chemistry: How defect reactivity controls liquid–solid friction through hydrogen bonding. *The journal of physical chemistry letters*, 7:1381–1386, 2016.

[10] Thi D Ta, A Kiet Tieu, Hongtao Zhu, and Buyung Kosasih. Adsorption of Normal-Alkanes on Fe(110), FeO(110), and Fe2O3(0001): Influence of Iron Oxide Surfaces. *Journal of Physical Chemistry C*, 119:12999–13010, 2015.

[11] Thi Dinh Ta, Anh Kiet Tieu, Hongtao Zhu, Buyung Kosasih, Qiang Zhu, and HT Phan. The structural, tribological, and rheological dependency of thin hexadecane film confined between iron and iron oxide surfaces under sliding conditions. *Tribology International*, 113:26–35, 2017.

[12] Joost Vandevondele, Matthias Krack, Fawzi Mohamed, Michele Parrinello, Thomas Chassaing, and Jürg Hutter. Quickstep: Fast and accurate density functional calculations using a mixed Gaussian and plane waves approach. *Computer Physics Communications*, 167:103–128, 2005.

[13] Jiří Klimeš, David R Bowler, and Angelos Michaelides. Chemical accuracy for the van der Waals density functional. *Journal of Physics: Condensed Matter*, 22:022201, 2010.

[14] Samira Dabaghmanesh, Erik C Neyts, and Bart Partoens. van der waals density functionals applied to corundum-type sesquioxides: bulk properties and adsorption of ch3 and c6h6 on (0001) surfaces. *Physical Chemistry Chemical Physics*, 18:23139–23146, 2016.

[15] SL Dudarev, GA Botton, SY Savrasov, CJ Humphreys, and AP Sutton. Electron-energy-loss spectra and the structural stability of nickel oxide: An lsda+ u study. *Physical Review B*, 57:1505, 1998.

[16] Nelson Y Dzade, Alberto Roldan, and Nora H de Leeuw. A Density Functional Theory Study of the Adsorption of Benzene on Hematite (α-Fe2O3) Surfaces. *Minerals*, 4:89–115, 2014.

[17] Pierre-Alain Garrain. These - Etude ab initio de l'adsorption d'acides amines et peptide sur surfaces modeles d'acier inoxydable. 2012.

[18] Matteo Cococcioni and Stefano De Gironcoli. Linear response approach to the calculation of the effective interaction parameters in the lda+ u method. *Physical Review B*, 71:035105, 2005.

[19] William Humphrey, Andrew Dalke, and Klaus Schulten. VMD: Visual molecular dynamics. *Journal of Molecular Graphics*, 14:33–38, 1996.

[20] M Muraki, T Sano, and D Dong. Elastohydrodynamic properties and boundary lubrication performance of polyolester in a hydrofluoroether refrigerant environment. *Proceedings of the Institution of Mechanical Engineers, Part J: Journal of Engineering Tribology*, 216:19–26, 2002.

[21] Byung Chul Na, Keyoung Jin Chun, and Dong-Chul Han. A tribological study of refrigeration oils under HFC-134a environment. *Tribology international*, 30:707–716, 1997.

[22] M Wasim Akram and Andreas A. Polycarpou. Wear Mechanisms of Gray Cast Iron in the Presence of Environmentally Friendly Hydrofluoroolefin-Based Refrigerant and the Effect of Tribofilm Formation. *Journal of Tribology*, 137:041602, 2015.

[23] Michael P Allen and Tildesley. *Computer simulation of liquids*. Oxford university press, 1989.

[24] Nicolas Voeltzel, Philippe Vergne, Nicolas Fillot, Nathalie Bouscharain, and Laurent Joly. Rheology of an Ionic Liquid with Variable Carreau Exponent: A Full Picture by Molecular Simulation with Experimental Contribution. *Tribology Letters*, 64:25, 2016.

[25] Nicolas Voeltzel, Nicolas Fillot, Philippe Vergne, and Laurent Joly. Orders of magnitude changes in the friction of an ionic liquid on carbonaceous surfaces. *The Journal of Physical Chemistry C*, 122:2145–2154, 2018.

[26] Thi Dinh Ta, A Kiet Tieu, H. T. Zhu, and Buyung Kosasih. Thin film lubrication of hexadecane confined by iron and iron oxide surfaces: A crucial role of surface structure. *The Journal of Chemical Physics*, 143:164702, 2015.

[27] James P Ewen, Sebastián Echeverri Restrepo, Neal Morgan, and Daniele Dini. Nonequilibrium molecular dynamics simulations of stearic acid adsorbed on iron surfaces with nanoscale roughness. *Tribology International*, 107:264–273, 2017.

[28] JP Ewen, DM Heyes, and D Dini. Advances in nonequilibrium molecular dynamics simulations of lubricants and additives. *Friction*, pages 1–38, 2018.

[29] James P Ewen, Chiara Gattinoni, Neal Morgan, Hugh A Spikes, and Daniele Dini. Nonequilibrium molecular dynamics simulations of organic friction modifiers adsorbed on iron oxide surfaces. *Langmuir*, 32:4450–4463, 2016.

[30] Steve Plimpton. Fast Parallel Algorithms for Short – Range Molecular Dynamics. *J Comp Phys*, 117:1–19, 1995.

[31] Gabriele Raabe. Molecular Simulation Studies on the Vapor - Liquid Equilibria of the cis - and trans -HCFO-1233zd and the cis - and trans -HFO-1336mzz. *Journal of Chemical & Engineering Data*, 60:2412–2419, 2015.

[32] Gabriele Raabe and Edward J. Maginn. A force field for 3,3,3-fluoro-1-propenes, including HFO-1234yf. *Journal of Physical Chemistry B*, 114:10133–10142, 2010.

[33] A Jewett, A; Lambert. Moltemplate.

[34] Dawid Toton, Christian D Lorenz, Nikolaos Rompotis, Natalia Martsinovich, and Lev Kantorovich. Temperature control in molecular dynamic simulations of non-equilibrium processes. *Journal of Physics: Condensed Matter*, 22:074205, 2010.

[35] Stefano Bernardi, B. D. Todd, and Debra J. Searles. Thermostating highly confined fluids. *Journal of Chemical Physics*, 132:244706, 2010.

[36] Daniele Savio, Nicolas Fillot, and Philippe Vergne. A molecular dynamics study of the transition from ultra-thin film lubrication toward local film breakdown. *Tribology Letters*, 50:207–220, 2013.

[37] Daniele Savio. Ph.D. Dissertation - Nanoscale phenomena in lubrication : From atomistic simulations to their integration into continuous models, INSA Lyon - Karlsruher Institut für Technologie. 2013.

[38] Energy Information Administration U.S. What's new in how we use energy at home: Results from EIA's 2015 residential energy consumption surfvey (RECS). *https://www.eia.gov/consumption/residential/reports/2015/overview/pdf/ whatsnew_home_energy_use.pdf / (accessed Dec 06, 2017)*, 2017.

[39] Jeff Biddle. Explaining the spread of residential air conditioning, 1955–1980. *Explorations in Economic History*, 45(4):402–423, 2008.

[40] Mat Santamouris. Cooling the buildings–past, present and future. *Energy and Buildings*, 128:617–638, 2016.

[41] Michael A McNeil and Virginie E Letschert. Future air conditioning energy consumption in developing countries and what can be done about it: the potential of efficiency in the residential sector. *Lawrence Berkeley National Laboratory*, 2008.

[42] James M Calm. The next generation of refrigerants–historical review, considerations, and outlook. *international Journal of Refrigeration*, 31(7):1123–1133, 2008.

[43] Vijay Wasudeo Bhatkar, VM Kriplani, and GK Awari. Alternative refrigerants in vapour compression refrigeration cycle for sustainable environment: a review of recent research. *International Journal of Environmental Science and Technology*, 10:871–880, 2013.

[44] M.J. Molina and F.S. Rowland. Stratospheric sink for chlorofluoromethanes: chlorine atom-catalysed destruction of ozone. *Nature*, 249:810 – 812, 1974.

[45] J Doucet, P Sauvageau, and C Sandorfy. Vacuum ultraviolet and photoelectron spectra of fluoro-chloro derivatives of methane. *The Journal of Chemical Physics*, 58:3708–3716, 1973.

[46] United Nations. Montreal protocol on substances that deplete the ozone layer. *https://treaties.un.org/doc/Treaties/1989/01/19890101%2003-25%20AM/Ch_XXVII_02_ap.pdf / (accessed Oct 26, 2017)*, 1987.

[47] J Steven Brown, Samuel F Yana-Motta, and Piotr A Domanski. Comparitive analysis of an automotive air conditioning systems operating with co 2 and r134a. *International Journal of refrigeration*, 25:19–32, 2002.

[48] MADHU SRUTHI EMANI, RANENDRA ROYb, and BIJAN KUMAR MANDAL. Development of refrigerants: A brief review. *Indian J. Sci. Res*, 14:175–181, 2017.

[49] Xiaomin Wu, Shan Hu, and Shaojia Mo. Carbon footprint model for evaluating the global warming impact of food transport refrigeration systems. *Journal of cleaner production*, 54:115–124, 2013.

[50] Report of the refrigeration, air conditioning and heat pumps, technical options commitee. *https://http://conf.montreal-protocol.org/meeting/mop/mop-27/presession/Background%20Documents%20are%20available%20in%20English %20only/RTOC-Assessment-Report-2014.pdf (accessed Fev 19, 2018)*, 2014.

[51] Cindy Newberg. Update on Kigali Amendment to the Montreal Protocol Montreal Protocol on Substances that Deplete the Ozone Layer, U.S. Environmental Protection Agency. *https://www.epa.gov/sites/production/files/2016-11/documents/newberg_kigaliamend_122016.pdf / (accessed Oct 26, 2017)*, 2016.

[52] Gabriele Raabe. Molecular simulation studies in hydrofluoroolefine (HFO) working fluids and their blends. *Science and Technology for the Built Environment*, 22:1077–1089, 2016.

[53] Gabriele Raabe and Edward J. Maginn. Molecular Modeling of the Vapor-Liquid Equilibrium Properties of the Alternative Refrigerant 2,3,3,3-Tetrafluoro-1-propene (HFO-1234yf). *Journal of Physical Chemistry Letters*, 1:93–96, 2010.

[54] Chemours. Freon^{TM} 123, Refrigerant (R-123), Properties, Uses, Storage, and Handling. *https://www.chemours.com/Refrigerants/en_US/assets/downloads/freon-123-properties-uses-storage-handling.pdf (accessed Fev 19, 2018)*.

[55] Ole John Nielsen, Meshkat Sadat Javadi, MP Sulbaek Andersen, Michael D Hurley, Timothy J Wallington, and Rajiv Singh. Atmospheric chemistry of cf3cfch2:

Kinetics and mechanisms of gas-phase reactions with cl atoms, oh radicals, and o3. *Chemical Physics Letters*, 439:18–22, 2007.

[56] M. P Sulbaek Andersen, Elna Johanna Kristina Nilsson, Ole John Nielsen, Matthew Stanley Johnson, Michael D Hurley, and Timothy J Wallington. Atmospheric chemistry of trans-cf3ch=chcl: Kinetics of the gas-phase reactions with cl atoms, oh radicals, and o3. *Journal of Photochemistry and Photobiology A: Chemistry*, 199:92–97, 2008.

[57] KO Patten and DJ Wuebbles. Atmospheric lifetimes and ozone depletion potentials of trans-1-chloro-3, 3, 3-trifluoropropylene and trans-1, 2-dichloroethylene in a three-dimensional model. *Atmospheric Chemistry and Physics*, 10:10867–10874, 2010.

[58] T. J. Wallington, M. P. Sulbaek Andersen, and O. J. Nielsen. Atmospheric chemistry of short-chain haloolefins: Photochemical ozone creation potentials (POCPs), global warming potentials (GWPs), and ozone depletion potentials (ODPs). *Chemosphere*, 129:135–141, 2015.

[59] Yohan Lee and Dongsoo Jung. A brief performance comparison of r1234yf and r134a in a bench tester for automobile applications. *Applied Thermal Engineering*, 35:240–242, 2012.

[60] M Wasim Akram, Jacob L Meyer, and Andreas A Polycarpou. Tribological interactions of advanced polymeric coatings with polyalkylene glycol lubricant and r1234yf refrigerant. *Tribology International*, 97:200–211, 2016.

[61] Honghyun Cho and Chasik Park. Experimental investigation of performance and exergy analysis of automotive air conditioning systems using refrigerant r1234yf at various compressor speeds. *Applied Thermal Engineering*, 101:30–37, 2016.

[62] Zhaogang Qi. Performance improvement potentials of r1234yf mobile air conditioning system. *International Journal of Refrigeration*, 58:35–40, 2015.

[63] Adrián Mota-Babiloni, Joaquín Navarro-Esbrí, Ángel Barragán, Francisco Molés, and Bernardo Peris. Drop-in energy performance evaluation of r1234yf and r1234ze (e) in a vapor compression system as r134a replacements. *Applied Thermal Engineering*, 71:259–265, 2014.

[64] Juan Manuel Mendoza-Miranda, Adrián Mota-Babiloni, JJ Ramirez-Minguela, VD Munoz-Carpio, M Carrera-Rodriguez, Joaquín Navarro-Esbrí, and C Salazar-Hernandez. Comparative evaluation of r1234yf, r1234ze (e) and r450a as alternatives to r134a in a variable speed reciprocating compressor. *Energy*, 114:753–766, 2016.

[65] Latra Boumaraf, Philippe Haberschill, and André Lallemand. Investigation of a novel ejector expansion refrigeration system using the working fluid r134a and its potential substitute r1234yf. *international journal of refrigeration*, 45:148–159, 2014.

[66] Francisco Molés, Joaquín Navarro-Esbrí, Bernardo Peris, Adrián Mota-Babiloni, and Ángel Barragán-Cervera. Theoretical energy performance evaluation of different single stage vapour compression refrigeration configurations using r1234yf and r1234ze (e) as working fluids. *International journal of refrigeration*, 44:141–150, 2014.

[67] Milad Ashouri, Mohammad H Ahmadi, Michel Feidt, and Fatemeh Razi Astaraei. Exergy and energy analysis of a regenerative organic rankine cycle based on flat plate solar collectors. *Mechanics & Industry*, 18:217, 2017.

[68] Huixing Zhai, Qingsong An, and Lin Shi. Zeotropic mixture active design method for organic rankine cycle. *Applied Thermal Engineering*, 129:1171–1180, 2018.

[69] Francisco Molés, Joaquín Navarro-Esbrí, Bernardo Peris, Adrián Mota-Babiloni, Ángel Barragán-Cervera, and Konstantinos Kostas Kontomaris. Low gwp alternatives to hfc-245fa in organic rankine cycles for low temperature heat recovery: Hcfo-1233zd-e and hfo-1336mzz-z. *Applied Thermal Engineering*, 71:204–212, 2014.

[70] Joaquín Navarro-Esbrí, Francisco Molés, Bernardo Peris, Adrián Mota-Babiloni, and Konstantinos Kontomaris. Experimental study of an organic rankine cycle with hfo-1336mzz-z as a low global warming potential working fluid for micro-scale low temperature applications. *Energy*, 133:79–89, 2017.

[71] Francisco Molés, Joaquín Navarro-Esbrí, Bernardo Peris, Adrián Mota-Babiloni, and Konstantinos Kostas Kontomaris. Thermodynamic analysis of a combined organic rankine cycle and vapor compression cycle system activated with low temperature heat sources using low gwp fluids. *Applied Thermal Engineering*, 87:444–453, 2015.

[72] Michel Feidt, Abdelhamid Kheiri, Sandrine Pelloux-Prayer, et al. Performance optimization of low-temperature power generation by supercritical orcs (organic rankine cycles) using low gwp (global warming potential) working fluids. *Energy*, 67:513–526, 2014.

[73] Adrián Mota-Babiloni, Joaquín Navarro-Esbrí, Francisco Molés, Ángel Barragán Cervera, Bernardo Peris, and Gumersindo Verdú. A review of refrigerant r1234ze(e) recent investigations. *Applied Thermal Engineering*, 95:211–222, 2016.

[74] Adrián Mota-Babiloni, Joaquín Navarro-Esbrí, Juan Manuel Mendoza-Miranda, and Bernardo Peris. Experimental evaluation of system modifications to increase r1234ze (e) cooling capacity. *Applied Thermal Engineering*, 111:786–792, 2017.

[75] R Hulse, R Singh, and W Spatz. Trans-chloro-3,3,3-trifluoropropene for use in chiller applications. *Patent US 8574451 B2*, 2013.

[76] Bala V Datla and Joost J Brasz. Comparing R1233zd And R245fa For Low Temperature ORC Applications. *International Refrigeration and Air Conditioning Conference*, paper 1524, 2014.

[77] Wang Bingming, Wu Huagen, Li Jianfeng, and Xing Ziwen. Experimental investigation on the performance of nh 3/co 2 cascade refrigeration system with twin-screw compressor. *International Journal of Refrigeration*, 32:1358–1365, 2009.

[78] J Alberto Dopazo, José Fernández-Seara, Jaime Sieres, and Francisco J Uhía. Theoretical analysis of a co 2–nh 3 cascade refrigeration system for cooling applications at low temperatures. *Applied thermal engineering*, 29:1577–1583, 2009.

[79] Adrián Mota-Babiloni, Joaquín Navarro-Esbrí, Ángel Barragán-Cervera, Francisco Molés, Bernardo Peris, and Gumersindo Verdú. Commercial refrigeration–an overview of current status. *International journal of refrigeration*, 57:186–196, 2015.

[80] Xiaoqin Liu, Jianlin Yu, and Gang Yan. Theoretical investigation on an ejector–expansion refrigeration cycle using zeotropic mixture r290/r600a for applications in domestic refrigerator/freezers. *Applied Thermal Engineering*, 90:703–710, 2015.

[81] M Mohanraj, S Jayaraj, C Muraleedharan, and P Chandrasekar. Experimental investigation of r290/r600a mixture as an alternative to r134a in a domestic refrigerator. *International Journal of Thermal Sciences*, 48:1036–1042, 2009.

[82] Juan Manuel Belman-Flores, AP Rodriguez-Munoz, C Gutiérrez Pérez-Reguera, and Adrián Mota-Babiloni. Experimental study of r1234yf as a drop-in replacement for r134a in a domestic refrigerator. *International Journal of Refrigeration*, 81:1–11, 2017.

[83] Martin K Vollmer, Stefan Reimann, Matthias Hill, and Dominik Brunner. First observations of the fourth generation synthetic halocarbons hfc-1234yf, hfc-1234ze (e), and hcfc-1233zd (e) in the atmosphere. *Environmental science & technology*, 49:2703–2708, 2015.

[84] Shigeo Kondo, Kenji Takizawa, and Kazuaki Tokuhashi. Flammability limits of binary mixtures of ammonia with hfo-1234yf, hfo-1234ze, hfc-134a, and hfc-125. *Journal of Fluorine Chemistry*, 149:18–23, 2013.

[85] Shigeru Koyama, Nobuo Takata, and Sho Fukuda. Drop-in experiments on heat pump cycle using hfo-1234ze (e) and its mixtures with hfc-32. international refrigeration and air conditioning conference at purdue, july 12-15. 2010.

[86] Gabriele Raabe. Molecular simulation studies on the vapor–liquid phase equilibria of binary mixtures of r-1234yf and r-1234ze (e) with r-32 and co2. *Journal of Chemical & Engineering Data*, 58:1867–1873, 2013.

[87] B B Chen, P Bonnet, M Y Elsheikh, B L Van Horn, and L Abbas. Compositions of Hydrochlorofluoroolefins. *Patent 20160257867 A1*, 2016.

[88] Series E^{TM} $CenTraVac^{TM}$ chiller product catalog, Trane. *http://www.trane.com/WEBCACHE/RF/CENTRIFUGAL%20LIQUID %20CHILLERS%20(CTV)/PRODUCT/CTV-PRC015B-EN_11122015.pdf (accessed Oct 26, 2017).*

[89] Sebastian Eyerer, Christoph Wieland, Annelies Vandersickel, and Hartmut Spliethoff. Experimental study of an orc (organic rankine cycle) and analysis of r1233zd-e as a drop-in replacement for r245fa for low temperature heat utilization. *Energy*, 103:660–671, 2016.

[90] Francisco Moles, Joaquin Navarro-Esbri, Bernardo Peris, and Adrian Mota-Babiloni. Experimental evaluation of hcfo-1233zd-e as hfc-245fa replacement in an organic rankine cycle system for low temperature heat sources. *Applied Thermal Engineering*, 98:954–961, 2016.

[91] Matthias Welzl, Florian Heberle, and Dieter Brüggemann. Simultaneous experimental investigation of nucleate boiling heat transfer and power output in orc using r245fa and r1233zd (e). *Energy Procedia*, 129:435–442, 2017.

[92] Alejandro Lavernia, Davide Ziviani, Bryce Shaffer, Kunal Bansal, and Eckhard A Groll. Optimization of an organic rankine cycle as bottoming cycle of a 1 kwe genset for residential applications. *Energy Procedia*, 129:867–874, 2017.

[93] Ludovic Guillaume, Arnaud Legros, Adriano Desideri, and Vincent Lemort. Performance of a radial-inflow turbine integrated in an orc system and designed for a whr on truck application: An experimental comparison between r245fa and r1233zd. *Applied Energy*, 186:408–422, 2017.

[94] Fujun Ju, Xiaowei Fan, Yaping Chen, Honglin Zhang, Tuanjie Wang, and Xiangyang Tang. Performance assessment of heat pump water heaters with r1233zd (e)/hcs binary mixtures. *Applied Thermal Engineering*, 123:1345–1355, 2017.

[95] Vladimir L Orkin, Larissa E Martynova, and Michael J Kurylo. Photochemical properties of trans-1-chloro-3, 3, 3-trifluoropropene (trans-chcl=chcf3): Oh reac-

tion rate constant, uv and ir absorption spectra, global warming potential, and ozone depletion potential. *The Journal of Physical Chemistry A*, 118:5263–5271, 2014.

[96] B L Van Horn, M Y Elsheikh, B B Chen, and P Bonnet. Stable Formulated Systems with Chloro-3,3,3- Trifluoropropene. *Patent US 9254468 B2*, 2016.

[97] MP Sulbaek Andersen, Ole John Nielsen, MD Hurley, and TJ Wallington. Atmospheric chemistry of t-cf 3 ch [double bond, length as m-dash] chcl: products and mechanisms of the gas-phase reactions with chlorine atoms and hydroxyl radicals. *Physical Chemistry Chemical Physics*, 14:1735–1748, 2012.

[98] Vladimir L Orkin, Robert E Huie, and Michael J Kurylo. Atmospheric lifetimes of hfc-143a and hfc-245fa: flash photolysis resonance fluorescence measurements of the oh reaction rate constants. *The Journal of Physical Chemistry*, 100:8907–8912, 1996.

[99] Giovanni Di Nicola, Laura Fedele, J Steven Brown, Sergio Bobbo, and Gianluca Coccia. Saturated pressure measurements of trans-1-chloro-3, 3, 3-trifluoroprop-1-ene (r1233zd (e)). *Journal of Chemical & Engineering Data*, 62:2496–2500, 2017.

[100] Ryan J Hulse, Rajat S Basu, Rajiv R Singh, and Raymond H P Thomas. Physical Properties of HCFO-1233zd(E). *Journal of Chemical & Engineering Data*, 57:3581–3586, 2012.

[101] María E Mondéjar, Mark O McLinden, and Eric W Lemmon. Thermodynamic properties of trans-1-chloro-3, 3, 3-trifluoropropene (r1233zd (e)): Vapor pressure,(p, ρ, t) behavior, and speed of sound measurements, and equation of state. *Journal of Chemical & Engineering Data*, 60:2477–2489, 2015.

[102] Chieko Kondou, Ryuichi Nagata, Noriko Nii, Shigeru Koyama, and Yukihiro Higashi. Surface tension of low gwp refrigerants r1243zf, r1234ze (z), and r1233zd (e). *International Journal of Refrigeration*, 53:80–89, 2015.

[103] Laura Fedele, Mariano Pierantozzi, Giovanni Di Nicola, J Steven Brown, and Sergio Bobbo. Compressed liquid density and vapor phase pvt measurements of trans-1-chloro-3, 3, 3-trifluoroprop-1-ene [r1233zd (e)]. *Journal of Chemical & Engineering Data*, 63:225–232, 2018.

[104] R Romeo, PA Giuliano Albo, S Lago, and JS Brown. Experimental liquid densities of cis-1, 3, 3, 3-tetrafluoroprop-1-ene (r1234ze (z)) and trans-1-chloro-3, 3, 3-trifluoropropene (r1233zd (e)). *International Journal of Refrigeration*, 79:176–182, 2017.

[105] Richard A Perkins, Marcia L Huber, and Marc J Assael. Measurement and correlation of the thermal conductivity of trans-1-chloro-3, 3, 3-trifluoropropene (r1233zd (e)). *Journal of Chemical & Engineering Data*, 62:2659–2665, 2017.

[106] Katsuyuki Tanaka. pρt property of trans-1-chloro-3, 3, 3-trifluoropropene (r 1233zd (e)) near critical density. *Journal of Chemical & Engineering Data*, 61:3570–3572, 2016.

[107] Vincent Strubel. *Particle Entrapment in EHD Contacts - Aerospace Applications*. PhD thesis, Lyon, INSA, 2016.

[108] Vincent Strubel, Nicolas Fillot, Fabrice Ville, Jérôme Cavoret, Philippe Vergne, Alexandre Mondelin, and Yves Maheo. Particle entrapment in hybrid lubricated point contacts. *Tribology Transactions*, 59:768–779, 2016.

[109] Jean Frene, Daniel Nicolas, Bernard Degueurce, Daniel Berthe, and Maurice Godet. *Hydrodynamic lubrication: bearings and thrust bearings*, volume 33. Elsevier, 1997.

[110] S Loehlé, C Matta, C Minfray, T Le Mogne, R Iovine, Y Obara, A Miyamoto, and JM Martin. Mixed lubrication of steel by c18 fatty acids revisited. part ii: Influence of some key parameters. *Tribology International*, 94:207–216, 2016.

[111] Mitsuhiro Fukuta, Junki Sumiyama, Masaaki Motozawa, and Tadashi Yanagisawa. Surface tension measurement of oil/refrigerant mixture by maximum bubble pressure method. *International Journal of Refrigeration*, 73:125–133, 2017.

[112] Chaobin Dang, Keitaro Hoshika, and Eiji Hihara. Effect of lubricating oil on the flow and heat-transfer characteristics of supercritical carbon dioxide. *International Journal of Refrigeration*, 35:1410–1417, 2012.

[113] Scott Bair, Wassim Habchi, Mark Baker, and David M Pallister. Quantitative elastohydrodynamic film-forming for an oil/refrigerant system. *Journal of Tribology*, 139:061501, 2017.

[114] M Wasim Akram, Kyriaki Polychronopoulou, and Andreas A Polycarpou. Tribological performance comparing different refrigerant–lubricant systems: The case of environmentally friendly hfo-1234yf refrigerant. *Tribology International*, 78:176–186, 2014.

[115] M Akei, K Mizuhara, T Taki, and T Yamamoto. Evaluation of film-forming capability of refrigeration lubricants in pressurized refrigerant atmosphere. *Wear*, 196:180–187, 1996.

[116] M Akei and K Mizuhara. The elastohydrodynamic properties of lubricants in refrigerant environments©. *Tribology transactions*, 40:1–10, 1997.

[117] Kasper Górny, Arkadiusz Stachowiak, Przemysław Tyczewski, and Wiesław Zwierzycki. Lubricity evaluation of oil–refrigerant mixtures with r134a and r290. *International Journal of Refrigeration*, 69:261–271, 2016.

[118] Ian BELL and Arno LAESECKE. Viscosity of refrigerants and other working fluids from residual entropy scaling. In *16th International Refrigeration and Air Conditioning Conference at Perdue, July 11-14*, 2016.

[119] M Wasim Akram, Kyriaki Polychronopoulou, and Andreas A Polycarpou. Lubricity of environmentally friendly HFO-1234yf refrigerant. *Tribiology International*, 57:92–100, 2013.

[120] Christopher Ciantar, Mark Hadfield, AM Smith, and A Swallow. The influence of lubricant viscosity on the wear of hermetic compressor components in hfc-134a environments. *Wear*, 236:1–8, 1999.

[121] Hiroyuki Fukui, Ken-ichi Sanechika, and Masanori Ikeda. Novel refrigeration lubricants for use with hfc refrigerants. *Tribology international*, 33:707–713, 2000.

[122] Emerson Escobar Nunez, Kyriaki Polychronopoulou, and Andreas A Polycarpou. Lubricity effect of carbon dioxide used as an environmentally friendly refrigerant in air-conditioning and refrigeration compressors. *Wear*, 270:46–56, 2010.

[123] Clare McCabe, Shengting Cui, Peter T Cummings, Peter A Gordon, and Roland B Saeger. Examining the rheology of 9-octylheptadecane to giga-pascal pressures. *The Journal of chemical physics*, 114:1887–1891, 2001.

[124] Bernard J Hamrock and Duncan Dowson. Isothermal elastohydrodynamic lubrication of point contacts: part iii—fully flooded results. *Journal of Lubrication Technology*, 99:264–275, 1977.

[125] Harmen Blok. Inverse problems in hydrodynamic lubrication and design directives for lubricated flexible surfaces. In *Symp. Lubric. & Wear*, pages 1–151, 1963.

[126] Roger Tuomas and Ove Isaksson. Compressibility of oil/refrigerant lubricants in elasto-hydrodynamic contacts. *Journal of tribology*, 128:218–220, 2006.

[127] Kasper Górny, Arkadiusz Stachowiak, and Przemysław Tyczewski. Lubricity evaluation of oil–refrigerant mixtures with R134a and R290. *International Journal of Refrigeration*, 69:261–271, 2016.

[128] A Yokozeki. Solubility correlation and phase behaviors of carbon dioxide and lubricant oil mixtures. *Applied Energy*, 84:159–175, 2007.

[129] Masayoshi Muraki, Takashi Sano, and Daming Dong. Rheological properties of polyolester under an ehd contact in some refrigerant environments. *Journal of tribology*, 123:54–60, 2001.

[130] S Kitaichi, S Sato, R Ishidoya, and T Machida. Tribological analysis of metal interface reactions in lubricant oils/cfc12 and hfc 134a system. In *International Refrigeration and Air Conditioning Conference at Perdue*, 1990.

[131] SE Quinones-Cisneros, J García, Josefa Fernàndez, and Matías Alfonso Monsalvo. Phase and viscosity behaviour of refrigerant–lubricant mixtures. *International journal of refrigeration*, 28:714–724, 2005.

[132] U. J. Jonsson. Lubrication of rolling element bearings with HFC-polyolester mixtures. *Wear*, 232:185–191, 1999.

[133] David R Henderson. Solubility, viscosity and density of refrigerant/lubricant mixtures. Technical report, Spauschus Associates, Inc., Stockbridge, GA (United States); Air-Conditioning and Refrigeration Technology Inst., Inc., Arlington, VA (United States), 1993.

[134] Bo Jacobson, Erik Höglund, Ulf Jonsson, FP Wardle, and H Dolfsma. The effect of refrigerants on the lubrication of rolling element bearings used in screw compressors. In *In: Proceedings of inter- national compressor engineering conference at Purdue, West Lafayette, IN, USA, 1992, pp.523–534*, 1992.

[135] Scott Bair, Mark Baker, and David M. Pallister. Revisiting the Compressibility of Oil/Refrigerant Lubricants. *Journal of Tribology*, 139:1–4, 2016.

[136] Shinji Tanaka, Tsunamitsu Nakahara, and Keiji Kyogoku. Measurements of two-dimensional distribution of refrigerant concentration in ehl film using micro ft-ir and effect of variation of concentration on oil film thickness. *Tribology Letters*, 14:9–15, 2003.

[137] Ulf J Jonsson and N Hansson. Lubrication limits of rolling element bearings in refrigeration compressors. 1998.

[138] Scott Bair. A new high-pressure viscometer for oil/refrigerant solutions and preliminary results. *Tribology Transactions*, 60:392–398, 2017.

[139] Bo O Jacobson and Guillermo E. Morales Espejel. High Pressure Investigation of Refrigerants HFC245fa, R134a and R123. *International Compressor Engineering Conference*, paper C033, 2006.

[140] Guillermo E Morales-Espejel and V Brizmer. Micropitting modelling in rolling–sliding contacts: application to rolling bearings. *Tribology Transactions*, 54:625–643, 2011.

[141] Customer Reference Case SKF. Pure refrigerant lubricated bearings from skf. *http://www.skf.com/binary/76-294546/15640-EN-Pure-refrigerant-lubricated-bearings-reference-case.pdf/ (accessed Fev 21, 2018)*, 2015.

[142] Scott Bair and Arno Laesecke. Viscosity measurements of R32 and R410A to 350 MPa. *International Journal of Refrigeration*, 83:157–167, 2017.

[143] V Brizmer, Antonio Gabelli, Charlotte Vieillard, and Guillermo E Morales-Espejel. An experimental and theoretical study of hybrid bearing micropitting performance under reduced lubrication. *Tribology Transactions*, 58:829–835, 2015.

[144] Philippe Vergne, N Fillot, N Bouscharain, and N Devaux. An experimental and modeling assessment of the HCFC-R123 refrigerant capabilities for lubricating rolling EHD circular contacts. *Proceedings of the Institution of Mechanical Engineers, Part J: Journal of Engineering Tribology*, 229:950–961, 2015.

[145] Duncan Dowson. *History of tribology.* Addison-Wesley Longman Limited, 1979.

[146] HH Wallin and GE Morales-Espejel. Hybrid bearings in oil-free air conditioning and refrigeration compressors. *Evolution Online, http://evolution.skf.com/hybrid-bearings-in-oil-free-air-conditioning-and-refrigeration-compressors/ (accessed Fev 14, 2018)*, 2002.

[147] Honeywell Solstice Liquid Blowing Agent. Technical information, (hfo-1233zd(e). *https://www.honeywell-blowingagents.com/?document=solstice-lba-technical-brochure&download=1 (accessed Fev 14, 2018)*.

[148] Wassim Habchi, Philippe Vergne, Dominique Eyheramendy, and Guillermo E Morales-Espejel. Numerical investigation of the use of machinery low-viscosity working fluids as lubricants in elastohydrodynamic lubricated point contacts. *Proceedings of the Institution of Mechanical Engineers, Part J: Journal of Engineering Tribology*, 225:465–477, 2011.

[149] Arno Laesecke and Scott Bair. High-pressure viscosity measurements of 1, 1, 1, 2-tetrafluoroethane. *International Journal of Thermophysics*, 32:925–941, 2011.

[150] Frédéric Chevalier. *Modélisation des conditions d'alimentation dans les contacts élastohydrodynamiques ponctuels.* PhD thesis, Lyon, INSA, 1996.

[151] Pieter Martin Lugt, RWM Severt, J Fogelströ, and JH Tripp. Influence of surface topography on friction, film breakdown and running-in in the mixed lubrication regime. *Proceedings of the Institution of Mechanical Engineers, Part J: Journal of Engineering Tribology*, 215:519–533, 2001.

[152] Roger G Horn and Jacob N Israelachvili. Direct measurement of structural forces between two surfaces in a nonpolar liquid. *The Journal of Chemical Physics*, 75:1400–1411, 1981.

[153] P Frantz, N Agrait, and M Salmeron. Use of capacitance to measure surface forces. 1. measuring distance of separation with enhanced spatial and time resolution. *Langmuir*, 12:3289–3294, 1996.

[154] Gerd Binnig, Heinrich Rohrer, Ch Gerber, and Edmund Weibel. Surface studies by scanning tunneling microscopy. *Physical review letters*, 49:57, 1982.

[155] Gerd Binnig, Calvin F Quate, and Ch Gerber. Atomic force microscope. *Physical review letters*, 56:930, 1986.

[156] Kai Siegbahn. Electron spectroscopy for atoms, molecules, and condensed matter. *Reviews of Modern Physics*, 54:709, 1982.

[157] Nicholas Metropolis, Arianna W Rosenbluth, Marshall N Rosenbluth, Augusta H Teller, and Edward Teller. Equation of state calculations by fast computing machines. *The journal of chemical physics*, 21:1087–1092, 1953.

[158] Sophie Loehle. Ph.D. Dissertation - Understanding of adsorption mechanisms and tribological behaviors of C18 fatty acids on iron-based surfaces: a molecular simulation approach, Ecole Centrale de Lyon. 2014.

[159] Anke Peguiron, Gianpietro Moras, Michael Walter, Hiroshi Uetsuka, Lars Pastewka, and Michael Moseler. Activation and mechanochemical breaking of c–c bonds initiate wear of diamond (110) surfaces in contact with silica. *Carbon*, 98:474–483, 2016.

[160] P Koskinen, H Häkkinen, G Seifert, S Sanna, Th Frauenheim, and M Moseler. Density-functional based tight-binding study of small gold clusters. *New Journal of Physics*, 8:9, 2006.

[161] Hassan Berro. Ph.D. Dissertation - A Molecular Dynamics Approach to Nanoscale Lubrication, INSA Lyon. 2010.

[162] Seiji Kajita and Maria Clelia Righi. A fundamental mechanism for carbon-film lubricity identified by means of ab initio molecular dynamics. *Carbon*, 103:193–199, 2016.

[163] Michael Doig, Chris P Warrens, and Philip J Camp. Structure and friction of stearic acid and oleic acid films adsorbed on iron oxide surfaces in squalane. *Langmuir*, 30:186–195, 2014.

[164] Carlos Vega, Berthold Saager, and Johann Fischer. Molecular dynamics studies for the new refrigerant r152a with simple model potentials. *Molecular Physics*, 68:1079–1093, 1989.

[165] M Lisal, R Budinskỳ, V Vacek, and K Aim. Vapor–liquid equilibria of alternative refrigerants by molecular dynamics simulations. *International journal of thermophysics*, 20:163–174, 1999.

[166] Farid F Abraham. The interfacial density profile of a lennard-jones fluid in contact with a (100) lennard-jones wall and its relationship to idealized fluid/wall systems: A monte carlo simulation. *The Journal of Chemical Physics*, 68:3713–3716, 1978.

[167] IK Snook and W Van Megen. Solvation forces in simple dense fluids. i. *The Journal of Chemical Physics*, 72:2907–2913, 1980.

[168] Jianping Gao, WD Luedtke, and Uzi Landman. Layering transitions and dynamics of confined liquid films. *Physical review letters*, 79:705, 1997.

[169] Atkinson Jabbarzadeh, JD Atkinson, and RI Tanner. Nanorheology of molecularly thin films of n-hexadecane in couette shear flow by molecular dynamics simulation. *Journal of non-newtonian fluid mechanics*, 77:53–78, 1998.

[170] Jianping Gao, WD Luedtke, and Uzi Landman. Structures, solvation forces and shear of molecular films in a rough nano-confinement. *Tribology letters*, 9:3–13, 2000.

[171] A Jabbarzadeh, Peter Harrowell, and RI Tanner. Low friction lubrication between amorphous walls: Unraveling the contributions of surface roughness and in-plane disorder. *The Journal of chemical physics*, 125:034703, 2006.

[172] JJ Magda, M Tirrell, and HT Davis. Molecular dynamics of narrow, liquid-filled pores. *The Journal of chemical physics*, 83:1888–1901, 1985.

[173] I Bitsanis, JJ Magda, M Tirrell, and HT Davis. Molecular dynamics of flow in micropores. *The Journal of chemical physics*, 87:1733–1750, 1987.

[174] Ioannis Bitsanis, Susan A Somers, H Ted Davis, and Matthew Tirrell. Microscopic dynamics of flow in molecularly narrow pores. *The Journal of Chemical Physics*, 93:3427–3431, 1990.

[175] Susan A Somers and H Ted Davis. Microscopic dynamics of fluids confined between smooth and atomically structured solid surfaces. *The Journal of chemical physics*, 96:5389–5407, 1992.

[176] Ramesh Singh, Joshua Monk, and Francisco R Hung. Heterogeneity in the dynamics of the ionic liquid [bmim+][pf6–] confined in a slit nanopore. *The Journal of Physical Chemistry C*, 115:16544–16554, 2011.

[177] Nicolas Voeltzel. *Molecular simulation of an ionic liquid as lubricant: from bulk rheology to nanoconfinement*. PhD thesis, Lyon, INSA, 2016.

[178] Hassan Berro, Nicolas Fillot, and Philippe Vergne. Molecular dynamics simulation of surface energy and zddp effects on friction in nano-scale lubricated contacts. *Tribology international*, 43:1811–1822, 2010.

[179] Peter A Thompson and Mark O Robbins. Shear flow near solids: Epitaxial order and flow boundary conditions. *Physical review A*, 41:6830, 1990.

[180] Uwe Heinbuch and Johann Fischer. Liquid flow in pores: Slip, no-slip, or multi-layer sticking. *Physical Review A*, 40:1144, 1989.

[181] Ashlie Martini, Hua-Yi Hsu, Neelesh A Patankar, and Seth Lichter. Slip at high shear rates. *Physical review letters*, 100:206001, 2008.

[182] Christopher JS Petrie and Morton M Denn. Instabilities in polymer processing. *AIChE Journal*, 22:209–236, 1976.

[183] Eric Lauga, Michael P Brenner, and Howard A Stone. Microfluidics: the no-slip boundary condition. *Perspective*, 17, 2006.

[184] Lydéric Bocquet and Jean-Louis Barrat. Flow boundary conditions from nano-to micro-scales. *Soft matter*, 3:685–693, 2007.

[185] AV Ramamurthy. Wall slip in viscous fluids and influence of materials of construction. *Journal of Rheology*, 30:337–357, 1986.

[186] A Jabbarzadeh, JD Atkinson, and RI Tanner. Effect of the wall roughness on slip and rheological properties of hexadecane in molecular dynamics simulation of couette shear flow between two sinusoidal walls. *Physical review E*, 61:690, 2000.

[187] Uri Raviv, Pierre Laurat, and Jacob Klein. Fluidity of water confined to sub-nanometre films. *Nature*, 413:51, 2001.

[188] Jianping Gao, Robert Szoszkiewicz, Uzi Landman, Elisa Riedo, et al. Structured and viscous water in subnanometer gaps. *Physical Review B*, 75:115415, 2007.

[189] John Van Alsten and Steve Granick. Molecular tribometry of ultrathin liquid films. *Physical Review Letters*, 61:2570, 1988.

[190] A Jabbarzadeh, Peter Harrowell, and RI Tanner. Crystal bridge formation marks the transition to rigidity in a thin lubrication film. *Physical review letters*, 96:206102, 2006.

[191] Peter A Thompson, Gary S Grest, and Mark O Robbins. Phase transitions and universal dynamics in confined films. *Physical Review Letters*, 68:3448, 1992.

[192] Jacob N Israelachvili. Measurement of the viscosity of liquids in very thin films. *Journal of colloid and interface science*, 110:263–271, 1986.

[193] Michelle L Gee, Patricia M McGuiggan, Jacob N Israelachvili, and Andrew M Homola. Liquid to solidlike transitions of molecularly thin films under shear. *The Journal of chemical physics*, 93:1895–1906, 1990.

[194] Jianping Gao, WD Luedtke, and Uzi Landman. Friction control in thin-film lubrication. *The Journal of Physical Chemistry B*, 102:5033–5037, 1998.

[195] Gustavo Luengo, Jacob Israelachvili, and Steve Granick. Generalized effects in confined fluids: new friction map for boundary lubrication. *Wear*, 200:328–335, 1996.

[196] Hsuan-Wei Hu, George A Carson, and Steve Granick. Relaxation time of confined liquids under shear. *Physical review letters*, 66:2758, 1991.

[197] Mark J Stevens, Maurizio Mondello, Gary S Grest, ST Cui, HD Cochran, and PT Cummings. Comparison of shear flow of hexadecane in a confined geometry and in bulk. *The Journal of chemical physics*, 106:7303–7314, 1997.

[198] Nicolas Voeltzel, Andrew Giuliani, Nicolas Fillot, Philippe Vergne, and Laurent Joly. Nanolubrication by ionic liquids: molecular dynamics simulations reveal an anomalous effective rheology. *Physical Chemistry Chemical Physics*, 17:23226–23235, 2015.

[199] Peihong Cong, Jun Imai, and Shigeyuki Mori. Effect of gas pressure on tribological properties and tribochemical reactions of alumina sliding against zirconia in hfc-134a. *Wear*, 249:142–148, 2001.

[200] D Dascalescu, K Polychronopoulou, and AA Polycarpou. The significance of tribochemistry on the performance of ptfe-based coatings in co2 refrigerant environment. *Surface and Coatings Technology*, 204:319–329, 2009.

[201] Geraldine Theiler, Wolfgang Hübner, Thomas Gradt, P Klein, and K Friedrich. Friction and wear of ptfe composites at cryogenic temperatures1. *Tribology International*, 35:449–458, 2002.

[202] Emerson Escobar Nunez, Seung Min Yeo, Kyriaki Polychronopoulou, and Andreas A Polycarpou. Tribological study of high bearing blended polymer-based coatings for air-conditioning and refrigeration compressors. *Surface and Coatings Technology*, 205:2994–3005, 2011.

[203] Seung Min Yeo and Andreas A Polycarpou. Tribological performance of ptfe- and peek-based coatings under oil-less compressor conditions. *Wear*, 296:638–647, 2012.

[204] Nicholaos G Demas and Andreas A Polycarpou. Tribological investigation of cast iron air-conditioning compressor surfaces in co 2 refrigerant. *Tribology Letters*, 22:271–278, 2006.

[205] Max Born and Robert Oppenheimer. Zur quantentheorie der molekeln. *Annalen der Physik*, 389:457–484, 1927.

[206] David M Ceperley and BJ Alder. Ground state of the electron gas by a stochastic method. *Physical Review Letters*, 45:566, 1980.

[207] Georg Kresse and Jürgen Furthmüller. Efficient iterative schemes for ab initio total-energy calculations using a plane-wave basis set. *Physical review B*, 54:11169, 1996.

[208] S Goedecker, M Teter, and Jürg Hutter. Separable dual-space gaussian pseudopotentials. *Physical Review B*, 54:1703, 1996.

[209] D. D. Johnson. Modified Broyden's method for accelerating convergence in self-consistent calculations. *Physical Review B*, 38:12807–12813, 1988.

[210] H Luth, G W Rubloff, and W D Grobman. Chemisorption and decomposition reactions of oxygen-containing organic molecules on clean Pd surfaces studied by UV photoemission. *Surface Science*, 63:325–338, 1977.

[211] S F₋ Boys and Fiorenza de Bernardi. The calculation of small molecular interactions by the differences of separate total energies. some procedures with reduced errors. *Molecular Physics*, 19:553–566, 1970.

[212] Curt M Breneman and Kenneth B Wiberg. Determining atom-centered monopoles from molecular electrostatic potentials. the need for high sampling density in formamide conformational analysis. *Journal of Computational Chemistry*, 11:361–373, 1990.

[213] Patrick Bultinck, Christian Van Alsenoy, Paul W Ayers, and Ramon Carbó-Dorca. Critical analysis and extension of the hirshfeld atoms in molecules. *The Journal of chemical physics*, 126:144111, 2007.

[214] Graeme Henkelman, Andri Arnaldsson, and Hannes Jónsson. A fast and robust algorithm for bader decomposition of charge density. *Computational Materials Science*, 36:354–360, 2006.

[215] Edward Sanville, Steven D Kenny, Roger Smith, and Graeme Henkelman. Improved grid-based algorithm for bader charge allocation. *Journal of computational chemistry*, 28:899–908, 2007.

[216] W Tang, E Sanville, and G Henkelman. A grid-based bader analysis algorithm without lattice bias. *Journal of Physics: Condensed Matter*, 21:084204, 2009.

[217] Min Yu and Dallas R Trinkle. Accurate and efficient algorithm for bader charge integration. *The Journal of chemical physics*, 134:064111, 2011.

[218] James P Ewen, Chiara Gattinoni, Foram M Thakkar, Neal Morgan, Hugh A Spikes, and Daniele Dini. A comparison of classical force-fields for molecular dynamics simulations of lubricants. *Materials*, 9:651, 2016.

[219] Katie A Maerzke and J Ilja Siepmann. Transferable potentials for phase equilibria-coarse-grain description for linear alkanes. *The Journal of Physical Chemistry B*, 115:3452–3465, 2011.

[220] Siewert J Marrink, H Jelger Risselada, Serge Yefimov, D Peter Tieleman, and Alex H De Vries. The martini force field: coarse grained model for biomolecular simulations. *The journal of physical chemistry B*, 111:7812–7824, 2007.

[221] Adri CT Van Duin, Siddharth Dasgupta, Francois Lorant, and William A Goddard. Reaxff: a reactive force field for hydrocarbons. *The Journal of Physical Chemistry A*, 105:9396–9409, 2001.

[222] R Romeo, P.A. Giuliano Albo, S Lago, and J.S. Brown. Experimental liquid densities of cis-1,3,3,3- tetrafluoroprop-1-ene (R1234ze(Z)) and trans-1- chloro-3,3,3-trifluoropropene (R1233zd(E)). *International Journal of Refrigeration*, 79:176–182, 2017.

[223] Roger W Hockney and James W Eastwood. *Computer simulation using particles*. crc Press, 1988.

[224] Stefano Bernardi, BD Todd, and Debra J Searles. Thermostating highly confined fluids. *The Journal of chemical physics*, 132:244706, 2010.

[225] James P Ewen, Chiara Gattinoni, Jie Zhang, David M Heyes, Hugh A Spikes, and Daniele Dini. On the effect of confined fluid molecular structure on nonequilibrium phase behaviour and friction. *Physical Chemistry Chemical Physics*, 19:17883–17894, 2017.

[226] Daniele Savio, Nicolas Fillot, Philippe Vergne, and Maurizio Zaccheddu. A model for wall slip prediction of confined n-alkanes: effect of wall-fluid interaction versus fluid resistance. *Tribology Letters*, 46:11–22, 2012.

[227] Robert D Engle, Robert D Skeel, and Matthew Drees. Monitoring energy drift with shadow hamiltonians. *Journal of Computational Physics*, 206(2):432–452, 2005.

[228] Thi D. Ta, A. Kiet Tieu, Hongtao Zhu, Qiang Zhu, Prabouno B. Kosasih, Jie Zhang, and Guanyu Deng. Tribological Behavior of Aqueous Copolymer Lubricant

in Mixed Lubrication Regime. *ACS Applied Materials and Interfaces*, 8:5641–5652, 2016.

[229] Clotilde Minfray, Thierry Le Mogne, Jean-michel Martin, Tasuku Onodera, Shuko Takahashi, Hideyuki Tsuboi, Michihisa Koyama, Akira Endou, Hiromitsu Takaba, Momoji Kubo, C.A. Del Carpio, and A Miyamoto. Experimental and Molecular Dynamics Simulations of Tribochemical Reactions with ZDDP: Zinc Phosphate–Iron Oxide Reaction. *Tribology Transactions*, 51:589–601, 2008.

[230] T. Halicioğlu and G. M. Pound. Calculation of Potential Energy Parameters from Crystalline State Properties. *Physica Status Solidi (a)*, 30:619–623, 1975.

[231] Pnina Dauber-Osguthorpe, Victoria A Roberts, David J Osguthorpe, Jon Wolff, Moniqe Genest, and Arnold T Hagler. Structure and energetics of ligand binding to proteins: Escherichia coli dihydrofolate reductase-trimethoprim, a drug-receptor system. *Proteins: Structure, Function, and Bioinformatics*, 4:31–47, 1988.

[232] In-Chul Yeh and Max L Berkowitz. Ewald summation for systems with slab geometry. *The Journal of chemical physics*, 111:3155–3162, 1999.

[233] Laetitia Martinie and Philippe Vergne. Lubrication at extreme conditions: a discussion about the limiting shear stress concept. *Tribology Letters*, 63:21, 2016.

[234] Chiara Gattinoni, David M Heyes, Christian D Lorenz, and Daniele Dini. Traction and nonequilibrium phase behavior of confined sheared liquids at high pressure. *Physical Review E*, 88:052406, 2013.

[235] S-N Ndiaye, L Martinie, D Philippon, N Devaux, and P Vergne. A quantitative friction-based approach of the limiting shear stress pressure and temperature dependence. *Tribology Letters*, 65:149, 2017.

[236] Jianping Gao, WD Luedtke, and Uzi Landman. Structure and solvation forces in confined films: Linear and branched alkanes. *The Journal of chemical physics*, 106:4309–4318, 1997.

[237] Jianping Gao, WD Luedtke, and Uzi Landman. Origins of solvation forces in confined films. *The Journal of Physical Chemistry B*, 101:4013–4023, 1997.

[238] Ion Marius Sivebæk, VN Samoilov, and BNJ Persson. Squeezing molecular thin alkane lubrication films between curved solid surfaces with long-range elasticity: Layering transitions and wear. *The Journal of chemical physics*, 119:2314–2321, 2003.

[239] Bertrand Guillot and Nicolas Sator. A computer simulation study of natural silicate melts. part i: Low pressure properties. *Geochimica et Cosmochimica Acta*, 71:1249–1265, 2007.

[240] Daniele Savio, Nicolas Fillot, Philippe Vergne, Hartmut Hetzler, Wolfgang Seemann, and GE Morales Espejel. A multiscale study on the wall slip effect in a ceramic–steel contact with nanometer-thick lubricant film by a nano-to-elastohydrodynamic lubrication approach. *Journal of Tribology*, 137:031502, 2015.

[241] Nicolas Fillot, Hassan Berro, and Philippe Vergne. From continuous to molecular scale in modelling elastohydrodynamic lubrication: Nanoscale surface slip effects on film thickness and friction. *Tribology Letters*, 43:257–266, 2011.

Publication and conferences

Publication:

Tromp, S., Joly, L., Cobian, M., Fillot, N. (2018).
Title: Chemical Physics at Interfaces Within a Refrigerant-Lubricated Contact: From Electronic Structure to Large Scale Molecular Dynamics Simulations. The Journal of Physical Chemistry C. 2018, 122 (10), pp 5420–5429.
DOI: 10.1021/acs.jpcc.7b11267

Oral presentations:

- Tribology Frontiers Conference, Chicago, USA, 13-15 Nov. 2016.
  Title: Refrigerants as lubricants: from molecular dynamics characterization to the applicability at the contact scale. S. Tromp, L. Joly, M. Cobian, N. Fillot.

- STLE (Society of Tribologists and Lubrication Engineers) 72nd Annual Meeting, Atlanta, USA, 21-25 May 2017.
  Title: Coupling between refrigerant-surface chemistry and lubrication conditions. S. Tromp, L. Joly, M. Cobian, N. Fillot.

- 6th World Tribology Congress, Beijing, China 17-22 Sept. 2017.
  Title: Influence of refrigerant-surface chemistry on lubrication conditions. S. Tromp, L. Joly, M. Cobian, N. Fillot.

Poster presentations:

- 8th Multiscale Materials Modeling Conference, Dijon, France, 9-14 Oct. 2016.
  Title: ReacLub – Strong coupling between flow and physical chemistry in lubricated contacts. S. Tromp, L. Joly, M. Cobian, N. Fillot.

- TriboUK, London, England 27-28 Apr. 2017.
  Title: How to translate ab-initio results about adhesion behavior to a larger scale Molecular Dynamics simulation? S. Tromp, L. Joly, M. Cobian, N. Fillot.

FOLIO ADMINISTRATIF

THESE DE L'UNIVERSITE DE LYON OPEREE AU SEIN DE L'INSA LYON

NOM : TROMP

DATE de SOUTENANCE : 11/07/2018

Prénoms : Stéphane, Arnaud

TITRE : Lubrication with a refrigerant: an industrial challenge investigated through multiscale modeling based on fluid/surface chemistry

NATURE : Doctorat

Numéro d'ordre : 2018LYSEI060

Ecole doctorale : Mécanique, Energétique, Génie Civil, Acoustique

Spécialité : Génie Mécanique

RESUME :
Dans les grands systèmes de réfrigération, l'utilisation de réfrigérants comme lubrifiants, à la place des huiles, simplifie la conception du système, l'allège et réduit son impact environnemental. La très faible viscosité du réfrigérant conduit à une épaisseur de film séparant les deux surfaces comparable à leur rugosité. Néanmoins, des travaux expérimentaux avec le réfrigérant R1233zd suggèrent que la lubrification est possible dans ces conditions grâce à la formation d'une couche adsorbée sur la surface d'oxyde de fer. Les analyses expérimentales in situ dans le contact sont très difficiles à cause des conditions de fort confinement et haute pression. C'est pourquoi une approche numérique multi-échelles est développée, afin d'étudier l'impact des réactions physico-chimiques à l'interface réfrigérant-surface sur les propriétés de lubrification. La théorie de la fonctionnelle de la densité est utilisée pour quantifier au niveau quantique, l'adsorption d'une molécule de réfrigérant sur une surface d'oxyde de fer. Des énergies de liaison allant de -0,92 eV à -0,22 eV sont observées et reliées à différents cas d'adsorption. Ces résultats sont exploités pour paramétrer un champ de forces interfacial, qui prédit des structures moléculaires à l'interface, différentes de celles obtenues avec des potentiels basés sur les règles de mélange classiques. Des simulations de dynamique moléculaire utilisant ce champ de forces paramétré confirment l'existence d'une couche fortement adsorbée de R1233zd sur une surface de Fe_2O_3. Avec des surfaces atomiques lisses et seulement 2 nm d'épaisseur de film de réfrigérant, les couches adsorbées résistent à des pressions allant jusqu'à 4 GPa et des vitesses de cisaillement atteignant 100 m/s. Une valeur minimale de 5 molécules de réfrigérant par nm² est nécessaire à la formation de deux couches adsorbées à 0.5 GPa. De plus, des simulations en cisaillement avec une surface rugueuse prédisent une rupture totale du film à environ 13 GPa.

MOTS-CLÉS :
Lubrification, Réfrigérants, Physico-Chimie Fluide/Surface, Dynamique Moléculaire, Théorie de la Fonctionnelle de Densité

Laboratoire (s) de recherche : Laboratoire de Mécanique des Contacts et des Structures – Institut Lumière Matière

Directeur de thèse: Dr. Nicolas Fillot, Prof. Laurent Joly

Présidente de jury : Prof. Céline Leonard

Composition du jury :
    Dr. Manuel Cobian (Examinateur)
    Prof. Daniele Dini (Rapporteur)
    Dr. Nicolas Fillot (Directeur)
    Prof. Laurent Joly (Co-directeur)
    Prof. Céline Leonard (Examinatrice)
    Prof. Michael Moseler (Rapporteur)